

The impact of model assumptions on coronary blood flow computations

Citation for published version (APA):

Gashi, K. (2019). *The impact of model assumptions on coronary blood flow computations*. [Phd Thesis 1 (Research TU/e / Graduation TU/e), Biomedical Engineering]. Technische Universiteit Eindhoven.

Document status and date:

Published: 26/06/2019

Document Version:

Publisher's PDF, also known as Version of Record (includes final page, issue and volume numbers)

Please check the document version of this publication:

- A submitted manuscript is the version of the article upon submission and before peer-review. There can be important differences between the submitted version and the official published version of record. People interested in the research are advised to contact the author for the final version of the publication, or visit the DOI to the publisher's website.
- The final author version and the galley proof are versions of the publication after peer review.
- The final published version features the final layout of the paper including the volume, issue and page numbers.

[Link to publication](#)

General rights

Copyright and moral rights for the publications made accessible in the public portal are retained by the authors and/or other copyright owners and it is a condition of accessing publications that users recognise and abide by the legal requirements associated with these rights.

- Users may download and print one copy of any publication from the public portal for the purpose of private study or research.
- You may not further distribute the material or use it for any profit-making activity or commercial gain
- You may freely distribute the URL identifying the publication in the public portal.

If the publication is distributed under the terms of Article 25fa of the Dutch Copyright Act, indicated by the "Taverne" license above, please follow below link for the End User Agreement:

www.tue.nl/taverne

Take down policy

If you believe that this document breaches copyright please contact us at:

openaccess@tue.nl

providing details and we will investigate your claim.

The impact of model assumptions on coronary blood flow computations

K. Gashi

A catalogue record is available from the Eindhoven University of Technology Library

ISBN: 978-90-386-4816-3

© Copyright 2019, Kujtim Gashi

All Rights Reserved. No part of this book may be reproduced, stored in a database or retrieval system, or published, in any form or in any way, electronically, mechanically, by print, photo print, microfilm or any other means without prior written permission of the author.

Cover design: Stefanie van den Herik || www.svdhmedia.nl
Printed: ProefschriftMaken || www.proefschriftmaken.nl

The research described in this thesis was supported by a grant of the Dutch institute IMDI-ZonMw [Project number: 104003009]

The publication of this thesis is financially supported by HeartFlow. Financial support by the Dutch Heart Foundation for the publication of this thesis is gratefully acknowledged.

The impact of model assumptions on coronary blood flow computations

PROEFSCHRIFT

ter verkrijging van de graad van doctor aan de Technische Universiteit
Eindhoven, op gezag van de rector magnificus prof.dr.ir. F.P.T. Baaijens,
voor een commissie aangewezen door het College voor Promoties, in het
openbaar te verdedigen op woensdag 26 juni 2019 om 16:00 uur

door

Kujtim Gashi

Geboren te Zürich, Zwitserland

Dit proefschrift is goedgekeurd door de promotoren en de samenstelling van de promotiecommissie is als volgt:

voorzitter: prof. dr. ir. C.W.J. Oomens
1e promotor: prof. dr. ir. F.N. van de Vosse
2e promotor: prof. dr. C.A. Taylor
co-promotor: dr. ir. E.M.H. Bosboom
leden: prof. dr. L.R. Hellevik (NTNU Trondheim)
prof. dr. ir. M.A. Viergever (JMC Utrecht)
dr. ir. M.A. Hulsen
dr. W.A.L. Tonino (Catharina ziekenhuis Eindhoven)

Het onderzoek of ontwerp dat in dit proefschrift wordt beschreven is uitgevoerd in overeenstemming met de TU/e Gedragscode Wetenschapsbeoefening.

Table of Contents

Summary	5
1 General Introduction	7
1.1 Coronary circulation	8
1.2 Clinical problem	9
1.3 Current clinical practice	10
1.4 Fractional flow reserve	10
1.5 Virtual FFR	12
1.6 Uncertainty quantification & Sensitivity analysis	14
1.7 Aim and thesis outline	15
2 Impact of blood viscosity models on computed fractional flow reserve	17
2.1 Introduction	19
2.2 Materials and Methods	20
2.2.1 Patient specific geometries	20
2.2.2 CFD modelling	20
2.2.3 Viscosity model	21
2.2.3.1 Constant viscosity value	21
2.2.3.2 Patient-specific Newtonian	21
2.2.3.3 Quemada model	21
2.2.4 Numerical implementation	23
2.3 Simulations & analysis	23
2.3.1 Non-Newtonian simulations	23
2.4 Discussion	28
2.4.1 Non-Newtonian simulations	28
2.4.2 Limitations	29
2.4.3 Conclusion	29
2.5 Acknowledgment	30
3 Influence of population-based variance of blood viscosity on the uncertainty in computed fractional flow reserve	31
3.1 Introduction	33
3.2 Materials and Methods	34
3.2.1 Patient specific geometries	34
3.2.2 CFD modelling	34
3.2.3 Non-Newtonian model	35

3.2.4	Numerical implementation	36
3.2.5	Uncertainty analysis & sensitivity analysis	36
3.3	Simulations & analysis	38
3.3.1	Non-Newtonian simulations	38
3.3.2	Sensitivity analysis	40
3.4	Discussion	41
3.4.1	Non-Newtonian simulations	42
3.4.2	Sensitivity analysis	42
3.4.3	Limitations	43
3.4.4	Conclusion	43
3.5	Acknowledgment	44
4	The influence of model order reduction on the computed fractional flow re- serve using parameterized coronary geometries	45
4.1	Introduction	47
4.2	Material and Methods	48
4.2.1	Geometry definition	48
4.2.2	CFD model	51
4.2.3	Boundary conditions	51
4.2.4	Uncertainty analysis	54
4.2.5	Post-processing	55
4.3	Results	55
4.3.1	Verification	55
4.3.2	Model comparison	55
4.3.3	Uncertainty analysis	57
4.4	Discussion	59
4.4.1	Model comparison	59
4.4.2	Uncertainty analysis	60
4.4.3	Limitations	61
4.5	Conflict of interest statement	61
4.6	Acknowledgment	61
5	Uncertainty quantification for computed FFR using myocardial perfusion and left ventricular mass	63
5.1	Introduction	65
5.2	Materials and Methods	66
5.2.1	Data acquisition	66
5.2.2	Mesh generation	66
5.2.3	Left ventricle segmentation	66
5.2.4	CFD modelling	67
5.2.5	Boundary conditions	67
5.2.6	Numerical implementation	69
5.2.7	Uncertainty analysis & sensitivity analysis	69
5.2.7.1	Population based	70
5.2.7.2	Measurement based	70
5.2.8	Post-processing	71
5.3	Simulations & analysis	71
5.3.1	Simulations	71

5.3.2	Sensitivity analysis	72
5.4	Discussion	75
5.4.1	Simulations	75
5.4.2	Sensitivity analysis	75
5.4.3	Limitations	76
5.5	Conclusion	77
5.6	Acknowledgment	77
6	General Discussion	79
6.1	General discussion	80
6.1.1	Introduction	80
6.1.2	Impact of blood viscosity	80
6.1.3	Blood viscosity (limitations)	82
6.1.4	Model order reduction	82
6.1.5	Model order reduction (Limitation)	83
6.1.6	Myocardial mass and perfusion	84
6.1.7	Myocardial mass and perfusion (Limitation)	84
6.1.8	Recommendations for future research	85
	Bibliography	87
	Samenvatting	99
	Dankwoord	101
	Curriculum vitae	105
	List of publications	107

Summary

The main task of the heart is to ensure an adequate blood flow. In order to maintain the blood flow, the heart itself also needs to be supplied with sufficient blood flow. This is done via the left and right coronary arteries. Optimal coronary flow is crucial for maintaining cardiac function. However, coronary blood flow can be impaired due to coronary heart disease (CHD). CHD is characterized by atheromatous plaque formation throughout a long period of time resulting in narrow segments (stenosis) in the coronary arteries. With growing plaque formation the coronary lumen area decreases. As a consequence of the lumen area reduction, additional pressure loss over the stenosis occurs resulting in lower blood flow for the corresponding coronary artery. The consequence of this is that the myocardium fed by the coronary artery receives less blood flow which may increase the risk for ischemia and myocardial infarction. Patients with CHD may show symptoms such as pain on the chest, discomfort during stress and exercise or even at rest for severe cases. Treatment options for CHD depend on things such as stenosis severity, stenosis location and patient history. Previous research showed that patients with mild CHD do not benefit from invasive treatment such as angioplasty and stenting. For these patients, life style changes and medication are shown to be sufficient. Patients with severe stenoses require invasive treatment as coronary blood flow tends to be impaired. In the clinic, the severity of a lesion is assessed using the fractional flow reserve (FFR) which is defined as the ratio between the pressure distal and pressure proximal. Depending on the FFR, patients either receive invasive treatment (severe stenosis, $FFR \leq 0.80$) or receive only medicinal treatment ($FFR > 0.80$). However, for patients receiving medicinal treatment the FFR assessment is considered to be unnecessary as a non-invasive treatment is given for an invasive assessment. Computer models can be used to reduce the number of unnecessary invasive assessments by simulating patient specific blood flow in the coronaries. The benefit is that assessment of lesions can be done non-invasively and thus reducing patient discomfort whilst resulting in less complications. From previous studies, the potential benefit of patient-specific CFD modelling of the coronary circulation might be evident. However, due to high computational costs 3D CFD modelling is impeded when performing sensitivity and uncertainty analysis for uncertain model parameters. The goal of the thesis was twofold. First goal is to reduce computational time of models by investigating the feasibility of lower order models. Second goal was investigating the influence of parameter uncertainty on the computed output of interest of coronary models. This thesis comprises of the following chapters: In **Chapter 2**, the influence of several assumptions of the blood viscosity models on the computed FFR was examined. Blood is known to behave in a non-Newtonian behaviour such that viscosity is high for low shear rates and low for high shear rates. Blood viscosity assumptions were taken into account as a fixed value (Newtonian), a Newtonian assumption depending on hematocrit and a non-Newtonian assumption (Quemada model) also depending on

hematocrit. The range in computed FFR was then investigated for the different viscosity assumptions. The results showed that depending on the choice for the blood viscosity model and the choice of input parameters, the FFR could vary up to 0.065. Most of the FFR discrepancies were found to be between a FFR value of 0.6 and 0.8. In several cases, the change in computed FFR was shown to be significant enough to result in a totally different stenosis classification. This shows that the choice of the blood viscosity model impacts the accuracy of FFR computations and might lead to different treatments. In **Chapter 3**, the Quemada model is used which is shown to accurately described blood viscosity behaviour while including two physical quantities (hematocrit and plasma viscosity) which can be measured in the clinic. Using population-based ranges for hematocrit and plasma viscosity, the uncertainty in the computed FFR was investigated in case both parameters for the patient were unknown. Including patient-specific hematocrit values was shown to decrease FFR uncertainty on average by a factor 2.2. The results showed that approximately 60% and 40% of the uncertainty in the FFR could be attributed to hematocrit and plasma viscosity, respectively. In **Chapter 4**, the effect of model-order reduction for CFD models for coronary circulations on the computed FFR was investigated using parameterized approach. To this end, 200 coronary vessels were generated in 3D for seven different geometry characteristics such as stenosis severity, vessel curvature, torsion, etc. For each 3D vessel a corresponding 2D vessel was generated. The goal was to investigate if a high diagnostic accuracy could be maintained while using a significantly less computational expensive model (2D). The results show that a 2D model is accurate enough to replace the 3D model. We furthermore have shown that when choosing a 'correct' steady flow, the results are similar as when an unsteady approach which generally is more computationally expensive. In **Chapter 5**, the effect of several boundary conditions on the computed FFR was investigated. To this end, a workflow was used where the flow was estimated based on the size of the myocardium and the expected perfusion of the myocardium (flow per amount of myocardium). The flow among coronary vessels was divided based on vessel sizes using Murray's Law. Whereas the pressure at the inlet was chosen to be the mean arterial pressure. These four parameters were varied within their population-based range. Results showed that myocardial size had the largest impact on the FFR whereas the flow division and mean arterial pressure had almost negligible effects. Even when including measured left ventricular mass with an uncertainty of 5%, left ventricular mass was shown to remain the most important parameter. In order to have accurate FFR predictions, effort should be dedicated to obtaining accurate myocardial sizes and perfusion whilst fixing the flow division to a population-based value.

CHAPTER

1

General Introduction

1.1 Coronary circulation

In order for the organs of the human body to properly function, it needs to be supplied with oxygen and nutrients, which is done via convective transport of blood through the cardiovascular system. The main task of the heart is to ensure an adequate blood flow by means of contracting and thus pushing blood into the cardiovascular circulation. In order for the heart to be able to contract, the heart itself also needs to be supplied with oxygen-rich blood. This is done via the coronary circulation which consists of the coronary arteries, the micro circulation and, the veins. The coronary arteries carry blood towards the myocardial microcirculation where nutrients are exchanged between the myocardium and blood. From the microcirculation, blood is then drained by the veins such that it can be replenished with nutrients.

The two main arteries of the coronary circulation are the left and right coronary artery (LCA and RCA) (see Figure 1.1). Both arteries originate from the aorta just after the aortic valve. The LCA supplies the left side of the heart. It bifurcates into the left circumflex artery (LCx) and the left anterior descending artery (LAD). The RCA supplies the right side of the heart and also bifurcates into two branches, namely the marginal and posterior interventricular artery. The larger arteries are located on top of the epicardium whereas the coronary microcirculation, the small capillaries supplying the tissue with blood, are located within the endocardium. This means that when the heart contracts during systole, the small capillaries are squeezed due to the increase in intramyocardial pressure such that coronary flow decreases (see Figure 1.2). During diastole, when the heart relaxes, the vascular bed is no longer squeezed and can start to open up again. The absence of the intramyocardial pressure then results in an increase in blood flow. Thus the coronary flow tends to be highest during diastole contrary to the rest of the body.

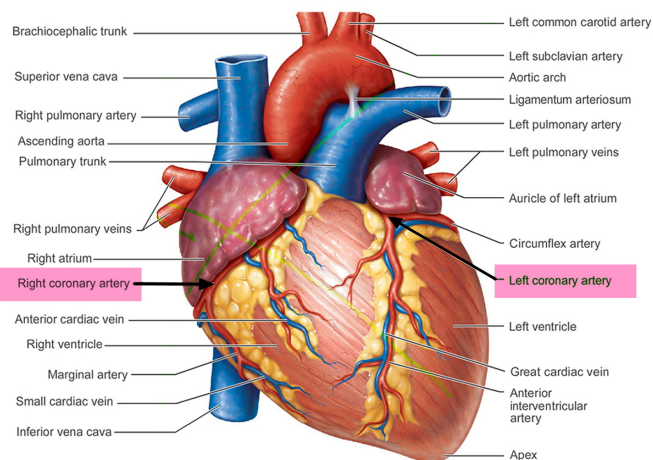


Figure 1.1: Coronary circulations of the heart including both the arteries and veins. Figure adopted from healthjade.com/what-is-heart-disease

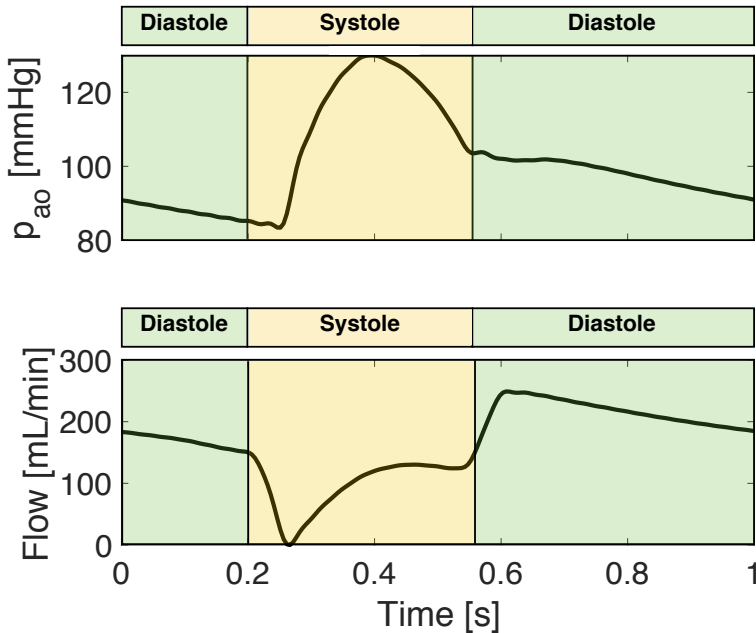


Figure 1.2: Aortic pressure (p_{ao}) and flow coronary flow for a left coronary artery during one cardiac cycle. The systole and diastole of the cardiac cycle are indicated in yellow and green, respectively.

The intramyocardial pressure is different for the left and right side of the heart. The left ventricle generates higher pressures compared to the right ventricle such that the intramyocardial pressure is also higher. Consequently, the systolic flow for the right side will be higher compared to the left side in the heart due to lower intramyocardial pressures.

1.2 Clinical problem

Optimal coronary flow is crucial for maintaining cardiac function. However, coronary blood flow can be impaired due to coronary heart disease (CHD). With CHD, coronary arteries are accompanied by narrow segments, stenoses or lesions, which are the result of atheromatous plaque formation throughout a long period of time (Stary et al., 1995). Lumen area of coronary arteries may be reduced due to plaque formation. As a result, blood flow may experience an increase in resistance with respect to the healthy case with no narrowing due to the lumen narrowing. Thus the lumen narrowing may lead to a pressure loss resulting in a lower distal coronary pressure (Gould, 2009; Miller et al., 1994). If with the same venous pressure, the difference between arterial and venous pressure decreases, lower blood flow of the affect myocardium is the result. With lower coronary blood flow, the myocardium is less perfused and thus raising the risk for ischemia or at some point even myocardial infarction depending on the severity (Stary et al., 1995). Patients with CHD may

show symptoms such as pain on the chest (angina pectoris), discomfort during stress and exercise or, in severe cases, at rest.

1.3 Current clinical practice

Ischemia and myocardial infarction can be detected using non-invasive tests such as ECG, echocardiography, and stress tests. If a physician suspects a patient to suffer from CHD, further examinations will be conducted using coronary angiography or computed tomography angiography (CTA). Using these imaging modalities, the state of the arteries can be investigated and potential stenoses can be located.

The treatment options for CHD depend on a number of things such as the stenosis severity, state of the arteries, location of the stenosis, clinical setting, and patient history. Using this information the physician determines the appropriate treatment. For mild stenoses, life style changes and medication are sufficient to stop the disease from progressing. For more severe stenoses percutaneous coronary intervention (PCI) is needed which involves angioplasty and stenting. With angioplasty, a catheter with deflated balloon is guided to the site of the stenosis. Once placed at the location, the balloon is inflated to force the stenosis open and thus restoring the lumen area of the blood vessel. In order to keep the lumen area open, a stent can be inserted such that the vessel will remain open. Once the stent is left behind, the catheter with deflated balloon is withdrawn. For patients who have multiple stenoses or who otherwise would be unsuitable for PCI will receive coronary artery bypass grafting (CABG) surgery. With CABG, the affected coronary artery is bypassed using a patient's artery or vein from somewhere else in the body such as leg or arm. This way part of the blood flow is directed via the health graft resulting in less pressure loss and thus effectively restoring blood flow. Another option for CABG is using the left internal mammary artery (LIMA) which is located behind the sternum and shows better long-term patency than other venous and arterial grafts (Arima et al., 2005).

1.4 Fractional flow reserve

For adequate treatment of significant stenoses, the severity and location of a stenosis need to be assessed. Only stenoses effecting myocardial blood flow and thus causing ischemia should be treated with PCI and CABG (Tonino et al., 2010; Pijls et al., 2010). Treating stenoses which are not responsible for myocardial ischemia, i.e. functionally non-significant, does not improve the patient's outcome (Pijls et al., 2010). In order to determine the appropriate treatment, many physicians still rely on visual inspection of stenoses (Hannawi et al., 2014; Dehmer et al., 2012; Ludman et al., 2012). However visual inspection only takes into account the geometry and does not include any functional information of blood flow and blood pressure. Therefore a stenosis which is deemed visually significant will not always lead to a impaired perfusion (Van Belle et al., 2014). Furthermore the correlation between visual assessment and functional significance of stenoses was found to be low (Spearman's $\rho = 0.36$) for stenoses of moderate severity (Fischer et al., 2002).

One solution to circumvent this problem is by using a functional measure which takes into account the underlying physiology of the coronary blood flow. The fractional flow reserve (FFR) is a haemodynamic measure to determine the haemodynamic severity of a stenosis which is shown to have a diagnostic performance above 90% (Pijls et al., 1996,

1995). Formally, the FFR is defined as the ratio between the mean flow with and without stenosis during maximal hyperemia:

$$FFR = \frac{q_s}{q_h} \quad (1.1)$$

The flow through the stenosed vessel is denoted by q_s whereas the flow in case of an absence of a stenosis is denoted by q_h . During maximal hyperemia maximum coronary blood flow is achieved by intravenously infusing adenosine (Russell, 1997). However, measuring *in vivo* blood flow within a clinical setting is much more difficult compared to measuring blood pressure. Using Ohm's law, the flow (q) in both scenarios can be approximated as:

$$q = \frac{p_a - p_v}{R^h}, \quad (1.2)$$

where p_a and p_v denote the arterial pressure and venous pressure, respectively. The resistance of the myocardial tissue during hyperemia is given by R^h . Using two assumptions, the FFR can be approximated by means of a pressure-derived FFR. **1)** First assumption is that by inducing hyperemia the myocardial resistance becomes independent of the stenosis as no autoregulation of the resistance can occur. This means that for the healthy and stenotic case the myocardial resistance in hyperemia are the same and do not change (Pijls *et al.*, 1993). **2)** The second assumption is that the venous pressure (p_v) is negligible compared to the arterial pressure (p_a). Combining Equation (1.1) and Equation (1.2) results in the pressure-derived FFR:

$$FFR = \frac{q_s}{q_h} = \frac{(p_d - p_v)/R^h}{(p_a - p_v)/R^h} \approx \frac{p_d}{p_a}, \quad (1.3)$$

where pressure distal to the stenosis is denoted by p_d . The proximal pressure, distal pressure, venous pressure and, resistance of the myocardial tissue are indexed in Figure 1.3. To measure the pressure-derived FFR in clinic, patients undergo coronary catheterization. A guiding catheter and pressure wire are inserted either via the femoral (groin) or radial (wrist) artery and are positioned at the ostium. While the guiding catheter is left at the ostium, the pressure wire is positioned in the vessel with stenosis. The guiding catheter is used to measure the aortic pressure whilst the pressure wire measures pressure in the coronary arteries. Next step is to induce hyperemia with infusion of adenosine. This way exercise or stress are simulated as usually during this state the patient's discomfort occurs. Once hyperemia is induced, the FFR measurement is performing a slow pull back of the pressure wire towards the guiding catheter. This way the FFR can be obtained throughout the entire length of the coronary artery. In case of multiple stenoses per coronary, each stenosis can be evaluated based on its effect on the FFR.

In a study by Pijls *et al.* the FFR threshold for a functional significant stenosis was set at 0.75 (Pijls *et al.*, 1995). Using this threshold, the DEFER study showed that patients with a functionally non-significant stenosis ($FFR > 0.75$) did not benefit from PCI. On the other hand, patients with functionally significant stenoses ($FFR < 0.75$) were shown to have a significantly benefit from PCI (Bech *et al.*, 2001). In a later study by Tonino *et al.* the FFR threshold was set to 0.80 (Tonino *et al.*, 2009). While FFR has been shown to classify stenoses based on their functional significance (De Bruyne *et al.*, 2012; Pijls *et al.*, 2010; Tonino *et al.*, 2009) coronary angiography on the other hand was shown to often overestimate the severity of stenosis (Green *et al.*, 2004). Based on coronary angiography hemodynamically significant and non-significant stenoses could not always be clearly

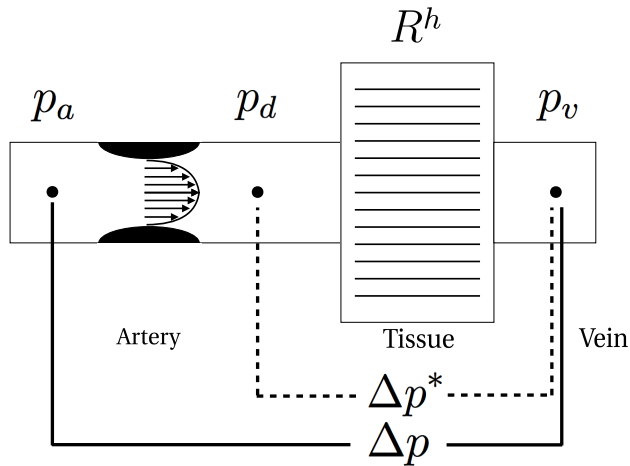


Figure 1.3: A schematic overview of the myocardial tissue, artery and, vein. Moreover, the proximal pressure p_a , distal pressure p_d , venous pressure p_v and, resistance of the myocardial tissue are indicated. Furthermore, the perfusion pressure for both the stenosed and healthy case are indicated with Δp^* and Δp , respectively.

distinguished (Miller et al., 1994; Legrand et al., 1986). Using angiographic classifications of lumen reduction area of 50% to 70%, 71% to 90% or 91% to 99% was unable to clearly classify stenoses into functionally significant and non-significant stenoses using FFR (Tonino et al., 2010) (See Figure 1.4). Moreover angiographic classification of multi-vessel disease did not match with the functional classification. This means that the number of significant stenoses found on a vessel using angiogram or FFR do not match (See Figure 1.4).

Although FFR is shown to be a valuable tool to define functional severity of stenoses, it still remains an invasive measure for which intra-vascular pressures need to be measured. Depending on the measured FFR, patients either receive PCI or CABG ($\text{FFR} \leq 0.80$) or only receive medicinal treatment ($\text{FFR} > 0.80$). The problem is that the latter group receives only medicinal treatment such that retrospectively, catheterization for measuring the FFR is considered to be unnecessary as no physical intrusion was proven to be necessary. This applies for almost 1 out of 2 patients that received an invasive FFR assessment (Van Belle et al., 2014; Curzen et al., 2014).

1.5 Virtual FFR

One study found that 145 of the 253 (58%) participating physicians measure FFR less than one third of the time. Whereas 15.4% of the physicians never measured FFR at all (Han-nawi et al., 2014). Other studies found an adoption rate of 5 to 7% in the USA and Europe (Dehmer et al., 2012; Ludman et al., 2012). Bringing vFFR computer models closer to the clinic could help increase the adoptions rate of the FFR in the clinic.

A benefit of vFFR compared to the clinically used FFR is that due to its non-invasive nature it is safer as complication rates decrease. It furthermore doesn't cause the patient any discomfort as no adenosine needs to be used which is needed for the hyperemia. Moreover,

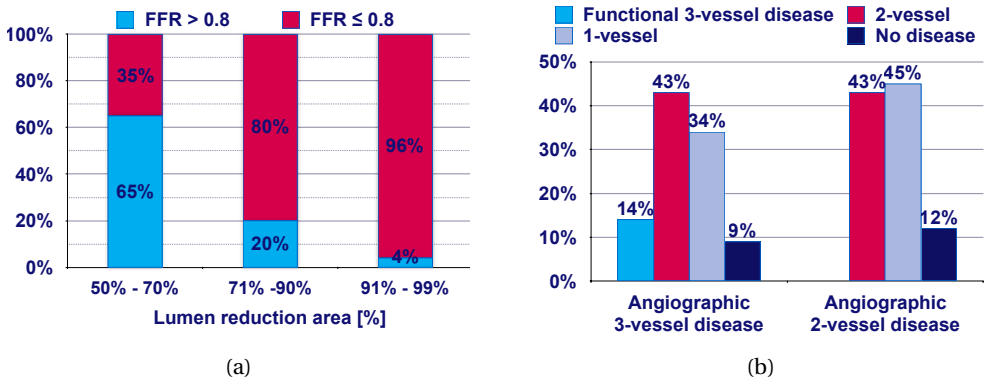


Figure 1.4: Stenoses classification based on angiography and FFR (Tonino et al., 2010). In (a) the three angiographic classifications are split into functionally significant ($FFR \leq 0.80$) and non-significant ($FFR > 0.80$). In (b) angiographic multi-vessel diseases compared against the functional multi-vessel disease.

vFFR is furthermore also cheaper (Douglas et al., 2016) as no catheterization is needed which includes a pressure wire, adenosine infusion, and of course the multiple staff members performing the catheterization.

Patients with stable coronary heart disease could be screened using computer models which compute the FFR without the need of an invasive pressure measurement. The patients then could be classified into patients with functionally significant stenoses ($FFR \leq 0.80$) and patients with functionally non-significant stenoses ($FFR > 0.80$). The latter group would then not need to receive catheterization but only receive medicinal treatment. Patients with significant stenoses can then be directed towards catheterization which depending on the stenosis will result in either PCI or CABG. This way the number of retrospectively unnecessary catheterizations could be reduced significantly as the group with non-significant stenoses is *a priori* excluded from the catheterization. Various studies in literature have shown the feasibility of applying CFD models at computing patient-specific FFR. In the DISCOVER-FLOW, DeFACTO and, NXT studies where FFR was based on the CT acquisitions were shown to yield promising results with accuracy as high as 86% (Koo et al., 2011; Min et al., 2012; Nørgaard et al., 2014). Morris et al. and Tu et al. have shown promising results based on computing FFR using angiography with either single-plane, bi-plane or, multi-plane acquisitions (Morris et al., 2013; Tu et al., 2014). In a study, Douglas et al. showed the feasibility of computed FFR as a diagnostic strategy using a prospective longitudinal trial (Douglas et al., 2015). They found that invasive coronary angiography was cancelled in 61% of the time after receiving FFRct. Moreover, cancelling the invasive coronary angiogram did not result in events in the patients (Douglas et al., 2015).

Another usage of computer models could be to determine the optimal treatment per patient by modelling various treatments *a priori* and choosing the optimal one (Kim et al., 2014). This could help physicians help decide which stenosis in multi-vessel disease should be taken care of without over treating the patient.

In literature various types of CFD models can be found ranging from 0D to 3D. Based on CTA or MRI acquisitions, 3D CFD models are meant to capture the *in vivo* structure of coronary arteries (Taylor et al., 2013; Min et al., 2015; Nakazato et al., 2013). Vessel

geometries can also be generated based on single-plane or bi-plane angiograms which however require additional reconstruction (Çimen et al., 2016; Chen and Carroll, 2000). Morris *et al.* showed promising results based on these semi-3D geometries (Çimen et al., 2016). A more straightforward model that could be generated based on angiograms is the 2D axisymmetric model which only requires a centerline with corresponding radius profile. The 2D axisymmetric model is effectively a slice from centerline to radius of a straightend tube and thus reducing computational time significantly (Morris et al., 2016).

Another type of CFD model are the 1D models (Fossan et al., 2018; van der Horst et al., 2013; Itu et al., 2012; Renker et al., 2014). For these relatively simple models, mass and momentum conservation equations are integrated over the cross-sectional area of a blood vessel such that only the axial direction is retained (van der Horst et al., 2013; Fossan et al., 2018; Itu et al., 2012; Van de Vosse and Stergiopoulos, 2011). Using 1D models, a larger portion of the circulation can be modelled. The last type of model is the lumped-parameter models (0D) model. This type of model is based on an *a priori* obtained pressure-flow relation of stenoses for various geometrical features (Huo et al., 2011; Schrauwen et al., 2015; Bessems, 2007).

Although the feasibility of applying CFD models for computing patient-specific FFR has been shown, there are still discrepancies between computed and actual measured FFR (see Figure 1.5a-c). These discrepancies may pose a problem when computing FFR values close to the 0.80 threshold of stenosis classification, leading to false positives and false negatives and thus eventually leading to overtreatment or undertreatment. Uncertainty quantification and sensitivity analysis could help in gaining more certainty regarding FFR predictions per stenosis.

1.6 Uncertainty quantification & Sensitivity analysis

Although CFD models for FFR are shown to have a high accuracy (Koo et al., 2011; Min et al., 2012; Nørgaard et al., 2014; Nakazato et al., 2013; Renker et al., 2014), model accuracy does not remain constant as a function of the FFR (see Figure 1.5d). In a review study performed by Cook *et al.* (Cook et al., 2017), where five studies were compared, FFR models were shown to have the highest accuracy (> 86%) for low ($FFR < 0.6$) and high ($FFR > 0.8$) FFR values (Koo et al., 2011; Min et al., 2012; Nørgaard et al., 2014; Nakazato et al., 2013; Renker et al., 2014). However, for FFR between 0.7 and 0.8 the accuracy was shown to be approximately 46% (Cook et al., 2017). Especially for FFR between 0.7 and 0.8, where a small error in FFR can lead to ambivalent classification of stenoses, accuracy should be highest. Moreover, a single computed FFR value hardly suffices in this region. Ideally for this range, a confidence interval of the FFR should be given to classify stenoses with more certainty. Moreover, accuracy of the computed FFR should be increased. Including parameter uncertainty, the FFR uncertainty can be quantified. Furthermore using sensitivity analysis, parameters with the largest impact on the FFR can be identified (Huberts et al., 2014; Quicken et al., 2016; Sankaran et al., 2016; Fossan et al., 2018). This way both the model can be more accurate as the parameter with the largest influence then can be measured or estimated more accurately whereas also a range of uncertainty in the FFR can be given. Examples of UQ&SA for computed FFR can be found in for example the studies of Fossan and Sankaran (Sankaran et al., 2014, 2016; Fossan et al., 2018) where effects of boundary conditions, viscosity and, geometry on the FFR are investigated.

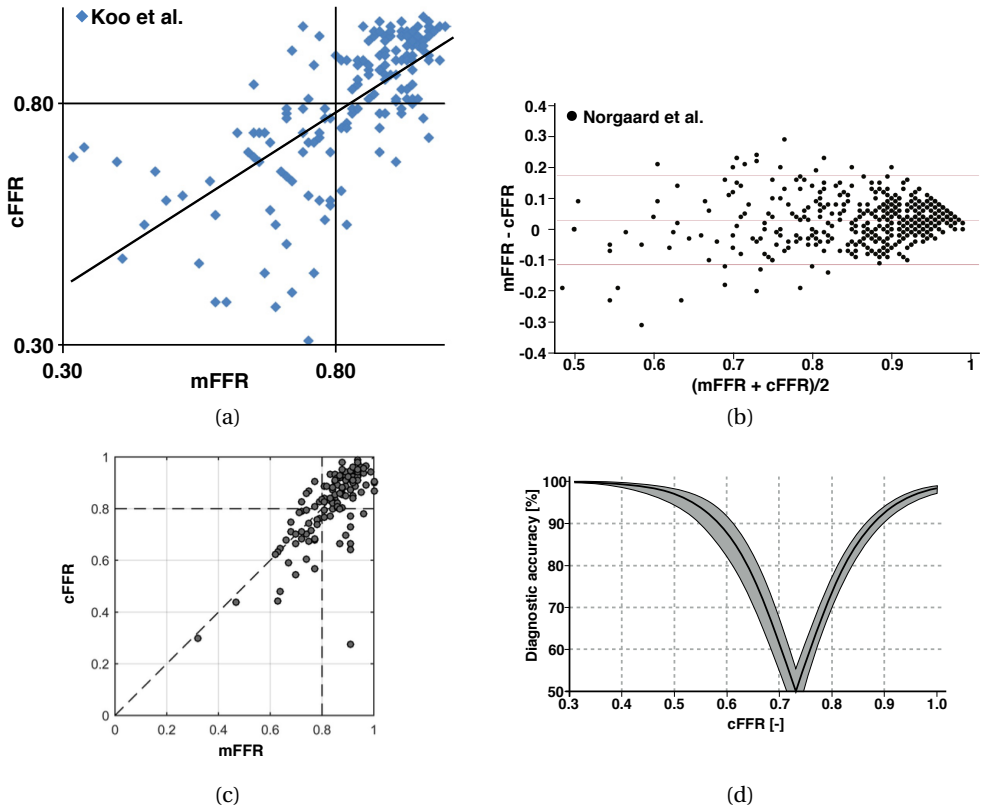


Figure 1.5: Overview of various studies comparing measured FFR (mFFR) with computed FFR (cFFR.) In (a) the results from Koo *et al.* are shown (Koo *et al.*, 2011). The results from Norgaard *et al.* (Nørgaard *et al.*, 2014) are depicted in (b) whereas the findings of Itu *et al.* are shown in (c) (Itu *et al.*, 2016). In (d) the diagnostic accuracy for the models as a function of cFFR is depicted as published by Cook *et al.* (Cook *et al.*, 2017).

1.7 Aim and thesis outline

The potential benefit of patient-specific CFD modelling of coronary blood flow is evident from previous studies. However, current 3D modelling is impeded by high computational costs (Morris *et al.*, 2017) when performing sensitivity and uncertainty analysis for model parameters. The goal of the thesis is twofold. The first goal is to reduce computational time of models by investigating the feasibility of reduced order models. The second goal is investigate the influence of parameter uncertainty in boundary conditions and blood viscosity models on the computed FFR of coronary models. This thesis comprises of the following chapters:

In **Chapter 2**, the influence of several viscosity assumptions on the computed FFR were investigated. To this end three different viscosity assumptions *e.g.* a constant viscosity value, a Newtonian approach including patient-specific hematocrit and a non-Newtonian approach including patient-specific hematocrit. For both patient-specific blood viscosity

models the plasma viscosity will be constrained to physiological values. FFR computations of the various viscosity assumptions are carried out for coronaries extracted from CTA.

In **Chapter 3**, the effect of variations in plasma viscosity and hematocrit on the computed FFR are investigated. Based on the variations of both parameters, the inter-patient variations on the computed FFR is determined using uncertainty quantification. Moreover, using sensitivity analysis the parameter with the largest effect on the computed FFR can be determined.

In **Chapter 4**, the aim is to investigate if less complex models maintain accuracy compared to their more complex three-dimensional counterpart. To this end a large number of parameterized coronaries are generated for seven different geometry characteristics such as stenosis severity, vessel curvature, torsion, etc. The results will show whether a less complex model is accurate enough to replace the 3D model. Moreover, we will extend the analysis to the steady inflow boundary conditions on the computed FFR with respect to the unsteady approach.

In **Chapter 5**, the effect of several boundary conditions on the computed FFR will be investigated. To this end, a workflow is used where the flow is estimated based on the size of the myocardium and the expected perfusion of the myocardium (flow per amount of myocardium). The flow among coronary vessels is divided based on vessel sizes using Murray's Law. Whereas the pressure at the inlet will be chosen to be the mean arterial pressure. These four parameters will be varied within their population-based range. Results of this chapter will identify the parameter with the largest impact on the computed FFR using sensitivity analysis.

In **Chapter 6**, the results and findings of **Chapter 2** to **Chapter 5** will be discussed and put into perspective with findings from literature.

CHAPTER **2**

**Impact of blood viscosity models
on computed fractional flow
reserve**

This chapter is based on: Impact of blood viscosity models on computed fractional flow reserve, **K. Gashi**, N. Xiao, E. M. H. Bosboom, M. van 't Veer, C. A. Taylor, and F. N. van de Vosse, *Submitted*

Abstract

Although blood viscosity is known to depend on the shear rate, in computational fluid dynamics (CFD) blood is often considered to behave as a Newtonian fluid. In this study, we examined the impact of using different constitutive models, both Newtonian and non-Newtonian, on the computed fractional flow reserve (FFR). 206 coronary lesions, imaged using CTA, were considered, and three-dimensional CFD simulations were carried out for the coronary circulation. We have shown that 26% to 53% of the cases considered can have a greater difference in computed FFR than the reported reproducibility of invasive FFR. While uncertainty in geometry and boundary conditions were not considered, the results clearly demonstrate that the choice of blood viscosity model has a significant impact on the FFR prediction.

2.1 Introduction

Fractional flow reserve (FFR) has become the gold standard for determining haemodynamic severity of a coronary stenosis and for deciding treatment. FFR is defined as the ratio between the invasively measured pressure distal and proximal to the stenosis averaged over time (Pijls *et al.*, 1995). In multiple studies, FFR has been shown to reliably classify stenoses based on functional significance (Tonino *et al.*, 2010; Pijls *et al.*, 2007). Patients with FFR 0.80 receive percutaneous coronary intervention (PCI) or coronary artery bypass grafting (CABG), whereas patients with a FFR above 0.80 are usually medically treated. It has been shown that the latter group of patients often undergo unneeded invasive FFR assessment (Min *et al.*, 2012; Koo *et al.*, 2011; Nørgaard *et al.*, 2014). To reduce the number of unnecessary and potentially risky invasive procedures, research has been aimed at applying computational fluid dynamics (CFD) to predict patient-specific FFR (Taylor *et al.*, 2013; Tu *et al.*, 2014; Morris *et al.*, 2013, 2015; Koo *et al.*, 2011).

In most CFD models blood is assumed to behave as a Newtonian fluid whereas in actuality blood exhibits complex non-Newtonian properties such as shear thinning, yield stress and viscoelasticity (Marcinkowska-Gapińska and Kowal, 2009; Long *et al.*, 2005; Revellin *et al.*, 2009). Although a Newtonian model can yield good approximations for the constitutive behavior of blood in higher flow regimes, non-Newtonian models are still needed for accurate predictions at lower flow rates (Johnston *et al.*, 2006, 2004; Cho and Kensey, 1991). The coronary circulation can show heavily decelerating or even retrograde flow in the epicardial coronary arteries because of the effect of myocardial contraction on the coronary micro-circulation. Large variations in flow rates within the coronary tree may have a significant effect on viscosity due to variations in shear rate. During systole, coronary flow and thus shear rates are usually lower compared to diastole. Consequently, viscosity is higher at systole and lower at diastole, which is the phase where most of the coronary flow occurs. Assuming a constant viscosity independent of shear rate could therefore introduce inaccuracies.

Several studies have shown that blood viscosity not only depends on shear rate but also on hematocrit: blood viscosity increases with hematocrit (Baskurt and Meiselman, 2003; Long *et al.*, 2005). Cokelet *et al.* (Cokelet, 1987) showed that an increase in hematocrit from 0.45 to 0.46 results in a 4% increase in blood viscosity at higher shear rates. The physiological range of hematocrit is between 0.35 and 0.55 (Marcinkowska-Gapińska and Kowal, 2009). For high shear rates and an average plasma viscosity, blood viscosity can vary by approximately a factor 1.6 from a hematocrit of 0.35 to 0.55 (Quemada, 1977), and for lower shear rates, the effect is even larger (Quemada, 1977). Shear thinning as a result of rouleaux formation at low shear rates is considered to be an important property of blood (Revellin *et al.*, 2009; Baskurt and Meiselman, 2003; Chen *et al.*, 2006; Mandal, 2005; Johnston *et al.*, 2004). Another important component of the total blood viscosity is the plasma viscosity: an increase in plasma viscosity also increases the total blood viscosity (Marcinkowska-Gapińska and Kowal, 2009; Quemada, 1977). This potential change in plasma viscosity does not depend on the hematocrit and the cells within the plasma as plasma behaves like a Newtonian fluid (Baskurt and Meiselman, 2003).

Finally, regarding viscoelasticity, McMillen *et al.* (McMillan *et al.*, 1986) showed that the viscoelasticity of blood diminishes very rapidly as shear rate rises which is the case in coronary arteries during hyperemia. Furthermore, Gijssen *et al.* (Gijssen *et al.*, 1999) showed that viscoelasticity can be ignored when investigating velocity profiles in medium sized arteries. In the literature, various non-Newtonian blood viscosity models can be found

(Quemada, 1977; Neofytou, 2004; Ree and Eyring, 1955). In particular, Quemada *et al.* (Quemada, 1977) developed a model that considers the influences of hematocrit, plasma viscosity and non-Newtonian behaviour on the total blood viscosity. The main benefit of the Quemada model over other non-Newtonian models is the fact that it depends on hematocrit and plasma viscosity, quantities that can be easily assessed from blood samples. Since blood samples can be taken in the clinical workflow, further personalization of CFD simulations, using patient-specific hematocrit and plasma viscosity, may be feasible. In this study, the influence of different viscosity assumptions on the computed FFR were investigated. For this purpose, we used three different viscosity assumptions *e.g.* a constant viscosity value, a Newtonian approach including patient-specific hematocrit and a non-Newtonian approach including patient-specific hematocrit where the plasma viscosity will be bounded to a physiological range of values. Simulations were carried out for coronary geometries extracted from CTA.

2.2 Materials and Methods

2.2.1 Patient specific geometries

For this study, geometries were based on a previous CTA study (Koo *et al.*, 2011). In total 206 lesions (146 patients) for which the hematocrit was available, were analyzed.

2.2.2 CFD modelling

In this study, blood flow was simulated by solving the incompressible unsteady Navier-Stokes equations given by:

$$\rho \left(\frac{\partial \vec{u}}{\partial t} + \vec{u} \cdot \nabla \vec{u} \right) = -\nabla p + \nabla \cdot 2\eta \mathbf{D}, \quad (2.1)$$

$$\nabla \cdot \vec{u} = 0. \quad (2.2)$$

The blood velocity and pressure are denoted by \vec{u} and p , and the blood viscosity is given by η . The rate of deformation tensor and blood density are denoted by \mathbf{D} and ρ , respectively. The constitutive model for blood can either be Newtonian (constant value for viscosity) or non-Newtonian using the blood shear rate. At the aortic inlet, a constant cardiac output was prescribed using a flat velocity profile, and the vessel walls were assumed to be rigid. In this study, a steady-state flow condition was used as it has been shown to provide reasonably accurate estimates for FFR (Fossan *et al.*, 2018; Morris *et al.*, 2017; Gashi *et al.*, 2018). The coronary outflow resistances (Kim *et al.*, 2010; Vignon-Clementel *et al.*, 2006; Sankaran *et al.*, 2012; Min *et al.*, 2015; Taylor *et al.*, 2013) to simulate maximal hyperemia were determined using the estimated fraction of the left ventricular myocardial mass perfused by each coronary vessel and appropriate assumptions regarding the vasodilatory effects of adenosine. First, based on the segmented left ventricular myocardium from the CTA images, the total basal coronary flow is computed from the estimated cardiac flow demand. Next, the baseline resistances of each individual coronary outlet boundary are computed from the estimated basal flow and morphometric relationships between flow rates and diameters. Maximal hyperemia is simulated by modeling the effect of a typical dose of adenosine by lowering the coronary outlet resistances to minimum values (Taylor

et al., 2013). The outflow resistance at the aortic outlet, representing the total systemic resistance, was adjusted together with the cardiac output to reproduce a physiologically realistic aortic pressure. The fluid equations were numerically solved using a stabilized, semi-discrete finite element method, using meshes containing linear tetrahedral elements with boundary layers at the vessel walls. FFR was calculated with $FFR = P_c/P_{A0}$, where P_c is the steady-state pressure in the coronary artery, and P_{A0} is the average pressure in the aorta.

2.2.3 Viscosity model

2.2.3.1 Constant viscosity value

The first method that was considered for modeling blood viscosity is to treat blood as a Newtonian fluid, where the viscosity is a single constant value independent of patient-specific characteristics. For this study, two constant values of viscosity were chosen from literature (Van Tricht et al., 2005; Kim et al., 2010; Valen-Sendstad and Steinman, 2014; Steele et al., 2007) :

$$\eta_{3.5} = 3.5 \cdot 10^{-3} \text{Pa} \cdot \text{s} \quad (2.3)$$

$$\eta_{4.5} = 4.5 \cdot 10^{-3} \text{Pa} \cdot \text{s} \quad (2.4)$$

2.2.3.2 Patient-specific Newtonian

Additionally, a patient-specific Newtonian model was considered, where the viscosity is calculated using the hematocrit and plasma viscosity values measured from the patient. For this study we used the model for blood viscosity from the work of Sankaran *et al.* (Sankaran et al., 2016)

$$\eta_N = \frac{\eta_p}{(1 - H_{ct})^{2.5}}, \quad (2.5)$$

where H_{ct} is the hematocrit denoted in a fraction and η_p is the plasma viscosity constant at $1.1 \cdot 10^{-3} \text{Pa} \cdot \text{s}$. In the literature, the plasma viscosity was reported as varying between $1.00 \cdot 10^{-3}$ and $1.50 \cdot 10^{-3} \text{Pa} \cdot \text{s}$ (Baskurt and Meiselman, 2003; Haidekker et al., 2002; Késmárky et al., 2008; Rand et al., 1964). Hence, we chose to also consider a higher plasma viscosity of $1.4 \cdot 10^{-3} \text{Pa} \cdot \text{s}$ so that both the lower and higher ends of the viscosity range was taken into account. The patient-specific Newtonian viscosity with a plasma viscosity of $1.1 \cdot 10^{-3} \text{Pa} \cdot \text{s}$ is denoted as $\eta_{N,1.1}$ whereas for a plasma viscosity of $1.4 \cdot 10^{-3} \text{Pa} \cdot \text{s}$ it is denoted as $\eta_{N,1.4}$.

2.2.3.3 Quemada model

A more complex representation of the blood viscosity within the patient would incorporate patient-specific measurements of hematocrit and plasma viscosity and account for the shear-thinning properties of blood. In the Quemada model blood viscosity is a function of hematocrit (H_{ct}) and blood plasma viscosity (η_p) which are both measurable physical quantities. The Quemada model is given by:

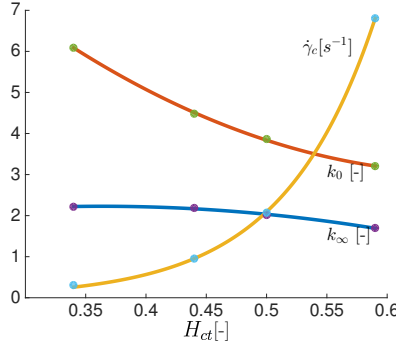


Figure 2.1: $\dot{\gamma}_c$, k_0 and k_∞ as a function of the hematocrit. Dots indicate measurements (Oliver, 1986).

$$\eta_Q = \eta_p \left[1 - \frac{1}{2} K_Q H_{ct} \right]^{-2}, \quad (2.6)$$

$$K_Q = \left(\frac{k_0 + k_\infty \sqrt{\frac{\dot{\gamma}}{\dot{\gamma}_c}}}{1 + \sqrt{\frac{\dot{\gamma}}{\dot{\gamma}_c}}} \right). \quad (2.7)$$

Herein, k_0 and k_∞ represent the intrinsic viscosities for zero and infinite shear rate, respectively. The Quemada viscosity is denoted as $\eta_{Q,1.1}$ or $\eta_{Q,1.4}$ depending on the choice of η_p . The characteristic shear rate is given by $\dot{\gamma}_c$. For incompressible flow, the magnitude of the effective shear rate ($\dot{\gamma}$) is defined as (Spencer, 2004):

$$\dot{\gamma} = \sqrt{2|II_D|} = \sqrt{|tr(\mathbf{D}^2)|} \quad (2.8)$$

II_D denotes the second invariant of the rate of deformation tensor \mathbf{D} , and \vec{u} denotes the blood velocity in the vessel. The parameters k_0 , k_∞ and $\dot{\gamma}_c$ depend on the hematocrit as observed experimentally by Oliver *et al.* (Oliver, 1986) (see Figure 2.1). In this study, the relationship between k_0 , k_∞ and H_{ct} was obtained by fitting a second order polynomial whereas the relationships between $\dot{\gamma}_c$ and H_{ct} were obtained by fitting an exponential function. k_0 , k_∞ and $\dot{\gamma}_c$ were fitted for the physiologically observed H_{ct} range, *i.e.* between 0.35 and 0.55 (Marcinkowska-Gapińska and Kowal, 2009). All three fits were generated such that the adjusted R^2 was higher than 0.99, resulting in the following equations:

$$k_0(H_{ct}) = \alpha_{0,0} H_{ct}^2 + \alpha_{0,1} H_{ct} + \alpha_{0,2}, \quad (2.9)$$

$$k_\infty(H_{ct}) = \alpha_{\infty,0} H_{ct}^2 + \alpha_{\infty,1} H_{ct} + \alpha_{\infty,2}, \quad (2.10)$$

and,

$$\dot{\gamma}_c(H_{ct}) = \alpha_{\gamma,0} e^{\alpha_{\gamma,1} H_{ct}}. \quad (2.11)$$

The parameter values of the constants for the fitted k_0 , k_∞ and $\dot{\gamma}_c$ can be found in Table 2.1. Using these fitted functions, the blood viscosity predicted by the Quemada model is

shown (Figure 2.2) for low (1s^{-1}) and high (1000s^{-1}) shear rates with varying H_{ct} and η_p . Properties of the isolines of the total blood viscosity change as a function of the shear rate: at low shear rates, blood viscosity mainly depends on hematocrit whereas for higher shear rates plasma viscosity becomes more dominant. Using relationships (2.9) to (2.11) the Quemada model is effectively reduced from a five-parameter model ($k_0, k_\infty, \dot{\gamma}_c, H_{ct}, \eta_p$) to a two-parameter model (H_{ct}, η_p).

2.2.4 Numerical implementation

Both the constant and patient-specific Newtonian viscosity manifest as a single viscosity value throughout the duration of the simulation. The Quemada model on the other hand was continually updated within each time step, whereby the viscosity value is updated using the latest available state of the velocity field. To improve numerical stability, simulations using the Quemada model were initialized by holding the shear rate within the viscosity formula constant at 1000s^{-1} until pressure and flow reached a steady state. Afterwards, the shear rate was computed from the velocity field. Simulations are carried out with a time step of $1 \cdot 10^{-3}$ s until all simulations converged to a new steady state.

2.3 Simulations & analysis

2.3.1 Non-Newtonian simulations

The computed FFR on a single patient-specific model is shown in Figure 2.3 for the various blood viscosity models used in this study. The sorted ranges of the computed FFR values

Table 2.1: Parameter values of the fits for k_0 , k_∞ and $\dot{\gamma}_c$

	$\alpha_{i,0}$	$\alpha_{i,1}$	$\alpha_{i,2}$
k_0	28.3 [-]	-37.83 [-]	15.68 [-]
k_∞	-10.46 [-]	7.601 [-]	0.8468 [-]
$\dot{\gamma}_c$	$3.012 \cdot 10^{-3}$ [s^{-1}]	13.09 [-]	-

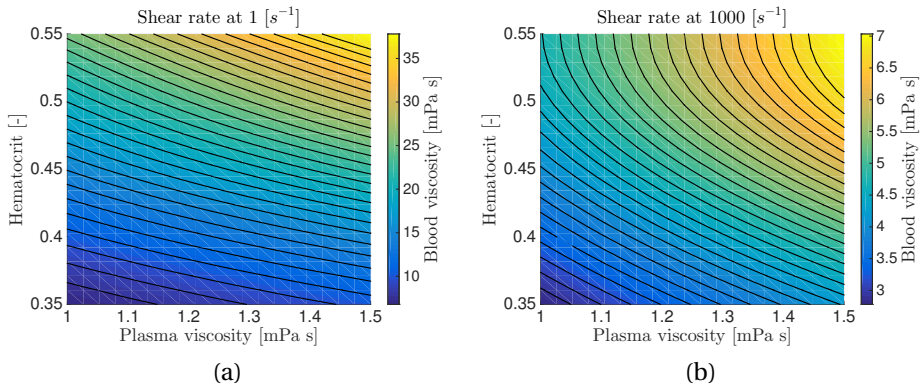


Figure 2.2: Isoviscosity lines for the total blood viscosity as a function of the hematocrit and plasma viscosity for shear rates of 1s^{-1} (a) and 1000s^{-1} (b).

for 206 lesions (146 patients) for six different viscosity cases are shown in Figure 2.4a. The range of computed FFR within a lesion results from different approximations for the blood viscosity. The different FFR predictions for the various viscosity models at multiple locations are shown with an FFR range of up to 0.065 (Figure 2.4b). The largest FFR ranges are observed to be around a FFR of 0.6 to 0.8. For all lesions the range of computed FFR values lies within 0.18 and 0.99. Based on the cut-off value of 0.80, 78 to 96 lesions are deemed significant depending on the viscosity model (see Figure 2.4a & 2.5, Table 2.2). However, 14 lesions (see Figure 2.5) may be either deemed as significant or insignificant depending on the choice of blood viscosity model. This implies that the decision to perform an invasive treatment such as PCI would change depending on the chosen approximation of the blood viscosity assuming that all other variables such as geometry and boundary conditions are known with certainty.

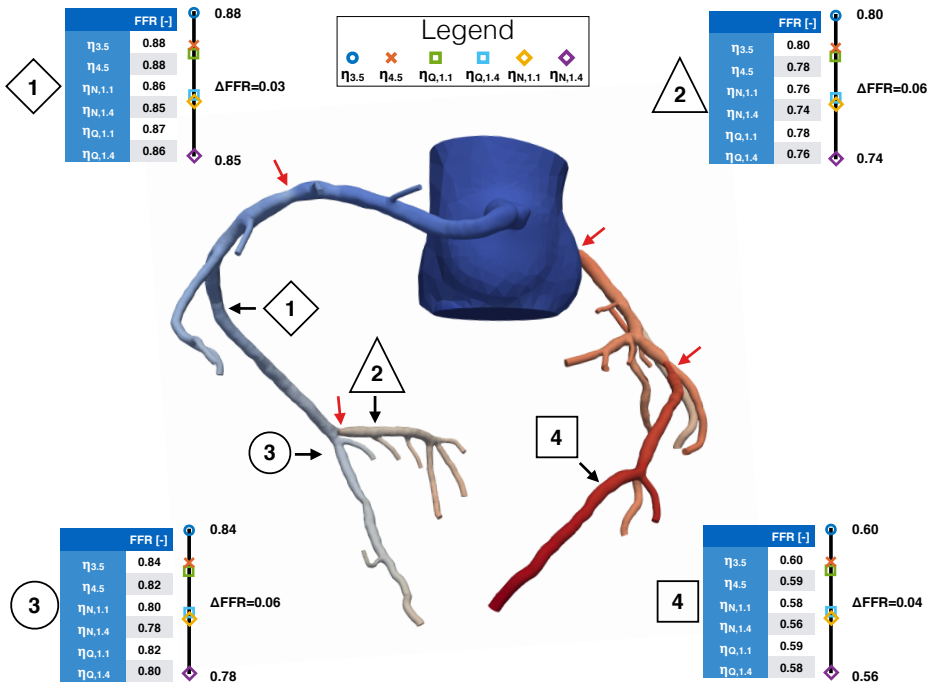


Figure 2.3: The computed FFR for the coronary circulation. The FFRs for the six different viscosity models at four different locations are indicated with arrows and their corresponding number. For each lesion a table of the FFR is included with a FFR distribution for all six models. The locations of the stenoses are indicated with red arrows.

Table 2.2: The number of significant lesions ($FFR \leq 0.80$) for the various Newtonian and non-Newtonian blood viscosity models.

	$\eta_{3.5}$	$\eta_{4.5}$	$\eta_{N,1.1}$	$\eta_{N,1.4}$	$\eta_{Q,1.1}$	$\eta_{Q,1.4}$
# Significant lesions [-]	78	87	83	96	83	91

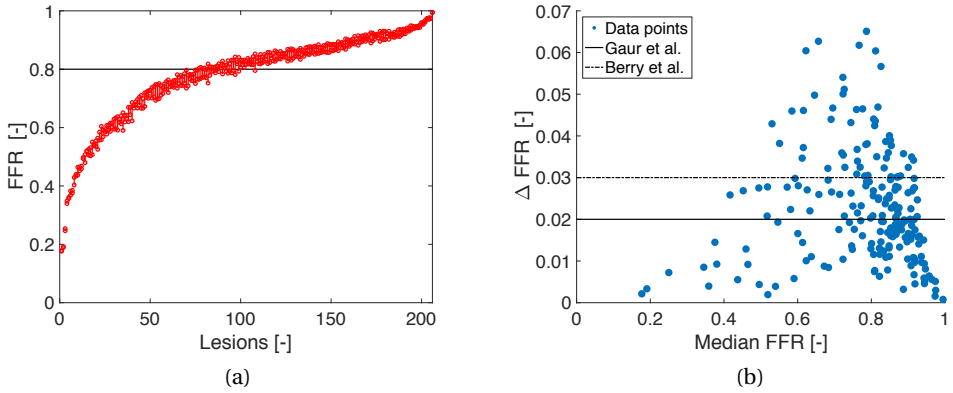


Figure 2.4: The computed FFR ranges for 206 lesions sorted from lower to higher FFR (a). The black line represents the FFR threshold for invasive treatment. In (b) the FFR ranges are shown as a function of the median FFR using the different viscosity models relative to the measured reproducibility. The dashed and solid lines in (b) represent the measured reproducibility obtained by Berry *et al.* (Berry *et al.*, 2013) and Gaur *et al.* (Gaur *et al.*, 2014b), respectively.

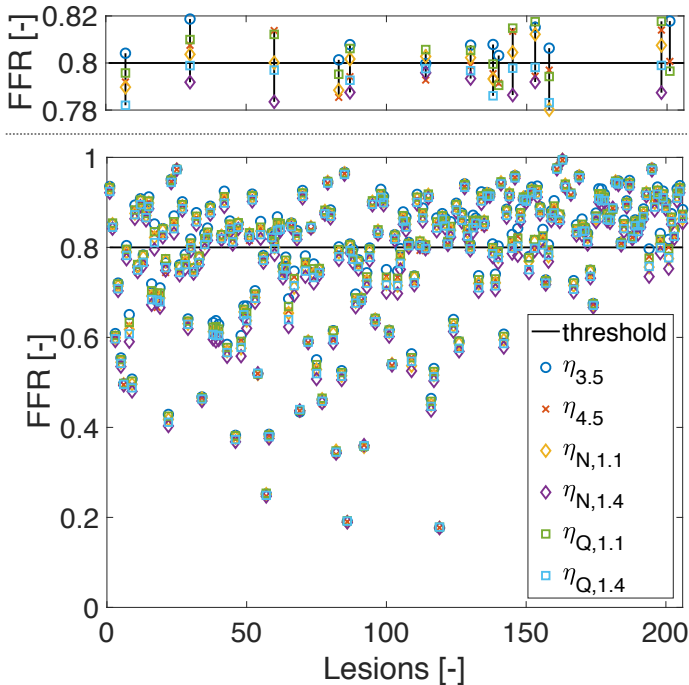


Figure 2.5: The computed FFR for the 206 lesions (146 patients) for six different viscosity cases is shown in the bottom figure. The FFRs with constant viscosity $\eta_{3.5}$ and $\eta_{4.5}$ are indexed with a circle and cross, respectively. The FFRs using the Newtonian model (η_N) based on the hematocrit and the non-Newtonian Quemada model (η_Q) are represented with a diamond and square, respectively. The black line indicates the FFR threshold for invasive treatment. At the top, the 14 lesions for which FFR values above and below the threshold of 0.80 are highlighted.

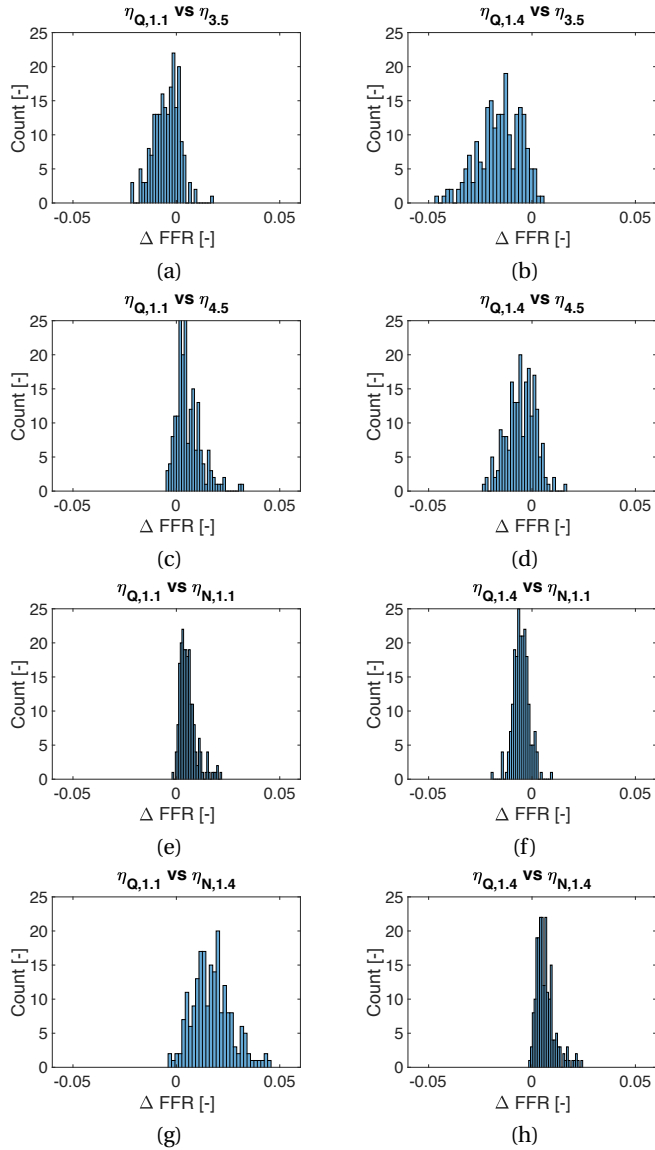


Figure 2.6: Histogram of the FFR differences between the Quemada model and the four Newtonian models. All of the Newtonian models are compared against the Quemada model for both η_p (a-h).

A closer look at the differences between the Quemada model and the Newtonian approximations showed that depending on the parameter choice for the Quemada model there is either an overestimation or underestimation of the FFR by the Newtonian approaches (see Figure 2.6). Using $\eta_{3.5}$ tends to result in an overestimation of the FFR which increases with increasing η_p . However, using $\eta_{4.5}$ results only in an overestimation of FFR when the larger η_p is used in the Quemada model while underestimating FFR when the smaller η_p is used. The patient-specific Newtonian model tends to underestimate the FFR compared to the Quemada model for both plasma viscosities. Depending on the choice of viscosity model, the FFR can vary up to 0.065 with 95% of the cases showing a difference below 0.048; the variation in FFR for 26% to 53% of the cases is more than the measured reproducibility of FFR ($\sigma_{FFR} = 0.02$, $\sigma_{FFR} = 0.03$) (Gaur et al., 2014b; Berry et al., 2013). It is important to note that the overestimation and underestimation of FFR by the Newtonian models is shown to be correlated with the hematocrit. Each of the Newtonian approaches is shown to correlate well with the Quemada model only for a certain hematocrit value. An FFR result based on $\eta_{3.5}$ corresponds best with the result based on the Quemada model for smaller values of H_{ct} independent of the chosen η_p . Increasing H_{ct} increases the overestimation of FFR by the Newtonian models as can be seen in Figure 2.8a. The result based on $\eta_{4.5}$ corresponds best for a hematocrit of 0.50 when using the smaller η_p for the Quemada model, and with decreasing hematocrit, the FFR underestimation was shown to increase. On the other hand for the larger η_p , a similar overestimation from using $\eta_{4.5}$ occurs as from using $\eta_{3.5}$. When using a Newtonian approach with patient-specific H_{ct} , the underestimation of the FFR increases with increasing H_{ct} .

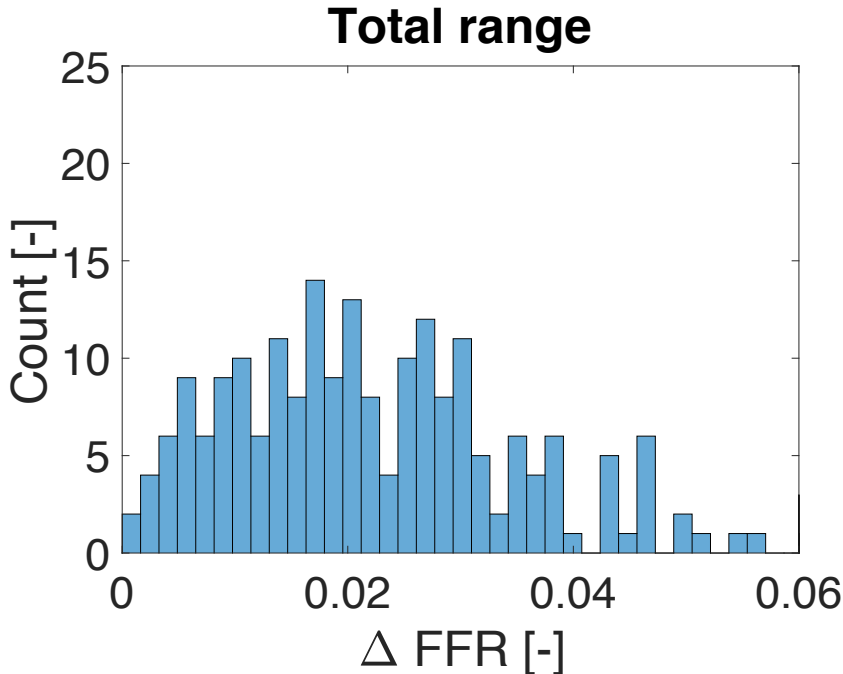


Figure 2.7: Histogram of the absolute FFR ranges resulting from the six different viscosity models for all 206 lesions.

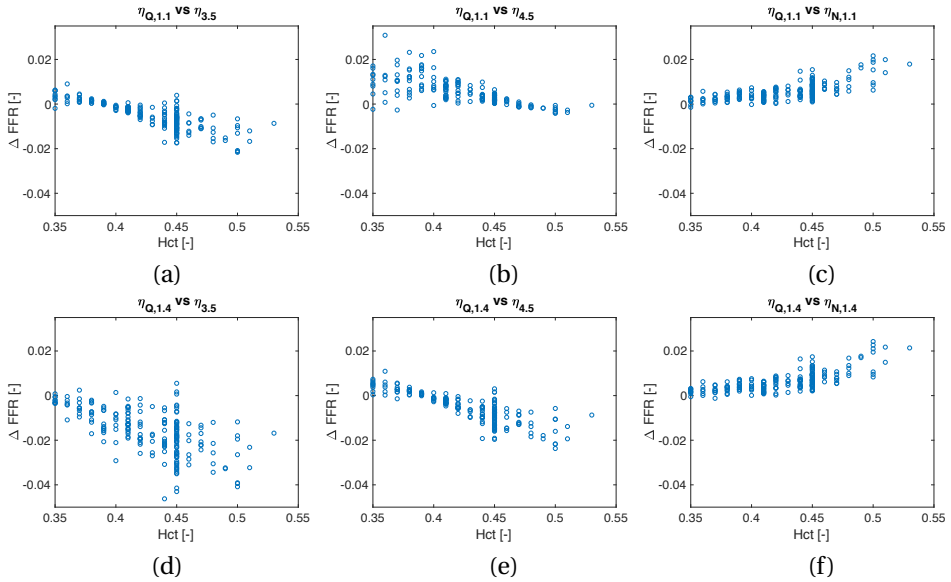


Figure 2.8: FFR differences are depicted between the Quemada model and the Newtonian models as a function of the hematocrit. The difference in FFR is calculated as the FFR with the Quemada model minus the FFR with the Newtonian model.

2.4 Discussion

The aim of this study was to investigate the impact of various blood viscosity models on the computed FFR. The FFR used in this study is derived from the time-averaged pressure proximal and distal to the stenosis, similar to what is used in the clinic for determining the physiological severity of a coronary stenosis. To this end we used a Newtonian approach with a constant value ($\eta_{3.5} = 3.5 \cdot 10^{-3} \text{Pa} \cdot \text{s}$, $\eta_{4.5} = 4.5 \cdot 10^{-3} \text{Pa} \cdot \text{s}$), a Newtonian approach with patient-specific hematocrit, and a non-Newtonian approach with the Quemada model for blood viscosity. Applying the different blood viscosity models on over 200 lesions, we investigated the effect of blood viscosity on the computed FFR. Our analysis showed that the FFR differences between the Newtonian models and the non-Newtonian model can vary by up to 0.065 and is also correlated to the hematocrit. We have furthermore shown that the differences in FFR can increase by varying the plasma viscosity.

2.4.1 Non-Newtonian simulations

The differences in FFR per lesion were found to be nonuniform across lesions. Investigating the impact of different blood viscosity models on the computed FFR has made clear that for a number of lesions (7%), the choice of blood viscosity model affects the classification of functional significance, as determined by a cutoff-value of 0.80.

For higher shear rates, blood viscosity approaches a plateau and becomes increasingly insensitive to changes in shear rate. This indicates that shear thinning for the Quemada model at high shear rates plays a minor role comparison to the choice of hematocrit and plasma viscosity.

Furthermore we have shown that each of the four Newtonian models has its characteristic hematocrit value for which it best matches the Quemada model. This characteristic hematocrit was found to change for different plasma viscosities.

For the current study we have included the measured hematocrit values which can be assessed in the clinic. However, this was done while using a population-based approach for the plasma viscosity by using values at the lower and higher range. Plasma viscosity is known to vary between 1.00 and 1.50 mPa · s; as such, the value that is chosen can have a significant impact on the computed FFR (Baskurt and Meiselman, 2003; Haidekker et al., 2002; Késmárky et al., 2008; Rand et al., 1964). A population-based approach for plasma viscosity will likely have less fidelity on a patient-specific basis, and the added uncertainty of the plasma viscosity contributes to the uncertainty in computed FFR.

In this study, the aim was not to perform a direct comparison of the computed FFR with the invasively-measured FFR for the various viscosity models, but rather to show that the choice of blood viscosity model can have a significant impact on the computed result, all else being equal. Future work would further investigate the impact of blood viscosity modeling on flow rates, velocity profiles and wall shear stresses. We have shown that the choice of blood viscosity model and the associated parameter values should be carefully considered, as the resulting variations in computed FFR may be greater than the reported reproducibility of invasively-measured FFR (Gaur et al., 2014b; Berry et al., 2013).

2.4.2 Limitations

One of the limitations of the study could be the use of constant steady boundary conditions. Flow through coronary arteries is known to heavily decelerate during systole as a result of myocardial contraction. Blood viscosity might be higher during systole as a result of the lower flow and thus lower shear rates. However, Sharp *et al.* (Sharp et al., 1996) argued that red blood cell aggregates are unlikely to occur in blood flowing in large arteries and if they occur, they are probably small in size. Furthermore, rouleaux degradation happens almost instantaneously. Aggregation on the other hand shows a characteristic time which is significantly longer than a cardiac cycle. Sharp *et al.* (Sharp et al., 1996) further argued that aggregations are unlikely to happen as shear rates increase throughout a large portion of the cross-section for at least a brief period of time during the cardiac cycle. Given these statements we expect the assumption of a steady flow to have small to negligible effect on the blood viscosity. Furthermore due to the increased flow during hyperemia, shear rates are expected to further increase compared to the resting state. The selection of the Quemada model may be deemed reasonable when considering the argument of Sharp *et al.* (Sharp et al., 1996) in combination with the high shear rates in this study.

2.4.3 Conclusion

This work is a first step towards understanding the effect on computed FFR of using a non-Newtonian blood viscosity compared to using Newtonian models. We have shown that when using different blood viscosity assumptions the computed FFR may vary significantly and result in possibly different diagnostic outcomes due to the 0.80 cut-off. We furthermore have shown that when employing the Quemada model, which in literature is shown to accurately capture the blood viscosity behaviour (Marcinkowska-Gapińska et al., 2007), the parameter values for hematocrit and plasma viscosity can significantly impact the FFR: these values should ideally be derived from reliable measurements on the patient.

Conflict of Interest

None

2.5 Acknowledgment

The authors would like to thank the Dutch institute IMDI- ZonMw for funding [Project number: 104003009].

Influence of population-based variance of blood viscosity on the uncertainty in computed fractional flow reserve

This chapter is based on: Influence of population-based variance of blood viscosity on the uncertainty in computed fractional flow reserve, **K. Gashi**, N. Xiao, E. M. H. Bosboom, S. Quicken, W. Huberts, C. A. Taylor, and F. N. van de Vosse, *Submitted*

Abstract

In this computational study, we investigated the impact of uncertainty in hematocrit and plasma viscosity on computed fractional flow reserve (FFR). The FFR was estimated using computational fluid dynamics (CFD) where the non-Newtonian constitutive behavior of blood was approximated with the Quemada model. To this end data of 68 patients (80 lesions) with patient-specific hematocrit values were considered. When the hematocrit is unknown and assumed to vary across a physiological range of values, the resulting variation in computed FFR was found to be as large as 0.08, which means that to 88% of lesions demonstrated a larger variance than the reported reproducibility of invasively-measured FFR in the clinic. Taking into account patient's hematocrit and only varying plasma viscosity, FFR variability decreased by more than a factor 2.2. Performing a sensitivity analysis, we found that 61% of the FFR uncertainty was due to uncertainty in the hematocrit and 38% was due to uncertainty in plasma viscosity. Knowledge of the hematocrit, which can readily be measured in the clinic, is vital for reducing the uncertainty in the computed FFR when employing the Quemada viscosity model.

3.1 Introduction

Measurement of the Fractional Flow Reserve (FFR) to determine the functional severity of a lesion in the coronary arteries is recommended by the guidelines of the European Society of Cardiology and the European Association for Cardio-Thoracic Surgery in order to refer the patient for coronary artery bypass grafting (CABG), percutaneous coronary intervention (PCI), or medicinal treatment. FFR is formally defined as the ratio between the time-averaged maximal hyperemic flow in a vessel with a stenotic lesion to normal maximal hyperemic flow in the same vessel. The FFR can be approximated by the ratio between the time-averaged pressure distal (p_d) to the lesion and the pressure proximal (p_a) to the lesion (Pijls et al., 1995). In the clinic, FFR is usually assessed via an invasive pressure measurement after hyperemic flow has been induced during coronary catheterization. Patients with an FFR 0.80 may receive percutaneous coronary intervention (PCI) or coronary artery bypass grafting (CABG), whereas patients with an FFR above 0.80 usually receive medicinal treatment. In retrospect the latter group of patients underwent an unneeded invasive FFR assessment. This applies to up to 50% of the patients that received a FFR measurement (Min et al., 2012; Koo et al., 2011; Nørgaard et al., 2014).

Recently, much effort has been focused on applying computational methods for non-invasively predicting FFR based on CT images (Taylor et al., 2013; Morris et al., 2013, 2015; Koo et al., 2011). When modeling blood flow, a common assumption is that blood can be treated as a Newtonian fluid. Many studies either employ a constant viscosity (Johnston et al., 2004; Mirramezani et al., 2019) or one based on patient data (Sankaran et al., 2012; Fossan et al., 2018). In reality, blood viscosity has been shown to be dependent on the hematocrit (H_{ct}) and plasma viscosity (η_p) which vary from patient to patient (Baskurt and Meiselman, 2003; Long et al., 2005). One of the main drawbacks for a Newtonian approach is that one assumes an effective shear rate *a priori* which is not known. This might have a significant impact on the computed FFR which especially around the threshold might affect decision-making. However, the exact influence of non-Newtonian blood viscosity on the computed FFR is unknown.

In this study, we therefore aim to examine the effect of variations in hematocrit and plasma viscosity on computed FFR. To this end the Quemada model which captures the shear-thinning behavior of blood and includes the input parameters, hematocrit and plasma viscosity has been used (Quemada, 1981, 1977). Whilst varying H_{ct} and η_p within their corresponding physiological ranges, we determined inter-patient variations in computed FFR using uncertainty quantification (UQ). The UQ approach is based on a global variance-based method which captures the uncertainty in variance. Using this UQ approach, sensitivity analysis (SA) was used to identify important parameters and quantify their effect on the output uncertainty (Quicken et al., 2016; Huberts et al., 2014). UQ in cardiovascular applications has been shown to be a valuable tool to gain insight into the relationships between the output and input variation and to select input parameters which reduce the output uncertainty (Chen et al., 2013; Sankaran et al., 2016; Quicken et al., 2016; Huberts et al., 2014). Using this approach the contribution relative to the FFR uncertainty for each parameter was investigated.

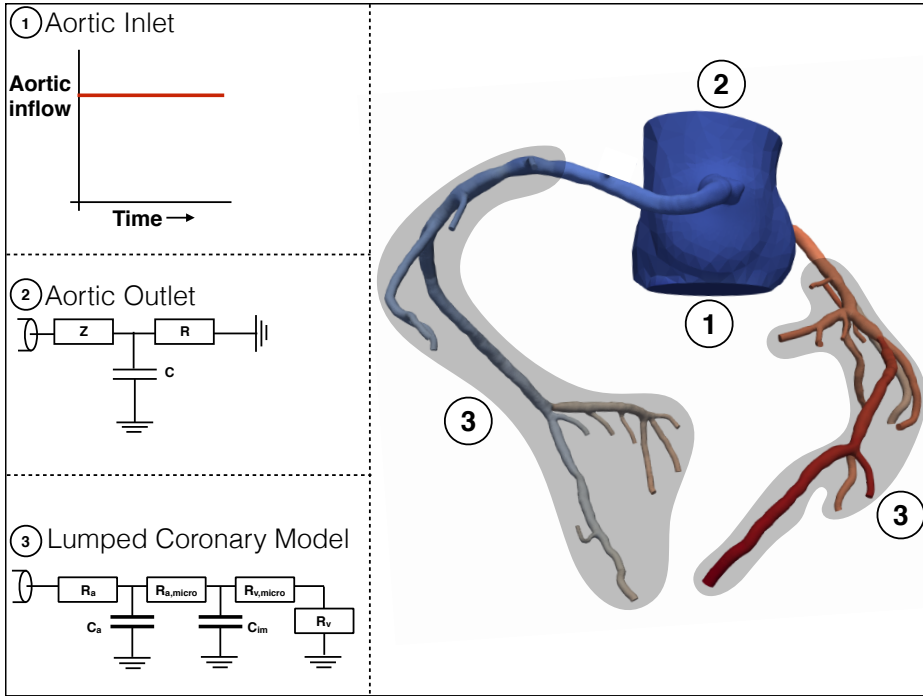


Figure 3.1: An overview of the boundary conditions applied at the aortic inlet (1), aortic outlet (2) and, coronary outlets (3). At the aortic inlet, a constant flow is prescribed whereas at the aortic outlet a three-element windkessel model is used. For the coronaries which are indicated in grey, at the outlets lumped coronary models are prescribed.

3.2 Materials and Methods

3.2.1 Patient specific geometries

Patient-specific geometries in this study were reconstructed from the CTA scans obtained from previous studies (Koo et al., 2011; Min et al., 2011). 68 patients (80 lesions) with measured hematocrit values were included. The median of the clinically measured FFR for the 80 lesions was 0.84 [95%CI: 0.5 - 0.97] whereas the median hematocrit values was found to be 0.44 [95%CI: 0.35 - 0.49]. Each patient's geometry consisted of a small part of the aorta with coronaries branching from the aorta (see Figure 3.1).

3.2.2 CFD modelling

The incompressible Navier-Stokes equations with non-Newtonian fluid viscosity were used to model coronary hemodynamics:

$$\rho \left(\frac{\partial \vec{u}}{\partial t} + \vec{u} \cdot \nabla \vec{u} \right) = -\nabla p + \nabla \cdot 2\eta(\dot{\gamma})\mathbf{D}, \quad (3.1)$$

$$\nabla \cdot \vec{u} = 0, \quad (3.2)$$

where \vec{u} and p are the velocity and pressure, respectively. The density, shear rate, shear rate dependent viscosity, and deformation rate tensor are denoted by ρ , $\dot{\gamma}$, $\eta(\dot{\gamma})$ and \mathbf{D} , respectively. The blood density ρ was set to 1060 kg/m^3 . Furthermore, vessel walls were assumed to be rigid. The shear rate ($\dot{\gamma}$) for incompressible flow is defined as (Spencer, 2004):

$$\dot{\gamma} = \sqrt{2|II_D|} \equiv \sqrt{|tr(\mathbf{D}^2)|} \quad (3.3)$$

where $|II_D|$ denotes the magnitude of the second invariant of the rate of deformation tensor \mathbf{D} ($\mathbf{D} = \frac{1}{2}(\nabla \vec{u} + (\nabla \vec{u})^c)$). It has been shown in the literature that the steady-state assumption provides reasonably accurate estimates for FFR compared to fully transient conditions (Fossan et al., 2018; Morris et al., 2017; Gashi et al., 2018). Therefore, at the aortic inlet (see Figure 3.1), a constant cardiac output was prescribed using a flat velocity profile. The coronary outflow resistances (Kim et al., 2010; Vignon-Clementel et al., 2006; Sankaran et al., 2012; Min et al., 2015; Taylor et al., 2013) to simulate baseline flow and hyperemic flow were determined using the estimated fraction of the left ventricular myocardial mass perfused by each coronary vessel. Based on the segmented left ventricular myocardium from the CTA images, the total baseline coronary flow is computed from the estimated cardiac flow demand. The baseline resistances of each individual coronary outlet boundary are computed from the estimated basal flow and morphometric relationships between flow rates and diameters. Maximal hyperemia is simulated by modeling the effect of a typical dose of adenosine by lowering the coronary outlet resistances to minimum values (Taylor et al., 2013). The outflow resistance at the aortic outlet (see Figure 3.1), representing the total systemic resistance, was adjusted together with the cardiac output to reproduce a realistic aortic pressure. The fluid equations were numerically solved with a stabilized, semi-discrete finite element method, using meshes containing linear tetrahedral elements with boundary layers at the vessel walls. FFR was calculated as $FFR = P_c/P_{Ao}$, where P_c is the steady-state pressure in the coronary artery, and P_{Ao} is the average pressure in the aorta.

3.2.3 Non-Newtonian model

A non-Newtonian constitutive model ($\eta(\dot{\gamma})$) based on the work of Quemada *et al.* was used (Quemada, 1981, 1983), where the blood viscosity is written as:

$$\eta(\dot{\gamma}) = \eta_p [1 - \frac{1}{2} K_Q(\dot{\gamma}) H_{ct}]^{-2}, \quad (3.4)$$

$$K_Q(\dot{\gamma}) = \left(\frac{k_0 + k_\infty \sqrt{\frac{\dot{\gamma}}{\dot{\gamma}_c}}}{1 + \sqrt{\frac{\dot{\gamma}}{\dot{\gamma}_c}}} \right). \quad (3.5)$$

The parameters η_p and H_{ct} represent the plasma viscosity and hematocrit, respectively. Intrinsic viscosities for $\dot{\gamma} \rightarrow 0$ and $\dot{\gamma} \rightarrow \infty$ are determined by k_0 and k_∞ whereas $\dot{\gamma}_c$ is defined as the characteristic shear rate of blood. K_Q will become k_0 for $\dot{\gamma} \rightarrow 0$ whereas K_Q will become k_∞ for $\dot{\gamma} \rightarrow \infty$. In this study, we used a reduced version of the five-parameter model ($\eta_p, H_{ct}, k_0, k_\infty, \dot{\gamma}$) containing two-parameters (η_p, H_{ct}) using the data from Oliver *et al.* (Oliver, 1986). The benefit of using a two-parameter model over a five-parameter model is that uncertainty and sensitivity analysis become more computationally tractable.

More importantly H_{ct} and η_p can be measured more readily in the clinic compared to k_0 , k_∞ and, $\dot{\gamma}$.

3.2.4 Numerical implementation

The blood viscosity model was implemented in such way that it was updated at every time step and Newton-Raphson iteration step throughout the simulation. Within each time step viscosity was calculated using the latest state of the velocity field. For numerical stability, simulations were started using a Newtonian approach by holding constant the shear rate for the Quemada model at 1000 s^{-1} . Later on, once an equilibrium for the pressure was achieved, the shear rate was made dependent on the velocity field. Simulations were performed using a time step of $1 \cdot 10^{-3} \text{ s}$ for a total simulation time of 0.2 s until a steady state solution was obtained. Simulations were performed on hosts with 32 cpu cores, 2.2GHz, 64GB of memory.

3.2.5 Uncertainty analysis & sensitivity analysis

The influence of uncertainty in H_{ct} and η_p on the uncertainty in the computed FFR was investigated by means of a global variance-based sensitivity analysis (SA). The global variance based method takes into account the expected reduction in output variance when a certain parameter is known (Huberts *et al.*, 2014). This method can be used to assess which parameter has the largest influence on the output variance and is therefore most important to know accurately. Furthermore, this approach takes possible interaction between input parameters into account. Another benefit of a global variance-based method is the fact that it does not depend on output-input relations and works for non-monotonic, non-linear and non-additive input-output responses. The SA was used to compute the so-called main Sobol sensitivity index for both H_{ct} and η_p . This index was calculated for every coronary lesion to investigate possible inter-lesion variation in main indices. Uncertainty in H_{ct} was assumed to be in the range of 0.35 - 0.55, which matches the reported physiological range (Marcinkowska-Gapińska and Kowal, 2009).

Based on the literature, the physiological range of the plasma viscosity was found to be between $1.10 \cdot 10^{-3}$ and $1.35 \cdot 10^{-3} \text{ Pa} \cdot \text{s}$ (Baskurt and Meiselman, 2003; Késmárky *et al.*, 2008). However, some researchers reported values outside of this physiological range (Rand *et al.*, 1964; Haidekker *et al.*, 2002). Therefore in this study, plasma viscosity was varied within a relative range of 20% of $1.25 \cdot 10^{-3} \text{ Pa} \cdot \text{s}$ so between $1.00 \cdot 10^{-3}$ and $1.50 \cdot 10^{-3} \text{ Pa} \cdot \text{s}$. We assumed a uniformly distributed uncertainty in both H_{ct} and η_p as the model input uncertainty distribution was unknown, which represents a 'worst case scenario'.

To assess the main indices we used the adaptive polynomial chaos expansion (agPCE) method, as described by Quicken *et al.* (Quicken *et al.*, 2016). This method adaptively builds a polynomial meta-model of the original model to analytically determine the main indices. It was shown that the agPCE method requires significantly fewer model evaluations for SA compared to traditional methods (Quicken *et al.*, 2016).

To build a meta-model, the agPCE method required the CFD model to be evaluated with random input samples, drawn from the model input uncertainty distributions. Twenty input samples were generated *a-priori* for each lesion using Sobol's low discrepancy series (Sobol', 1967). The number of simulations was a quasi-random number of simulations required for creating a full agPCE meta-model for a maximum polynomial degree of order

three including interaction. It has been heuristically shown that this choice is often sufficient for the agPCE method to create good quality meta-model (Quicken *et al.*, 2016). Given twenty simulations per lesion, multiple meta-models were generated using the agPCE algorithm. The value of the leave-one-out cross validation term, Q^2 was determined for each meta-model. The value of Q^2 , ranging between 0 and 1, is a quality measure of the meta-model and captures its predictive properties (Blatman and Sudret, 2010). In our analysis we required Q^2 to be at least 0.999. It was verified that at this value of Q^2 convergence of the sensitivity indices was reached: i.e. the sensitivity indices were invariant to a further increase of Q^2 .

In order to capture up to third order interaction terms for H_{ct} and η_p , 20 parameter sets were needed (Quicken *et al.*, 2016) which resulted in a total of 1360 simulations. Furthermore, these 20 parameter sets were required to describe a monotonically decreasing function of the blood viscosity as a function of the shear rate as observed by Oliver *et al.* for a similar range of shear rates (between 10^{-3} and 10^3 s^{-1}) (Oliver, 1986). In Figure 3.2, the Quemada blood viscosity is shown as a function of the shear rate for different parameter combinations. A typical monotonically decreasing viscosity function can be seen in Figure 3.2a whereas in Figure 3.2b a spike can be observed. None of the parameter combinations resulted in a spike within the shear rate range of interest between 10^{-3} and 10^3 s^{-1} .

To investigate the effect of uncertainty reduction when the value of H_{ct} was known, H_{ct} for each lesion was set to the measured value obtained from the patient whereas the η_p was varied as before. For these simulations only 10 evaluations per patient were necessary resulting in 680 additional simulations. The range of the measured H_{ct} was within 35 and 48 whereas the median was 44, similar to the physiological range noted in Marcinkowska *et al.* (Marcinkowska-Gapińska and Kowal, 2009).

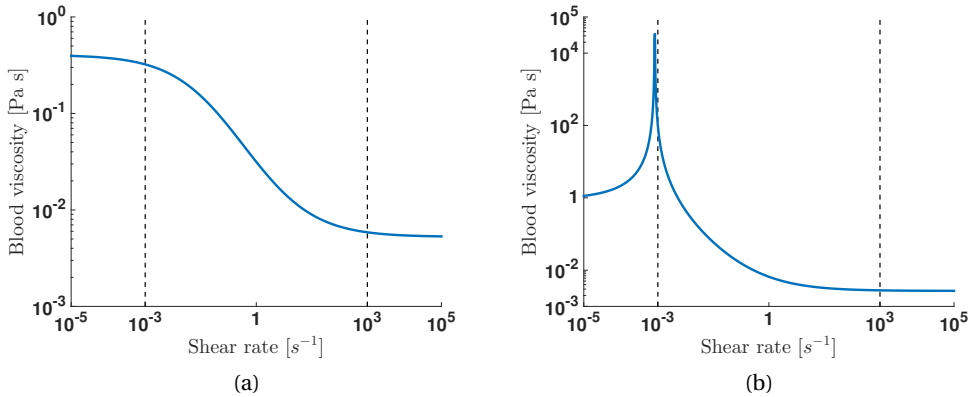


Figure 3.2: Example of a monotonic (a) and non-monotonic (b) decreasing blood viscosity for the Quemada model. The region of interest ($10^{-3} \leq \gamma_c \leq 10^3 \text{ s}^{-1}$) for which the viscosity needs to be monotonically decreasing is indicated between the dashed lines. For the monotonic curve $H_{ct} = 0.35$ and $\eta_p = 1 \text{ mPa} \cdot \text{s}$ were used whereas for the non-monotonic curve $H_{ct} = 0.55$ and $\eta_p = 1.25 \text{ mPa} \cdot \text{s}$ were used.

3.3 Simulations & analysis

3.3.1 Non-Newtonian simulations

Boxplots with the computed FFR for all 80 lesions are shown in Figure 3.3. The ranges of computed FFR values per lesion resulted from the chosen ranges of hematocrit and plasma viscosity. If we compare the median computed values to the common diagnostic cut-off value of 0.80 then 31 lesions were classified as functionally significant. However, up to 40 lesions may be deemed significant depending on the parameter value within the uncertainty range. The FFR cut-off value of 0.80 lies within the FFR prediction range of 15 lesions. This means that the decision to perform an invasive treatment could change

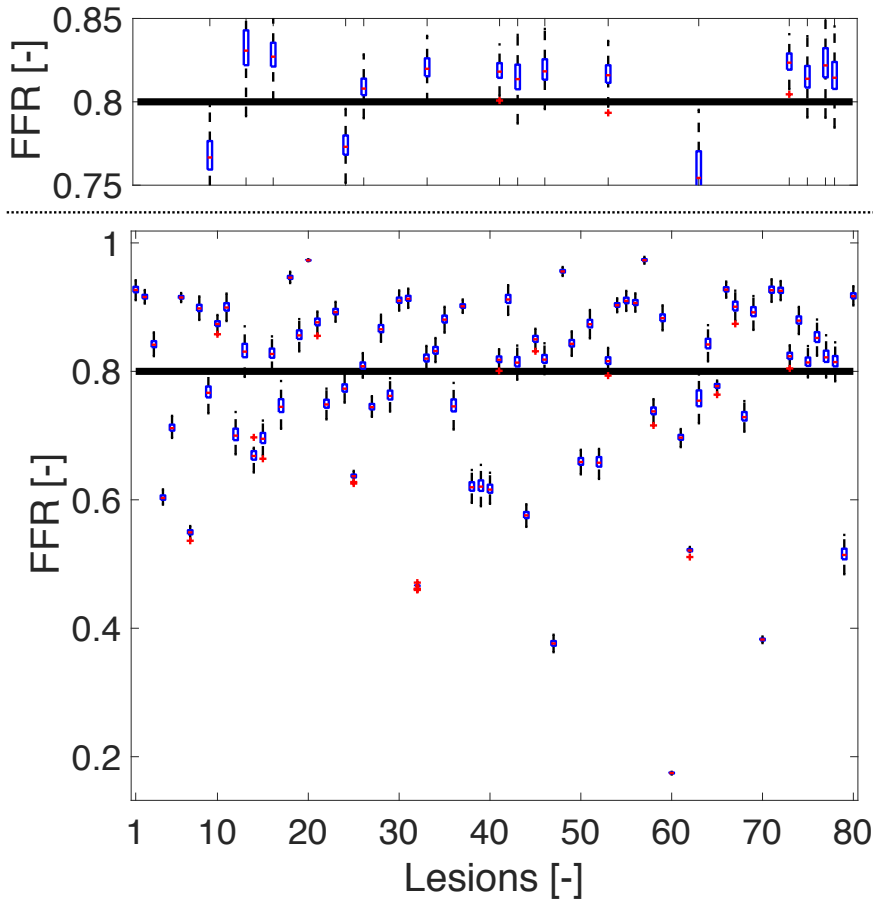


Figure 3.3: Depicted FFR values for the 80 lesions with their corresponding boxplots for unknown hematocrit and plasma viscosity. The red lines in the boxes represent the median whereas the horizontal edges of the boxes represent the 25th and 75th percentile of the data. The black dotted lines represent the whiskers which are 1.5 times the interquartile range. Outliers are represented with a red cross. The black line represents the clinical FFR cut-off value of 0.80. At the top, the 15 lesions which cross the FFR threshold of 0.80 or are close to it are highlighted.

for these lesions depending on the chosen value for H_{ct} and η_p assuming that all other variables such as geometry and boundary conditions are constant. Including patient-specific H_{ct} values largely decreases the uncertainty as shown in Figure 3.4. The range of computed FFR values shrinks by a factor of 1.1 and 3.4 (average of 2.2). The number of lesions for which the range in computed FFRs intersects with the 0.80 cut-off value is reduced from 15 to 6. Lesions 9 and 46 from Figure 3.4 crossed the threshold of 0.80, however including H_{ct} measurements results in both lesions having a minimum FFR of 0.81.

In Figure 3.5 the coronary tree with four stenoses and four FFR locations is shown. For each FFR location the FFR range due to uncertainty in both H_{ct} and η_p and, due to solely η_p is

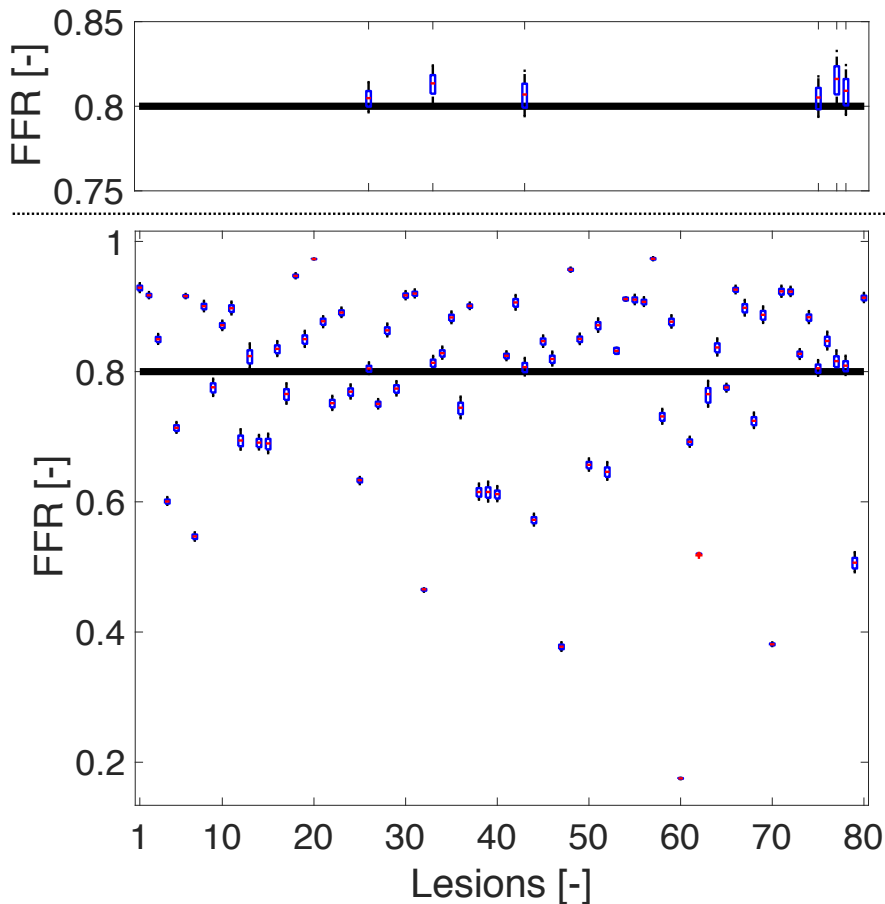


Figure 3.4: Depicted FFR values for the 80 lesions with their corresponding boxplots for known hematocrit and unknown plasma viscosity. The red lines in the boxes represent the median whereas the horizontal edges of the boxes represent the 25th and 75th percentile of the data. The black dotted lines represent the whiskers which are 1.5 times the interquartile range. Outliers are represented with a red cross. The black line represents the clinical FFR cut-off value of 0.80. At the top, the lesions which cross the FFR threshold of 0.80 are highlighted.

shown.

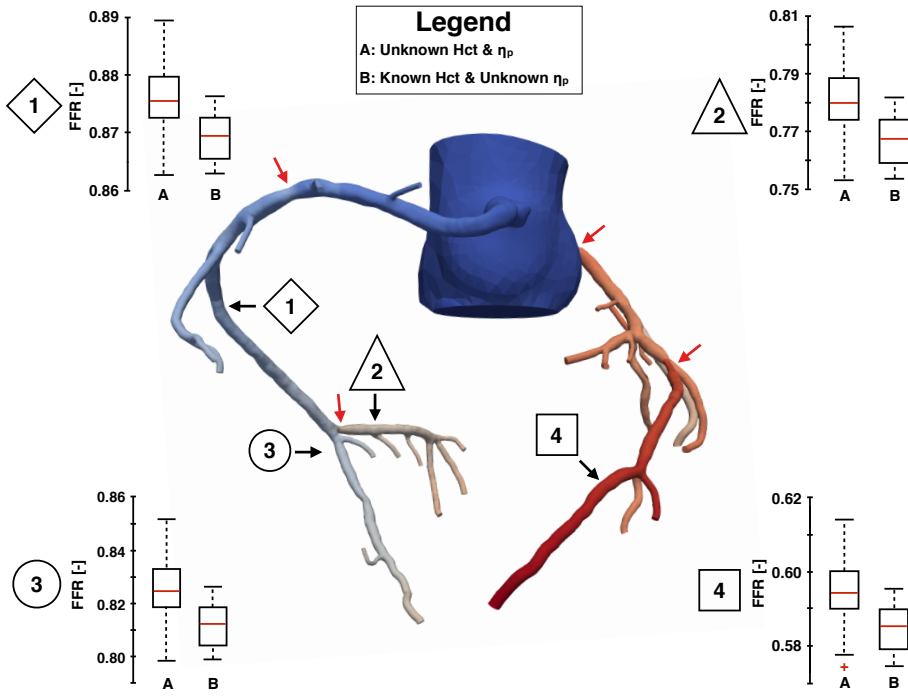


Figure 3.5: The computed FFR for the coronary circulation. The FFRs for the Quemada model at four different locations are indicated with arrows and their corresponding number. For each lesion, the uncertainty in the FFR is given with a boxplot. This is done for unknown hematocrit and plasma viscosity (A) and for known hematocrit and unknown plasma viscosity (B). Stenoses locations are indicated with red arrows.

For all patients and parameter sets, the total range of computed FFR values lies within 0.17 and 0.98 as can be seen in Figure (3.6a). The largest variation in FFR is found to occur between a FFR of 0.57 and 0.93 (Figure (3.6b)). Based on the choice of hematocrit and plasma viscosity, the range in FFR uncertainty can be as large as 0.079 (see Figure 3.6 (a&b) with 71% to 88% of the lesions showing larger discrepancies than the measured reproducibility of invasive FFR ($\sigma_{FFR}=0.02$ or $\sigma_{FFR}=0.03$) (Gaur et al., 2014b; Berry et al., 2013). Including the patient's measured hematocrit was shown to decrease the computed FFR uncertainty such that 11 to 40% of the lesions show an uncertainty range larger than the measured FFR reproducibility. The maximum FFR uncertainty range decreased to 0.04 as can be seen in Figure 3.6 (c&d).

3.3.2 Sensitivity analysis

All meta-models contained a maximum polynomial degree of 3. Furthermore, interaction up to the third order ($H_{ct}^2\eta_p, H_{ct}\eta_p^2$) were found although, being in the order of 1%, these interaction terms for all patients were small. For the ranges that were chosen, H_{ct} has the

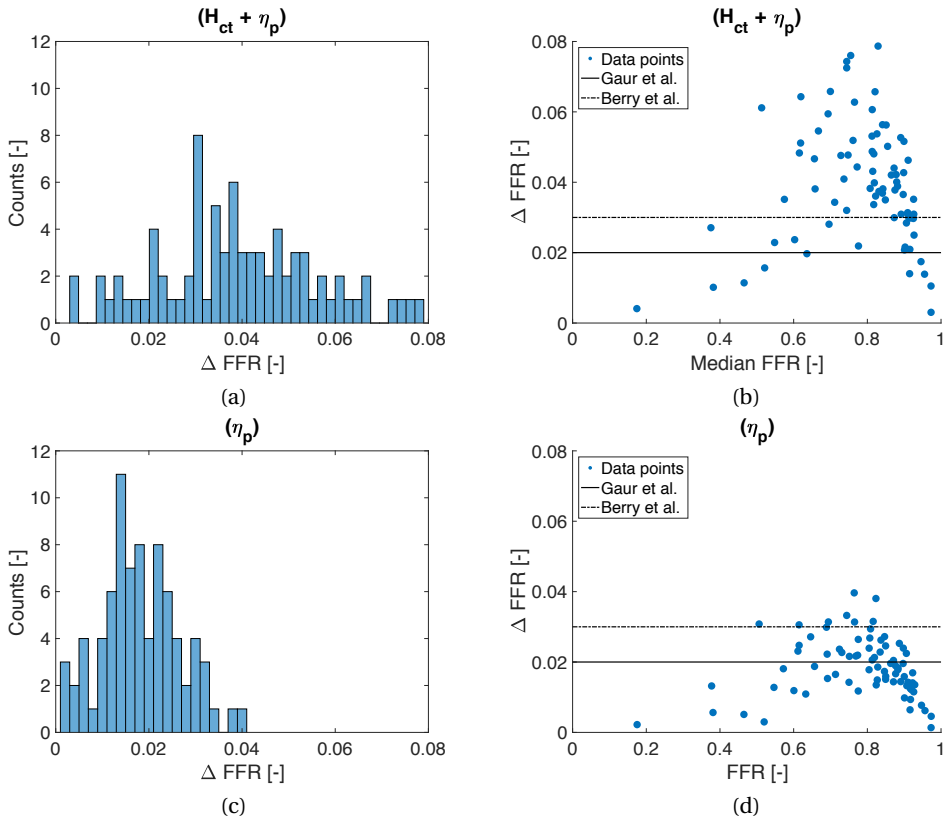


Figure 3.6: Histogram of the range in FFR uncertainty ΔFFR for 80 lesions for both unknown hematocrit and plasma viscosity (a). In (c) the ΔFFR histogram for a known hematocrit and unknown plasma viscosity is depicted. Scatter plots of the ΔFFR as a function of the median FFR are depicted in (b) and (d) for both unknown hematocrit and plasma viscosity and, only known hematocrit, respectively. The dashed and solid lines in (b) and (d) represent the measured reproducibility found by Berry *et al.* (Berry *et al.*, 2013) and Gaur *et al.* (Gaur *et al.*, 2014b), respectively.

largest influence on the uncertainty of the computed FFR. Based on the main sensitivity index for the lesions, approximately 61% [95%CI: 52% - 65%] of the FFR uncertainty can be attributed to the H_{ct} whereas 38% [95%CI: 35% - 45%] can be explained by η_p . The main indices show small inter-patient variations for both H_{ct} and η_p as seen in Figure 3.7. This implies that the influence of variations in H_{ct} and η_p does not depend on the lesion.

3.4 Discussion

The aim of this study was to investigate the impact of uncertainty in the parameters of a hemotocrit-based non-Newtonian model on the computed FFR. In addition we used a Quemada model for blood viscosity. Applying sensitivity analysis (SA) we investigated the effect of uncertainty in the hematocrit and blood plasma viscosity on the computed FFR. Our analysis showed that, using a hematocrit-based non-Newtonian model with a known

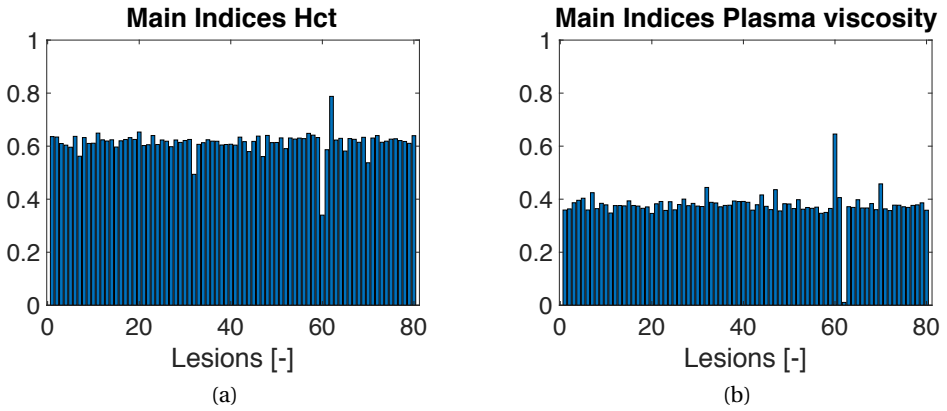


Figure 3.7: The main Sobol indices for 80 lesions for the hematocrit (a) and plasma viscosity (b) using the Quemada model.

hematocrit value significantly reduces the uncertainty in computed FFR.

3.4.1 Non-Newtonian simulations

We have investigated the uncertainty in predicting FFR for 80 lesions. The uncertainty in computed FFR was not the same for all lesions, ranging from 0.003 and 0.079. For a number of lesions (19%), the input uncertainty will have a significant effect on the final treatment. For a FFR cut-off value of 0.80, 15 lesions would receive different treatment depending on chosen parameters. This means that approximately 1 out of 5 lesions could be diagnosed either as significant or non-significant depending on the chosen input parameters.

We have shown that one should exert caution regarding the parameter value choice when using the Quemada model. Despite the higher fidelity of the Quemada model for describing the constitutive behavior of blood compared to the Newtonian approach, significantly different FFR predictions can be obtained depending on the choice of model parameters. For a population-based range of input uncertainties with unknown hematocrit and plasma viscosity, up to 88% of lesions showed a larger uncertainty than the invasive FFR reproducibility (Gaur et al., 2014b; Berry et al., 2013). This changed to 40% of lesions when the hematocrit was known. Therefore a population-based approach will not suffice on an individual basis. Furthermore including a measured hematocrit still leaves remaining uncertainty in the plasma viscosity, not to mention any measurement errors associated with the hematocrit measurement itself. Therefore uncertainty quantification for the Quemada model is still recommended even if hematocrit is measured.

3.4.2 Sensitivity analysis

Sensitivity analysis showed that 61% of uncertainty in computed FFR was due to variations in the hematocrit. Approximately 38% could be attributed to variations in plasma viscosity. Small inter-patient differences in the main indices for both H_{ct} and η_p were observed. The variability in computed FFR showed larger differences from patient to patient. Since the

range in plasma viscosity ($1.00 \cdot 10^{-3} - 1.50 \cdot 10^{-3} \text{ Pa} \cdot \text{s}$) that was used is larger than the reported physiological range ($1.10 \cdot 10^{-3} - 1.35 \cdot 10^{-3} \text{ Pa} \cdot \text{s}$) we can expect that the relative role of H_{ct} may even be underestimated (Baskurt and Meiselman, 2003; Késmárky et al., 2008). The η_p range was chosen to be larger for two reasons: first, the ranges for both H_{ct} and η_p were chosen to be approximately the same ($\pm 20\%$) such that the main indices were based on the same relative range, and second, there have been reports of plasma viscosities outside the physiological range (Haidekker et al., 2002; Rand et al., 1964).

In this paper, we only accounted for the uncertainty due to variations in blood viscosity when using the Quemada model. Other parameters such as myocardial resistance, aortic pressure and also geometry were assumed to be exactly known. In this way, the effect of the blood viscosity on the FFR could be investigated under the assumption that all other parameters were known. As there is interplay between viscosity, geometry and flow, a full sensitivity analysis combining the input uncertainties in geometry and boundary conditions will be helpful for probing these dependencies. In a recent study, Sankaran *et al.* have investigated the influence of uncertainty in lumen diameter, myocardial resistance, lesion length and Newtonian blood viscosity on FFR_{CT} (Sankaran et al., 2016). Based on their findings, blood viscosity had a similar impact as the myocardial resistance on the FFR. The findings in this paper regarding FFR uncertainty are similar to what Sankaran *et al.* found using a Newtonian blood viscosity. Both studies showed that accurate blood viscosity should be included to lower uncertainty in computed FFR.

3.4.3 Limitations

It must be noted that in this study we chose to only include the uncertainty of blood viscosity assuming the other parameters were known at a higher accuracy. The uncertainties in other parameters such as geometry, myocardial resistance, inflow boundary conditions and, mean arterial pressure were not considered. In this context, this study has shown that blood viscosity significantly impacts FFR even if other parameters are measured with high accuracy. To compare the effect of blood viscosity on the computed FFR against the effect of other parameters (Fossan et al., 2018; Sankaran et al., 2016), a more extensive analysis is needed. However, including additional parameters significantly increases the number of model evaluations needed to obtain Sobol indices (Donders et al., 2015) to the point that 3D CFD models may become unfeasible to evaluate. A solution might involve reduced order models for uncertainty quantification and sensitivity analysis when investigating the effect of additional parameters (Fossan et al., 2018; Morris et al., 2017; Gashi et al., 2018).

3.4.4 Conclusion

When FFR is computed with the Quemada viscosity model, the largest influence on the output uncertainty comes from uncertainty in the input hematocrit value. Knowledge of patient-specific hematocrit greatly reduces the variations in FFR predictions.

Conflict of Interest

-

3.5 Acknowledgment

The authors would like to thank the Dutch institute IMDI- ZonMw for funding [Project number: 104003009].

The influence of model order reduction on the computed fractional flow reserve using parameterized coronary geometries

This chapter is based on: The influence of model order reduction on the computed fractional flow reserve using parameterized coronary geometries, **K. Gashi**, E. M. H. Bosboom, and F. N. van de Vosse, In: *Journal of Biomechanics*, 2018;

Abstract

Computational fluid dynamics (CFD) models combined with patient-specific imaging data are used to non-invasively predict functional significance of coronary lesions. This approach to predict the fractional flow reserve (FFR) is shown to have a high diagnostic accuracy when comparing against invasively measured FFR. However, one of the main drawbacks is the high computational effort needed for preprocessing and computations. Hence, uncertainty quantification may become unfeasible. Reduction of complexity is desirable, computationally inexpensive models with high diagnostic accuracy are preferred. We present a parametric comparison study for three types of CFD models (2D axisymmetric, Semi-3D and 3D) in which we study the impact of model reduction on three models on the predicted FFR. In total 200 coronary geometries were generated for seven geometrical characteristics *e.g.* stenosis severity, stenosis length and vessel curvature. The effect of time-averaged flow was investigated using unsteady, mean steady and a root mean square (RMS) steady flow. The 3D unsteady model was regarded as reference model. Results show that when using an unsteady or RMS flow, predicted FFR hardly varies between models contrary to using average flows. The 2D model with RMS flow has a high diagnostic accuracy (0.99), reduces computational time by a factor 162,000 and the introduced model error is well below the clinical relevant differences. Stenosis severity, length, curvature and tapering cause most discrepancies when using a lower order model. An uncertainty analysis showed that this can be explained by the low variability that is caused by variations in stenosis asymmetry.

4.1 Introduction

Coronary heart disease is characterized by plaque buildup within the arterial wall resulting in stenoses. Stenoses may impair myocardial perfusion such that myocardial ischemia may occur during exercise or even rest (Stary et al., 1995). To determine the correct treatment for a stenosis, its hemodynamic severity needs to be assessed. This can be done by determining the fractional flow reserve (FFR) which is approximated by the ratio between the (intra-vascular measured) time-averaged pressure distal and proximal to the stenosis (Pijls et al., 1995). In multiple large randomized-control clinical trials FFR is shown to be reliable for classifying stenoses (Pijls et al., 2007; Tonino et al., 2010; De Bruyne et al., 2014). However, measuring FFR is an invasive procedure that needs catheterization. Retrospectively, up to 50% of the catheterizations was unnecessary as these patients only needed medicine treatment (Min et al., 2012; Koo et al., 2011; Nørgaard et al., 2014). Using computational fluid dynamics (CFD) models, the invasive nature of FFR assessment could be omitted (Morris et al., 2013, 2015; Nakazato et al., 2013; Tu et al., 2014). With, in general, 3D CFD models, FFR can be computed based on CT or other imaging data only, hence without the use of intra-vascular pressure measurements. One of the main drawback of these models is the fact that they are computationally expensive (Morris et al., 2017). Depending on the amount of computational resources and simulated physical time, simulations can last somewhere between minutes (Tu et al., 2014) for a steady approach until hours to days for a transient approach (Morris et al., 2017). The 3D approach works straightforward for full 3D scans (CT or MRI) compared to single-plane or bi-plane angiograms where 3D models of vessels need to be reconstructed first (Chen and Carroll, 2000; Çimen et al., 2016). Reconstructing semi-3D geometries using angiographic data for FFR predictions yields promising results as illustrated by Morris *et al.* (Morris et al., 2013). Although the semi-3D approach makes FFR predictions based on angiographic data possible, it still remains computationally expensive (Morris et al., 2017). The Semi-3D approach depends on the number of available images and the angle between images. Therefore, stenosis asymmetry might be caused by possible misrepresentation of stenoses resulting from insufficient number of images from single-plane and bi-plane angiograms. It is not yet clear what the benefit of a full 3D approach is and to what extent a semi-3D approach is accurate enough or if it even can be further reduced to 2D. In previous research the effect of curvature, torsion and stenosis severity has been shown to have an effect on the velocity profiles and wall shear stress (Katritsis et al., 2010; Chang and Tarbell, 1988; Hayashi and Yamaguchi, 2002). To which extent this might affect FFR predictions when applying a reduced order model needs to be investigated.

For an accurate prediction of the FFR, CFD models need to include uncertainty for boundary conditions and geometry. Variation of a few voxels in the lumen segmentation of a stenosis can yield an opposite diagnosis (Sankaran et al., 2015). In a later study, it was shown that myocardial resistance can have a similar impact on the FFR as the minimal lumen diameter (Sankaran et al., 2016). To include uncertainty in CFD models, computational time needs to be minimal to allow for multiple model evaluations. Itu *et al.* has shown promising results using a reduced order model (Itu et al., 2016). Therefore, we propose a parametric comparison study for three types of CFD models with different complexities which if needed can be extended for example for more accurate representation of non-Newtonian blood viscosity. The first model is the full 3D model which generally results from CT data segmentation (Taylor et al., 2013; Min et al., 2012; Nørgaard et al., 2014). This model resembles the physiological situation the most as it captures most of the

geometrical features. The second model is the semi-3D model which is characterized by its symmetric contours along the centerline of the geometry (Morris et al., 2015, 2017; Tu et al., 2014). The semi-3D model results from angiogram data segmentation of the centerline and effective radius. Third is the 2D axisymmetric model which is a simplified semi-3D model. The centerline loses its curvature and torsion and becomes a straightend tube with only one slice from centerline to wall (Morris et al., 2016).

Model complexity is also influenced by whether a model is evaluated for the steady or unsteady case. Evaluating unsteady models increases computational costs as simulations need to be performed until a steady-state solution is achieved.

The goal of this study is to investigate to what extend less complex models can be used while still maintaining their accuracy with respect to 3D models. For this, a large number of parametrized coronaries are constructed for three model types using various geometrical features such as stenosis severity, stenosis length, curvature, tapering, etc. Using uncertainty analysis, the effect of each geometrical feature on the predicted FFR is investigated and quantified features that have the largest effect on the predicted FFR are determined. The uncertainty analysis is expanded to the steady and unsteady case for the models to compare the steady and unsteady approach.

4.2 Material and Methods

4.2.1 Geometry definition

To quantify the impact of different model assumptions, 200 idealized coronary artery geometries were made. Seven parameters were set for each geometry: stenosis severity, stenosis asymmetry, stenosis length, curvature, torsion, angular stenosis position and tapering. Construction of the geometry was done in five steps. The first step was to create straight tubes with diameter of 2.8 mm and a length of 95 mm which correspond to either left or right coronary arteries (Tu et al., 2014). Symmetric stenoses were added with predefined severities using the following relation:

$$s(z) = \frac{r(z)}{r_{ref}} = \begin{cases} 1 + \frac{1}{2}s_r(\cos(\frac{\pi}{l_{si}}(z - z_i)) - 1), & \text{if } z_i \leq z \leq z_i + l_{si} \\ 1 - s_r, & \text{if } z_i + l_{si} < z < z_o - l_{so} \\ 1 + \frac{1}{2}s_r(\cos(\frac{\pi}{l_{so}}(z - z_o)) - 1), & \text{if } z_o - l_{so} \leq z \leq z_o \end{cases} \quad (4.1)$$

With, s_r representing the stenosis severity expressed in radius reduction. The variable z represents the longitudinal position. Furthermore, the positions and lengths of the stenosis inlet and outlet are given by z and l_s , respectively. Parameters with respect to inlet and outlet are indicated with the subscripts i and o , respectively. Next, the stenosis was moved in radial direction using the asymmetry index which was defined as:

$$a(z) = \begin{cases} r_{ref} \cdot s_r \cdot a_{ref} \cdot [\frac{1}{2} - \frac{1}{2} \cos(\pi \frac{z - z_i}{l_{si}})], & \text{if } z_i \leq z \leq z_i + l_{si} \\ r_{ref} \cdot s_r \cdot a_{ref}, & \text{if } z_i + l_{si} < z < z_o - l_{so} \\ r_{ref} \cdot s_r \cdot a_{ref} \cdot [\frac{1}{2} + \frac{1}{2} \cos(\pi \frac{z - z_o - l_{so}}{l_{so}})], & \text{if } z_o - l_{so} \leq z \leq z_o \end{cases} \quad (4.2)$$

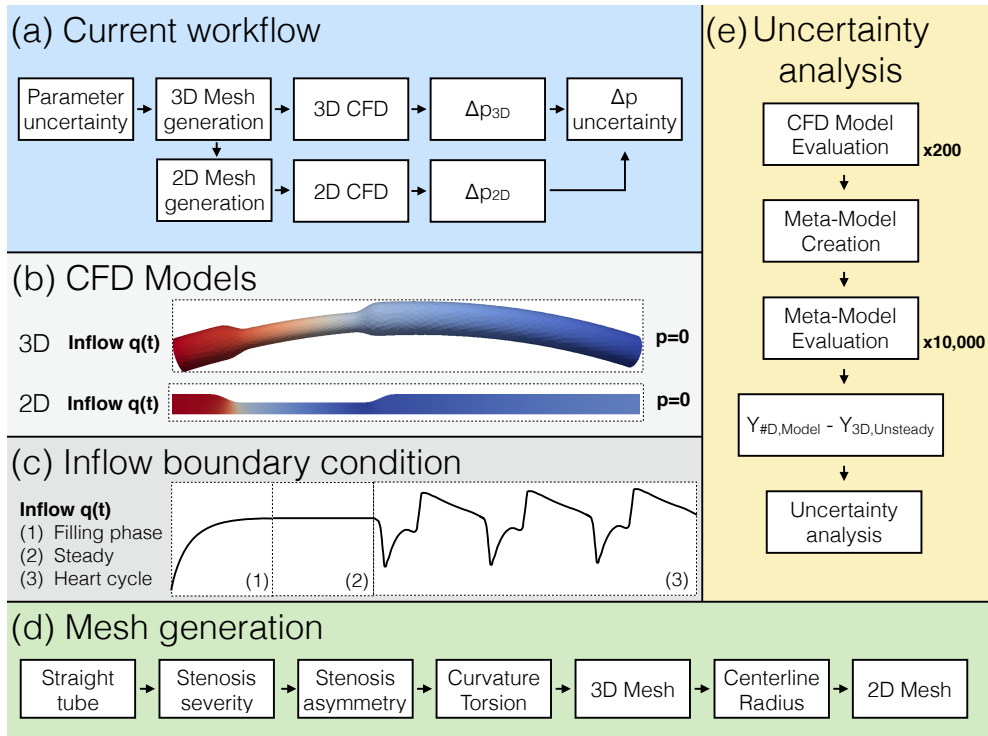


Figure 4.1: Schematic overview of the simulation study. In (a) based on parameter uncertainty 3D, semi-3D and 2D meshes are generated. The obtained pressures are used to determine which parameter of the geometry influences the pressure drop prediction the most. As shown in (b), all CFD models have a stress-free boundary condition at the outlet whereas at the inlet a flow-driven approach is applied. The applied flow (c) consists of three parts. A filling phase (1 s) is used to bring the system to the correct flow, the flow is then kept constant for 1.15 s where after four heart cycles (4 s) were imposed. The mesh generation (d) starts with a straight tube on which a stenosis severity is imposed. The stenosis can then be located either at the center of the vessel or moved to the outer side of the vessel depending on the asymmetry of the stenosis. Next, the geometry obtains its curvature and torsion based on the Frenet-Serret formulas. Once the 3D mesh is constructed, centerline and radius can be extracted such that a 2D axisymmetric mesh can be constructed. For each model, meta-models (e) are generated based on the parameter sets and output of interest. Using these meta-models, a large set of model output is generated based on the properties of the original CFD model. For each model the output is compared against the 3D unsteady model and uncertainty analysis is performed.

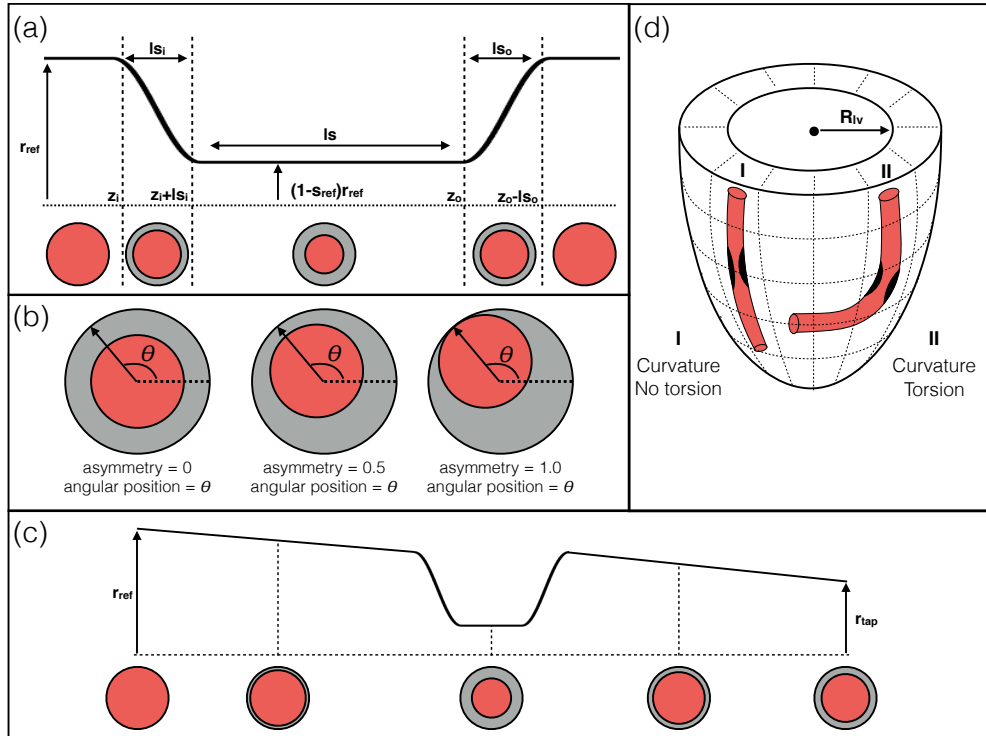


Figure 4.2: The definition of all seven parameters used to define the geometries are shown. The lumen is shown in red whereas the original lumen in case of stenosis is shown in grey. An example of a stenosis is shown in (a) where the stenosis length and severity are freely varied. The stenosis can then be shifted towards a desired position using a predefined asymmetry and angular position (b). Tapering of the vessel (c) (continuous radius reduction) is applied to mimic the *in vivo* situation when travelling more distal. Different alignment of coronary arteries is shown in (d). Here two distinct cases are shown, only curvature (I) and curvature in combination with torsion (II).

Herein, r_{ref} , a_{ref} are the predefined radius and the asymmetry index. The asymmetric translation of the stenosis is given by:

$$\begin{bmatrix} x(z) \\ y(z) \end{bmatrix} = s(z) \begin{bmatrix} x_0(z) \\ y_0(z) \end{bmatrix} + a(z) \begin{bmatrix} \cos(\theta) \\ \sin(\theta) \end{bmatrix} \quad (4.3)$$

Herein $x_0(z)$ and $y_0(z)$ are the original coordinates perpendicular to the longitudinal direction whereas $x(z)$ and $y(z)$ correspond to the new deformed coordinates when applying a stenosis and asymmetry. The angular position of the stenosis is given by θ . For the semi-3D geometries no asymmetry is applied such that $a(z)$ remains 0 for all Semi-3D cases.

The third step was to apply curvature and torsion to mimic 3D behaviour of coronaries by modifying the centerline using Frenet-Serret formulas:

$$\begin{bmatrix} \mathbf{T}' \\ \mathbf{N}' \\ \mathbf{B}' \end{bmatrix} = \begin{bmatrix} 0 & \kappa & 0 \\ -\kappa & 0 & \tau \\ 0 & -\tau & 0 \end{bmatrix} \begin{bmatrix} \mathbf{T} \\ \mathbf{N} \\ \mathbf{B} \end{bmatrix} \quad (4.4)$$

Herein \mathbf{T} and \mathbf{N} are the vectors tangent and normal to the direction of the centerline, respectively. The binormal vector (\mathbf{B}) is defined as the cross product of \mathbf{T} and \mathbf{N} . Furthermore, the curvature and torsion of the centerline are represented with κ and τ , respectively.

Over the full length of the vessel tapering was applied, meaning the radius along the vessel was reduced by a predefined radius reduction.

3D tetrahedral meshes with boundary layer and finer meshed stenosis were generated using VMTK (Antiga et al., 2008). A full 3D mesh convergence study was performed for an area-reduction of 50% and 90% with mesh sizes of 1.4 and 1.6 million elements, respectively. Number of elements for 3D models ranging between 290,000 and 350,000 were shown to be sufficient as the pressure drop differed less than 2% with respect to the finest meshes. For the 2D models, 4000 to 7000 elements were needed as the difference in pressure drop was also below 2% compared to the finest mesh of 40,000 elements. For semi-3D models the asymmetry index was zero with the same meshing approach as described above. For 2D models, meshes were created using centerlines and radius profiles of 3D geometries. Centerlines were mapped on a linear coordinate such that the radius profile was a function of the centerline length. 2D axisymmetric meshes with bi-quadratic quadrilateral elements and a boundary layer were created using the finite element software SEPRAN (TU Delft, the Netherlands) (Segal, 1989).

4.2.2 CFD model

For this study, blood flow was governed by the incompressible Newtonian Navier-Stokes equations given as:

$$\rho \left(\frac{\partial \vec{u}}{\partial t} + \vec{u} \cdot \nabla \vec{u} \right) = -\nabla p + \nabla \cdot 2\eta \mathbf{D}, \quad (4.5)$$

$$\nabla \cdot \vec{u} = 0, \quad (4.6)$$

with \vec{u} the velocity, p the pressure, and \mathbf{D} the rate of deformation tensor. The dynamic viscosity η is set to be $3.5 \cdot 10^{-3}$ Pa·s whereas ρ is set at 1050 kg/m^3 . For the 3D simulations, Fenics was used in combination with OASIS using the incremental pressure correction method (Alnæs et al., 2015; Mortensen and Valen-Sendstad, 2015). For 2D simulations an in-house finite element package (TFEM) was used (Hulsén, 2007). For the 3D and 2D simulations a time step of 0.1 ms and 1 ms was used, respectively.

4.2.3 Boundary conditions

Flow boundary conditions at the inlet were chosen to represent hyperemic flow and to be stenosis dependent. This was done using the non-linear relationship between coronary flow reserve (CFR) and stenosis severity found in literature (Gould, 2009; Wei et al., 2001; Miller et al., 1994). For low severities, CFR and thus flow are invariant to stenosis severity as CFR remains almost constant. For certain stenosis severities CFR decreases exponentially with eventually no blood flow for higher severities. This non-linear behaviour was used to derive a severity flow relationship using the following assumptions. **1)** Flow was assumed to be only zero for a total occluded blood vessel (Gould, 2009). Although, in the approach of Wei the flow was shown to be zero while still some lumen area remained open, this was assumed to be due to collateral flow (Wei et al., 2001). **2)** Flow was also estimated in absence of a stenosis. From the work of for example Min *et al.* and Kim *et al.* it can be observed

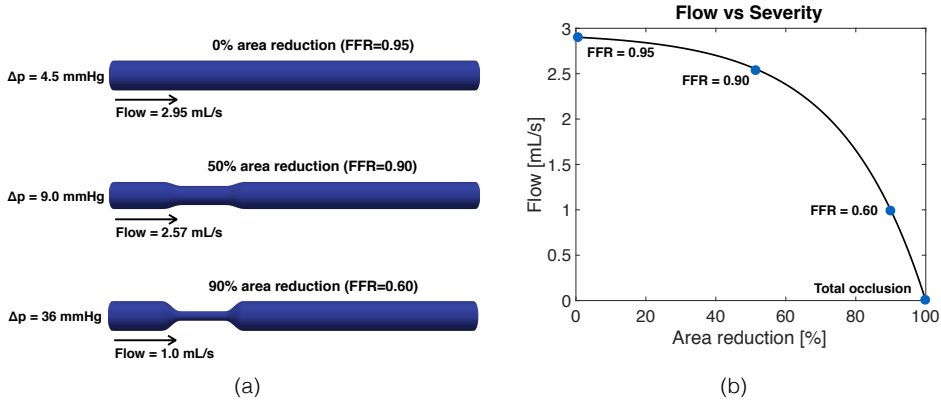


Figure 4.3: Obtaining a relationship between flow and stenosis severity by estimating the flow for four different stenosis severities. For this, typical FFR values for different severities were used from literature. In (a) the three geometries for which the flow was estimated are shown. The resulting relation between severity and flow is shown in (b).

that coronary arteries proximal to the stenosis have a FFR close to 1 (Min et al., 2015; Kim et al., 2014). This means that before blood arrives at the stenosis, it already lost part of its pressure proximal to the stenosis. It was assumed that flow (q_{max}) without stenosis would result in a FFR of 0.95 based on literature (Min et al., 2015; Kim et al., 2014). **3)** FFR for a 50% and 90% area reduction stenosis was assumed to be around 0.85 - 0.9 and 0.6, respectively based on literature (Tonino et al., 2010; Johnson et al., 2013). For this purpose, flows were estimated for two geometries with an area reduction of 50% and 90% by increasing the flow until the corresponding FFR was found (Tonino et al., 2010; Johnson et al., 2013). These two flow values (q_{area50} , q_{area90}) in combination with q_{min} and q_{max} were then used to obtain the non-linear relationship between severity (S_A) and the prescribed flow at the inlet (q) of the form: (Gould, 2009; Wei et al., 2001; Miller et al., 1994)

$$q = q_{max} \cdot (1 - \exp(-b \cdot S_A)), \quad (4.7)$$

$$S_A = \frac{A_{stenosis}}{A_{ref}} = \frac{r_{stenosis}}{r_{ref}} = (1 - s_r)^2, \quad (4.8)$$

where q_{max} and b are the flow without stenosis and an exponential decay constant, respectively. As q_{max} was known, only the decay constant (b) needed to be fitted. This resulted in a non-linear relationship between flow and severity as found in literature with q_{max} and b equal to 2.95 mL/s and 4.119, respectively (Gould, 2009; Wei et al., 2001; Miller et al., 1994). **4)** For the transient coronary flow behavior, a typical left coronary flow curve was used with high flow during diastole and low flow during systole (Boron and Boulpaep, 2012; Hall, 2015). The mean of the transient flow curve was scaled using Equation 4.7. **5)** As for this study flow was prescribed, by definition, the pressure drop was calculated using the Navier-Stokes equation instead of the patient's arterial pressure. Hence for the last assumption the mean arterial pressure was assumed to be 90 mmHg (12 kPa) (Tang et al., 2009; Wilson et al., 1988; Taylor et al., 2013). Using the pressure drop (Δp) and mean arterial

pressure (\bar{p}_a), the FFR was calculated as follows:

$$FFR = 1 - \frac{\Delta p}{\bar{p}_a}. \quad (4.9)$$

For the steady simulations both average and root mean square (RMS) of the transient flow signal were used. The mean flow (\bar{q}) was used to investigate how well it scales with the predicted FFR which itself is a ratio between the time-averaged pressure distal and proximal to a stenosis (Pijls et al., 1995). The RMS of the flow (q_{rms}) takes into account the shape of the flow signal, weighing the peaks of the signal higher compared to lower values. The equations for mean flow and the RMS flow are given as:

$$\bar{q} = \frac{\sum_{i=1}^n q_i}{n}, \quad (4.10)$$

$$q_{rms} = \sqrt{\frac{\sum_{i=1}^n q_i^2}{n}}, \quad (4.11)$$

here, q_i represents a discrete flow value of the flow signal consisting of n points. In Figure (4.4a) a coronary flow with corresponding mean and root mean square is shown. The root mean square of the flow for this study was shown to be slightly higher compared to the mean flow. Furthermore, the influence of increased retrograde flow on the mean and root mean square of the flow is shown in Figure (4.4b).

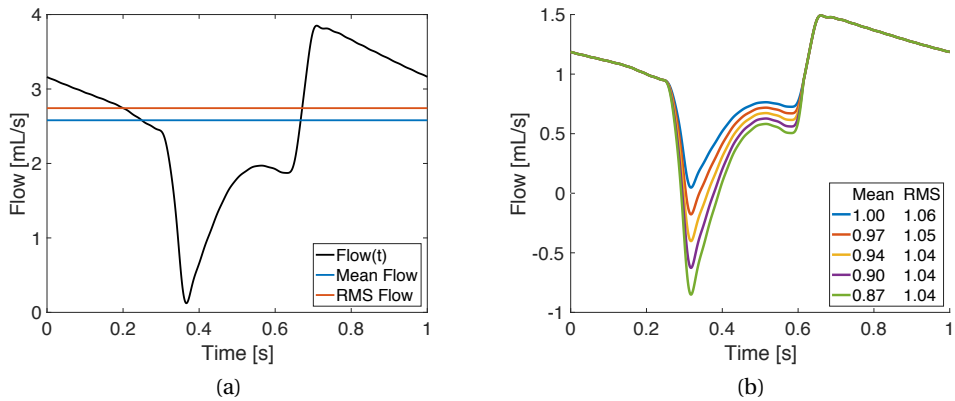


Figure 4.4: In (a) an example of a transient flow curve (black) is shown which is applied for the 2D, semi-3D and 3D models. Furthermore, the mean (blue) and root mean square (red) of the flow curve are indicated. An example (b) of changing mean and RMS flow is shown for an increase in regurgitant flow.

For stable simulations, a start-up phase was introduced where the flow was gradually increased for 1 second to either the mean or RMS for the transient flow curve. Next, the inflow was kept constant for 1.15 second to obtain a steady solution. Next, 4 heart cycles of 1 second were imposed.

Table 4.1: Geometrical features used in this study with their corresponding minimum and maximum value.

	Minimum	Maximum
Severity [%]	50	90
Asymmetry [-]	0	1
Length [mm]	5	10
Curvature [cm^{-1}]	0	0.887
Torsion [cm^{-1}]	0	0.286
Angular position [-]	0	2π
Tapering [%]	0	20

4.2.4 Uncertainty analysis

Parameter variation for mesh generation are shown in Table 1. Tonino *et al.* showed that stenoses with an area reduction between 50% and 70% were most difficult to distinguish as either functionally significant or non-significant (Tonino *et al.*, 2010). On average 35% of these stenoses were functionally significant. For stenoses with an area reduction between 70% and 90%, approximately 80% of stenoses were functionally significant. In this study the area reduction of stenoses was varied between 50% and 90% as visual assessment of these stenoses did not correspond well to functional assessment (Tonino *et al.*, 2010). In order to capture various kind of asymmetric stenoses, the stenosis asymmetry was varied between perfectly symmetric (0) and fully asymmetric stenosis against the wall (1). The effective stenosis length was varied between 5 and 10 mm similar to what was shown in Tonino *et al.* and Sankaran *et al.* (Tonino *et al.*, 2009; Sankaran *et al.*, 2016). Both the inlet and outlet of stenosis were kept constant at 2 mm. Waksman *et al.* investigated the curvature and cyclic curvature of coronary arteries for 38 patients (Waksman *et al.*, 2013). Therefore, the broadest curvature range was assumed ranging between 0 and 0.887 cm^{-1} . For the torsion of coronary arteries, a left ventricular radius of 3.5 cm was expected. This way the minimum (no circumference alignment) and maximum (pure circumference alignment) torsion ranged between 0 and 0.286 cm^{-1} . Due to the 3D nature of coronary vessels, a stenosis can be located either on the inside of the bend or on the outside. Therefore, the angular stenosis position was varied independently of the curvature and torsion between 0 and 2π radials. For the vessel tapering, up to 20% radial reduction was assumed (Itu *et al.*, 2016). An important assumption was that parameter ranges were uniformly distributed corresponding to the worst case scenario as the likelihood of occurrence was the same. The unsteady 3D model was assumed to be the reference model ('golden standard') as it best represents the physiological situation, hence all other models were compared against the reference. The comparison between models was done by investigating the performance for each model and performing uncertainty analysis on geometry parameters. Uncertainty analysis was done in three steps. First, for every combination of CFD models either steady or unsteady, a meta-model was created using the adaptive polynomial chaos expansion (agPCE) method (Quicken *et al.*, 2016) which described the pressure drop for the chosen set of parameters. The main benefit of the agPCE method is the adaptive way meta-models created. Polynomial terms that do increase the meta-model quality significantly are added to the model. On the other hand terms that do not improve meta-model quality are removed. This way only significant terms are kept such that a lower number of CFD model evaluations is needed. Second, these meta-models were evaluated for 10000 samples.

Computational costs were substantially lower as new pressure drops within the chosen parameter range could be predicted. Finally, differences in output for the 3D unsteady meta-model and other meta-models were analyzed by comparing the main and total Sobol indices which were computed as described by Quicken *et al.* (Quicken *et al.*, 2016). This way, geometrical features causing large pressure drop discrepancies were identified.

4.2.5 Post-processing

For post-processing, the pressure drop along the centerline was calculated. This was done by generating a plane perpendicular to the centerline for each centerpoint. For each plane along the centerline, the average pressure is computed resulting in a pressure drop along the centerline. The maximum pressure drop was extracted and used to calculate the minimum FFR per geometry. Pressure drops and FFRs obtained from the 2D and 3D models were compared against the reference model. To determine the predictive power of each model, indicators such as the diagnostic accuracy, sensitivity and specificity of each model were investigated.

4.3 Results

We first compare the results of our models to the findings in literature. Next the models are benchmarked against the unsteady 3D model (Reference). Next, the impact of varying seven geometrical characteristics on the predicted FFR and pressure drop for the idealized model are investigated.

4.3.1 Verification

Simulated hemodynamics were shown to be in good agreement with previous studies (Katrtsis *et al.*, 2010; Chang and Tarbell, 1988; Hayashi and Yamaguchi, 2002; Kelidis and Konstantinidis, 2018). For the 2D, Semi-3D and 3D models the recirculation zone was found to increase with increase in stenosis severity (Katrtsis *et al.*, 2010; Kelidis and Konstantinidis, 2018). Furthermore, for the Semi-3D and 3D case velocity profiles were found to match the ones found in curved tubes (Chang and Tarbell, 1988; Hayashi and Yamaguchi, 2002; Kelidis and Konstantinidis, 2018)

4.3.2 Model comparison

Comparison of predicted FFRs for 200 geometries for each model against the 3D unsteady model for both the steady and unsteady case can be seen in Figure 4.5. In general, steady models with RMS flow and unsteady models predict the best FFR. Steady mean flow tends to overestimate FFR more with decreasing FFR.

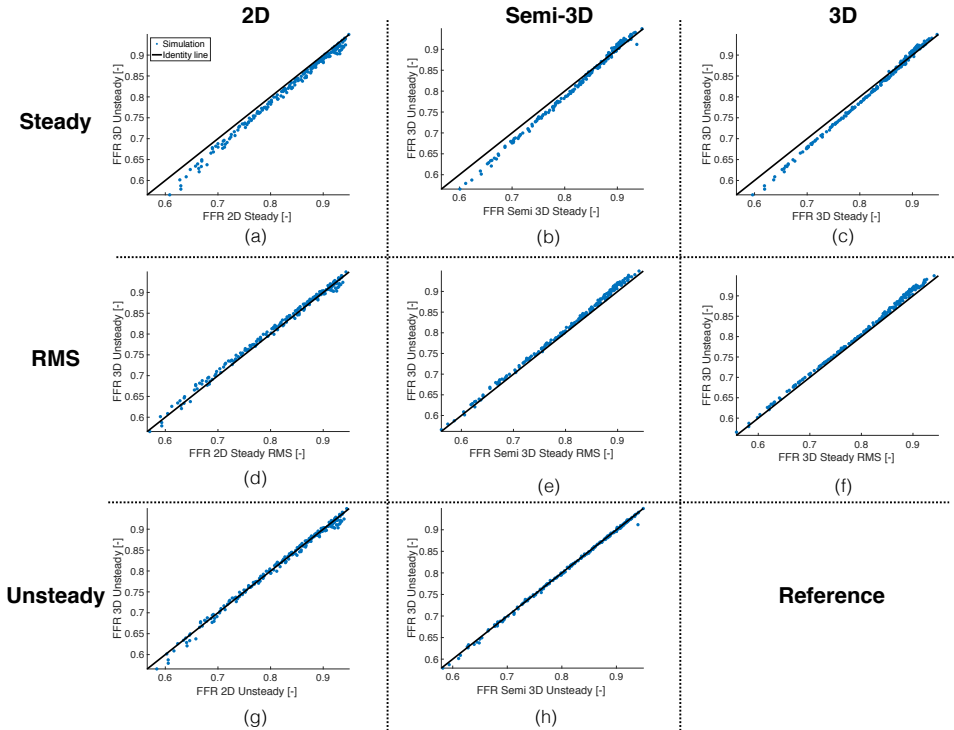


Figure 4.5: Computed FFR for all models (2D, Semi-3D and 3D) compared with the results of the 3D unsteady model. On the top row (a, b and c), the predicted FFR of the steady models is shown based on the average flow. On the second row, the results for the steady models with the root mean square of the flow is shown. At the bottom row, the unsteady 2D and Semi-3D model are shown.

To be able to replace the 3D unsteady model with a computationally less expensive model, the modelling error introduced due to change in model should be lower than the absolute error in FFR measurement reproducibility (Berry *et al.* (σ_{FFR} : 0.02); Gaur *et al.* (σ_{FFR} : 0.03)) (Gaur *et al.*, 2014a; Berry *et al.*, 2013). The largest absolute error in predicted FFR is found to be for the steady cases of the Semi-3D and 3D model which is $\sigma=0.012$ and thus at least 1.6 times smaller than what is found in clinic. The error for the unsteady models (2D, Semi-3D) is shown to be the lowest (Figure 4.6). On average, the absolute errors for the 2D and Semi-3D unsteady model are approximately 0.0052 and 0.0018, respectively. As shown before, the error increases for steady mean flow with decreasing FFR. Steady models underestimate the pressure drop by 6%, 6.1% and 7.8% for the 3D, Semi-3D and 2D model, respectively.

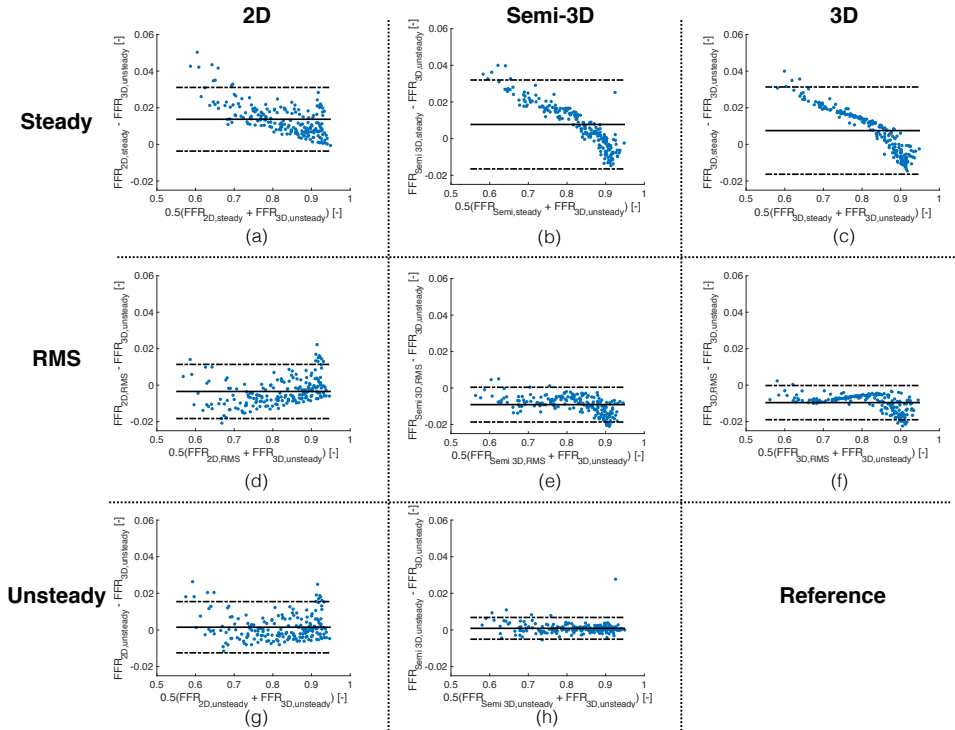


Figure 4.6: Differences in computed FFR for all models compared to the reference model shown in Bland-Altman plot. Mean and mean ± 1.96 std with the solid and dashed lines, respectively. On the top row, the difference are shown when using a steady model with a mean flow. The second row shows the result for the steady models with root mean square flow. On the bottom row, the differences in computed FFR for the unsteady 2D and Semi-3D models are shown.

The model also should predict the same treatment as the complex 3D unsteady model (FFR cut-off: 0.80). All models are shown to have a sensitivity of at least 0.97 whereas steady models show a sensitivity of 1 when using mean flows (See Table 4.2). Where steady models with mean flow have the highest sensitivity they also have the lowest specificity (0.93). When using RMS flow, steady models are shown to improve in specificity and PPV whilst maintaining a similar high (> 0.97) sensitivity and NPV (See Table 4.2). The accuracy of classifying stenoses correctly increases from 95 to 99% when using RMS flow instead of mean flow. For all steady RMS models the accuracy was 0.99 (See Table 4.2).

The 2D unsteady model has a specificity of 0.98. The diagnostic performance, classifying stenoses correctly, is shown to be at least 0.95. The 2D unsteady model has an accuracy of 0.98 meaning that from the 200 geometries, only 4 geometries were wrongly classified. In general predictions of the steady model with RMS flow are similar to predictions of the 3D unsteady model.

4.3.3 Uncertainty analysis

Around 170 of the 200 samples were needed to generate accurate meta-models. Furthermore, a maximum polynomial degree of third order (x_i^3) was found in all meta-models

whereas interactions up to third order ($x_i x_j^2$) were included. For each model different geometrical features are important. In general, differences in output between steady models and the reference model tend to occur mostly due to stenosis severity (Figure 4.7). Furthermore, geometry curvature plays a role for 2D models whereas torsion does not play a role at all. Overall, stenosis asymmetry, torsion and angular stenosis position do not influence predictions in FFR. When looking at the total Sobol indices, tapering is shown to be only important when considering 2D models and steady RMS models. Most discrepancies are caused by only four parameters *e.g.* stenosis severity, stenosis length, curvature and vessel tapering. Torsion and angular stenosis position are shown to have an almost negligible effect ($< 5\%$) on FFR differences. Similar is true for the angular position except for the Semi-3D RMS and 3D RMS models.

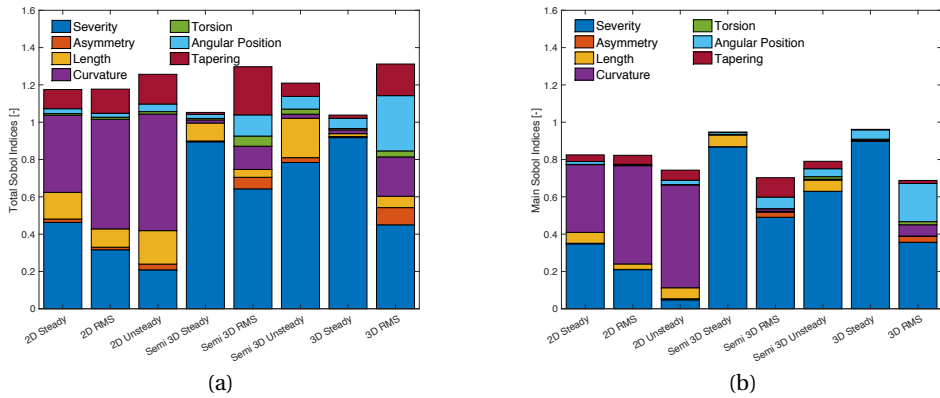


Figure 4.7: Main and total Sobol indices for seven parameters for each model benchmarked against the 3D unsteady model.

Table 4.2: Performance of the models regarding the sensitivity, specificity, positive predictive value (PPV), negative predictive value (NPV) and accuracy with respect to correct treatment prediction compared to the unsteady 3D model. Furthermore, the average CPU time which is defined as the elapsed real time x the number of cores used is given. Steady 3D and steady semi-3D are solved using the unsteady Navier-Stokes equations, the computational time when solving the steady Navier-Stokes equations is given in brackets which is based on Tu *et al.* (Tu *et al.*, 2014)

Model type	Sensitivity	Specificity	PPV	NPV	Accuracy	CPU time
2D Steady	1.00	0.93	0.88	1.00	0.95	2 s
2D Steady RMS	0.99	0.99	0.99	0.99	0.99	2 s
2D Unsteady	0.99	0.98	0.97	0.99	0.98	28 m
Semi-3D Steady	1.00	0.93	0.88	1.00	0.95	31 h [5 m]
Semi-3D Steady RMS	0.97	1.00	1.00	0.98	0.99	33 h [5 m]
Semi-3D Unsteady	1.00	0.99	0.99	1.00	0.99	95 h
3D Steady	1.00	0.93	0.88	1.00	0.95	30 h [5 m]
3D Steady RMS	0.97	1.00	1.00	0.98	0.99	32 h [5 m]
3D Unsteady	-	-	-	-	-	91 h

4.4 Discussion

The aim of this study was to investigate the effect of replacing the 3D unsteady CFD model with computationally less expensive models. Various parametrized geometries were constructed for various 3D geometry characteristics such as stenosis severity, stenosis asymmetry, curvature, etc. Then geometries were simulated with the different models (2D, Semi-3D, 3D). These models were shown to yield results which were in good agreement with previous studies (Katritsis et al., 2010; Kelidis and Konstantinidis, 2018; Chang and Tarbell, 1988; Hayashi and Yamaguchi, 2002; Kelidis and Konstantinidis, 2018). This approach allows ranking characteristics based on their effect on differences in FFR and pressure drops between different CFD models and 3D unsteady model (Reference).

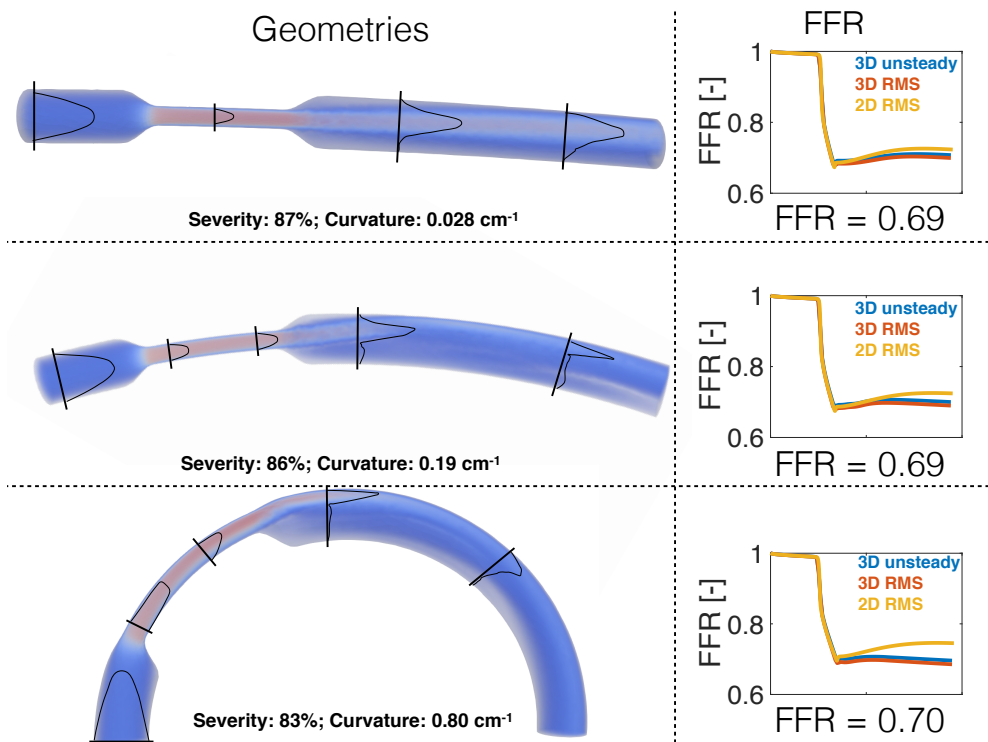


Figure 4.8: Schematic overview of three geometries with corresponding velocity profiles and FFRs along the centerline. On the left side geometries with the velocity profile are given with increasing curvature from top to bottom. Furthermore, velocity profiles as a function of the radius are given at multiple locations. Finally at the right side, the FFR as a function of the centerline is depicted for each geometry. This is done for the 3D unsteady (blue), 3D steady RMS (red) and 2D steady RMS (yellow) case.

4.4.1 Model comparison

We showed that when using unsteady models (2D, Semi-3D), predicted pressure drop and FFR match very well with the reference model. However, when using steady models, a corresponding effective flow needs to be chosen. In the current study, we have shown that

predicted pressure drop and FFR highly depend on this flow. Steady models overestimate FFR when using mean flow although FFR is defined as a time-averaged quantity (Pijls et al., 1995). This is probably due to the fact that mean flow does not take into account the shape of the flow curve. Contributions of short periods of high flow may be cancelled out when longer periods of low flow or even regurgitant flow occur when only taking the mean of a flow signal. When using the root mean square of the flow curve, the predicted FFR corresponds very well to the 3D unsteady FFR. When using the root mean square, the performance of steady models is shown to get closer to the 3D unsteady model. This can be explained by the fact that the mean flow can be close to zero with sufficient retrograde flow whereas the RMS takes into account the absolute flow curve.

Reducing model complexity yields smaller differences compared to the measured reproducibility in clinic (Gaur et al., 2014a; Berry et al., 2013). When using a mean flow for steady models, differences are shown to be slightly above the measured reproducibility for low FFR values. However, for the steady RMS and unsteady models, the differences remain below the reproducibility.

If we examine the hemodynamics a bit closer, we can see that with increasing curvature the velocity profile changes with high velocity at the outer side of the bend (Chang and Tarbell, 1988; Hayashi and Yamaguchi, 2002; Kelidis and Konstantinidis, 2018) (See Figure 4.8). Furthermore, recirculation zones right after the stenosis can be observed which vary in size depending on the stenosis severity similar to what was found in literature (Katritsis et al., 2010; Kelidis and Konstantinidis, 2018).

In this study we have shown three ways of reducing computational time while still maintaining a high diagnostic accuracy. **1)** Using a full-steady approach where only the steady Navier-Stokes equations are solved for. This effectively reduces the computational effort to the equivalent of solving a couple of time steps which takes around a couple of minutes instead of multiple hours. **2)** Using a 2D model instead of a Semi-3D or 3D model reduces computational time approximately by a factor 190 while still maintaining a high accuracy. Solving the full-steady 2D model takes on average 2 seconds to solve for while the 3D unsteady model usually takes around 90 hours and thus reduces computational time by a factor 162,000.

4.4.2 Uncertainty analysis

Uncertainty quantification for the different models shows that the different geometrical features do not influence the models in the same way. When using a 2D model, most of the uncertainty comes from the lack of curvature. This can also be seen in Figure 4.8. Although the 2D RMS model is able to capture the same drop in FFR as the 3D unsteady model, it shows a slight post-stenotic overestimation of the FFR. This effect becomes more pronounced when the curvature of the vessel is increased. For the Semi-3D and 3D model, stenosis severity is shown to play an overall dominant role in the uncertainty. On the other hand the role of the stenosis asymmetry, torsion and angular stenosis position is small when reducing the model order. Overall the severity is shown to have a far greater effect than asymmetry and angular stenosis position. This explains why predictions of the 2D and Semi-3D model are so close to the ones of the reference model whilst omitting these geometrical features.

4.4.3 Limitations

One of the limitations of this study is the fact that parameterized coronary geometries were used. Compared to *in vivo*, current geometries are considered smooth which might influence the predictive power of the models. Nonetheless results of this study are useful for future research using realistic geometries. In this study a proof of concept of the influence of various geometrical features on the predicted FFR is given where specific parts of FFR uncertainty can be attributed to a specific geometrical feature.

Another thing to note is that in this study only one stenosis per vessel is investigated. In future research the currently presented workflow could be extended in a straightforward way for multi stenosed vessels. However, we expect those difference not to change the conclusion regarding the model reduction and parameter importance. The results of this study have shown that given the current input, the 3D unsteady model can be replaced by less computational expensive lower order models.

4.5 Conflict of interest statement

None

4.6 Acknowledgment

The authors would like to thank the Dutch institute IMDI-ZonMw for funding [Project number: 104003009]

Uncertainty quantification for computed FFR using myocardial perfusion and left ventricular mass

This chapter is based on: Uncertainty quantification for predicted FFR using myocardial perfusion and left ventricular mass, **K. Gashi**, E. M. H. Bosboom, M. J. M. M. Hoeijmakers, M. Zreik, I. Išgum, T. Leiner, and F. N. van de Vosse, *Submitted*

Abstract

In this study we have investigated the impact of uncertainty in boundary conditions on the computed FFR using a computational fluid dynamics (CFD) model. Simulations for 14 patients were performed with boundary conditions based on left ventricular mass m_{lv} , myocardial perfusion, mean arterial pressure and, Murray's exponential constant for subdivision of myocardial resistance per branch.

We found that left ventricular mass accounts for 72% of the uncertainty in FFR. Perfusion and mean arterial pressure were shown to have a relative contribution of 19% and 8%, respectively. Murray's constant was shown to have a negligible contribution. Most of the FFR uncertainty occurred for patients with a low m_{lv} . Moreover, a linear decrease in FFR uncertainty was observed with increase in median FFR.

Even when including patients' m_{lv} with $\pm 5\%$ uncertainty, m_{lv} remained the most important parameter (51%) while the importance of MAP rose from 8% to 36%. However using MAP variation as found in literature was shown to decrease the MAP contribution in FFR uncertainty to approximately 10%, leaving left ventricular mass the most important parameter. In this study we found that m_{lv} should be measured as accurate as possible to most effectively decrease uncertainty in computed FFR given the four parameter that were investigated.

5.1 Introduction

A lot of research is aimed at performing non-invasive assessment of coronary artery disease using computational fluid dynamics (CFD) models by means of the derivation of virtual fractional flow reserve (FFR) (Taylor et al., 2013; Morris et al., 2015; Min et al., 2012; Itu et al., 2016). By first segmenting coronary arteries from imaging data such as CT and using the geometry endowed with appropriate boundary conditions, the patient's blood flow and pressure along the coronary tree can be computed. In this way invasive intra-vascular pressure measurement needed to measure the FFR in the clinic can be avoided. One of the main challenges of computing FFR using CFD models is obtaining correct boundary conditions. These boundary conditions are preferably patient-specific and based on non-invasively obtained and accurate patient data. Another challenge is the fact that CFD models for coronary circulation are computationally very expensive (Taylor et al., 2013; Morris et al., 2017) and thus can be cumbersome to evaluate within a given time frame when also uncertainty quantification is needed. Both challenges might result in the fact that especially uncertainty applied in the boundary conditions can not be used to enrich the corresponding patient's FFR with a confidence interval. This especially becomes important when the computed FFR is close to the threshold used to differentiate between various types of treatment.

One of the possible boundary conditions is coronary flow which depends on the size of the myocardium that needs to be supplied with blood. In general, coronaries supplying larger parts of the myocardium are expected to have more flow (Kassab, 2006; Choy and Kassab, 2008). Moreover, coronary flow is determined by perfusion of the myocardial tissue. Perfusion is amount of blood flow per unit of tissue mass. Another possible boundary condition is the mean arterial pressure which in healthy arteries together with the flow could determine the total myocardial resistance. A thing to note is that the same pressure drop will lead to a different FFR if the mean arterial pressure changes. The myocardial resistance needs to be divided accordingly among the various branches (Murray, 1926; Kassab, 2006; Fossan et al., 2018; Min et al., 2015) which will influence the flow distribution within the coronary circulation and thus the FFR throughout the coronary circulation. This distribution can be approximated by using allometric scaling laws based on geometrical input of the coronaries such as volume, length or radius (Kassab, 2006; Van der Giessen et al., 2011; Murray, 1926; Choy and Kassab, 2008). Some of the required parameters are more readily available from the clinical workflow such as the mean arterial pressure. Other parameters such as perfusion and myocardial mass need to be taken either from population-based ranges or need to be extracted using additional imaging modalities or post-processing.

In this paper, we investigate the effect of the uncertainty in the derived boundary conditions on the computed FFR. Boundary conditions in this study are derived from the parameters myocardial perfusion, left ventricular mass, flow distribution and mean arterial pressure. First parameters will be based on population-based ranges to obtain an uncertainty in FFR. Using this approach the parameters with the largest impact on the FFR are determined. Next, the left ventricular mass will be adapted using patient-specific values. This way the total reduction in FFR uncertainty is determined for the case that the patient's left ventricular mass is available.

5.2 Materials and Methods

For non-invasive FFR computations, boundary conditions of a patient need to be estimated by non-invasively obtained parameters. In this study the influence of the perfusion, left ventricular mass, flow distribution constants and mean arterial pressure were varied. Moreover, the reduction of FFR uncertainty due to including patient-specific measured left ventricular mass was investigated.

5.2.1 Data acquisition

For this study, 14 patients received a CCTA scan with corresponding measured FFR. The data were retrospectively obtained from the UMC Utrecht (Utrecht, the Netherlands). The study was furthermore approved by the Institutional Review Board committee (IRB). For the usage of the anonymized data, permission was given by means of written informed consent. The 14 patients (9 Male) had an average age of 60 years with a minimum and maximum age of 49 and 74 years, respectively. CCTA scans were acquired on a 256-detector row scanner (Phillips Brilliance iCT, Philips Medical, Best, The Netherlands). Acquisition was done using an ECG-triggered step and shoot protocol. The tube current was between 210 and 300 mAs whereas a tube voltage of 120 kVp was used. For patients > 80 kg contrast medium was injected using a flow rate was 6.7 mL/s a total of 80 mL iopromide (Ultravist 300 mg I/mL, Bayer Healthcare, Berlin, Germany), followed by a 67 mL mixed contrast medium and saline (50:50) flush, and next a 40 mL saline flush. For patients ≤ 80 kg the flow rate was 6.7 mL/s and the volumes of the boluses were 70, 50 and 30 mL, respectively. Images were reconstructed resulting in an in-plane resolution ranging from 0.38 to 0.56 mm, and 0.9 mm thick slices with 0.45 mm spacing.

5.2.2 Mesh generation

To obtain patient-specific meshes, the coronary arteries in the CCTA scans were first segmented using ITK snap (Yushkevich et al., 2006). Segmentation was performed either at the left or right side of the coronary circulation depending on the location of the measured FFR. Segmentation was performed from the ostium onward. For each segmentation a surface mesh of either the left or right coronary circulation was obtained. After segmentation, the obtained surface mesh was processed in SpaceClaim (Canonsburg, Pennsylvania, United States). Next the inlet and outlets were elongated. In general all branches were elongated until the original length of the vessel was restored. Inlet and outlet surfaces were generated to prescribed boundary conditions. Furthermore, to minimize boundary effects, branches were elongated to at least 10 times the radius. Once the surface meshes were processed, meshing was performed in Fluent (Canonsburg, Pennsylvania, United States). Meshes with an element size between 0.1 mm and 0.2 mm were generated.

5.2.3 Left ventricle segmentation

The left ventricle (LV) myocardium in coronary CTA was segmented using the method presented by Zreik *et al.* (Zreik et al., 2018). Briefly, to identify voxels of the LV myocardium, the algorithm uses multiscale convolutional neural network (CNN) that analyses two inputs, *i.e.* two image patches, centered around the voxel of interest. One input is a small patch taken at high-resolution allowing analysis of the detailed local texture but limited

contextual information. Another input is a larger image patch taken at low-resolution allowing analysis of the contextual information, but at reduced image resolution. The CNN combines information from both scales to classify all voxels in a CTA scan as LV myocardium or background.

5.2.4 CFD modelling

In this study, flows and pressures within the coronaries were solved using the incompressible Navier-Stokes equation assuming a Newtonian fluid:

$$\rho \left(\frac{\partial \vec{u}}{\partial t} + \vec{u} \cdot \nabla \vec{u} \right) = -\nabla p + \nabla \cdot 2\eta \mathbf{D}, \quad (5.1)$$

$$\nabla \cdot \vec{u} = 0, \quad (5.2)$$

with p and \vec{u} representing the pressure and velocity, respectively. The rate of deformation tensor is given by \mathbf{D} . Blood density and viscosity were set at 1050 kg/m^3 and $4.0 \cdot 10^{-3} \text{ Pa} \cdot \text{s}$, respectively. Blood flow and pressure were solved using the finite element package Fenics in combination with Oasis by means of the incremental pressure correction method (Alnæs et al., 2015; Mortensen and Valen-Sendstad, 2015). For all patients a time step of 0.1 ms was used.

5.2.5 Boundary conditions

In order to simulate a patient's blood flow and pressure, boundary conditions at the inlet and outlet of the coronary circulation need to be chosen wisely. At the inlet a steady coronary flow (q_{tot}) was prescribed based on the myocardial perfusion at rest, left ventricular size, hyperemic factor and, the side of the heart the coronary circulation is supplying. The corresponding steady coronary flow was prescribed at the inlet with a plug velocity profile as shown in Figure 5.1. The myocardial perfusion ($\text{mL}/(\text{gram} \cdot \text{min})$) at rest represents the amount of blood flow through a certain amount of myocardial tissue and is closely linked to myocardial oxygen consumption (Sharma et al., 2012). Using the tissue perfusion and the mass of the myocardial tissue of interest, the corresponding coronary flow of the tissue during rest can be estimated. The mass of the left ventricle can be obtained by using segmented left ventricular volume from CTA scans and assuming a myocardial tissue density of 1.055 gram/mL (Fuchs et al., 2016). The mass of the right ventricle was assumed to be half the size of the left ventricle (Sharma et al., 2012), hence no additional ventricular segmentation would be needed. To obtain blood flow during hyperemia, the rest flow needs to be multiplied with a certain hyperemic factor. The total coronary flow during hyperemia can be given as:

$$q_{tot} = \begin{cases} q_{per} \cdot m_{lv} \cdot f_{hyp} & \text{if left ventricle,} \\ 0.5 \cdot q_{per} \cdot m_{lv} \cdot f_{hyp} & \text{if right ventricle,} \end{cases} \quad (5.3)$$

with m_{lv} the myocardial mass in *gram*. The factor of flow increase during hyperemia is given by f_{hyp} which is 1 during rest and > 1 during hyperemia. For this study, we based our hyperemic factor on the coronary flow reserve (CFR) of 3.3 based on findings of Danad et al. (Danad et al., 2014). Using the total coronary flow (q_{tot}) and a mean arterial pressure

(\bar{p}_a), the total myocardial resistance (R_{tot}) was estimated as (Tang et al., 2009; Taylor et al., 2013):

$$R_{tot} = \frac{\bar{p}_a}{q_{tot}}. \quad (5.4)$$

The total myocardial resistance corresponds to the resistance of the entire coronary circulation. However, the resistance per outflow branch needed to be determined for an accurate flow distribution throughout the coronary circulation. One of the most widely used methods to do so, is based on the radius of the outflow branches (Mittal et al., 2005; Huo and Kassab, 2007; Murray, 1926; Van der Giessen et al., 2011). The total resistance can be divided as (Murray, 1926):

$$R_i = R_{tot} \frac{\sum_i r_i^b}{r_i^b}, \quad (5.5)$$

with r_i the radius of a single outflow branch, b the coefficient with which the radii were scaled and $\sum_i r_i^b$ the sum of all radii to the power b . The corresponding resistance of each vessel (R_i) was then prescribed at the outlet by means of lumped-parameter coronary model (see Figure 5.1). The individual resistances of the lumped-parameter coronary model as seen in Figure 5.1 were then calculated as follows (Sankaran et al., 2012):

$$R_a = 0.32R_i, \quad (5.6)$$

$$R_{a,micro} = 0.52R_i, \quad (5.7)$$

$$R_{v,micro} = 0.08R_i, \quad (5.8)$$

$$R_v = 0.08R_i. \quad (5.9)$$

The compliance C_a and C_{im} were as follows:

$$C_a = 0.11 \frac{\tau}{R_i}, \quad (5.10)$$

$$C_{im} = 0.89 \frac{\tau}{R_i}, \quad (5.11)$$

where τ is the RC-time constant of the lumped-parameter model whereas R_i is the resistance of the lumped-parameter model per branch. The compliances C_a and C_{im} represent the compliance of the arterial and intra-myocardial system, respectively. For constant inflow boundary conditions, the impedance of the lumped-parameter model will only depend on the resistance of the model once blood pressure has reached its steady state. Hence for this study, we chose a τ of 0.1 s to ensure a quick transition from simulation to simulation when using different parameter sets such that computational costs were reduced.

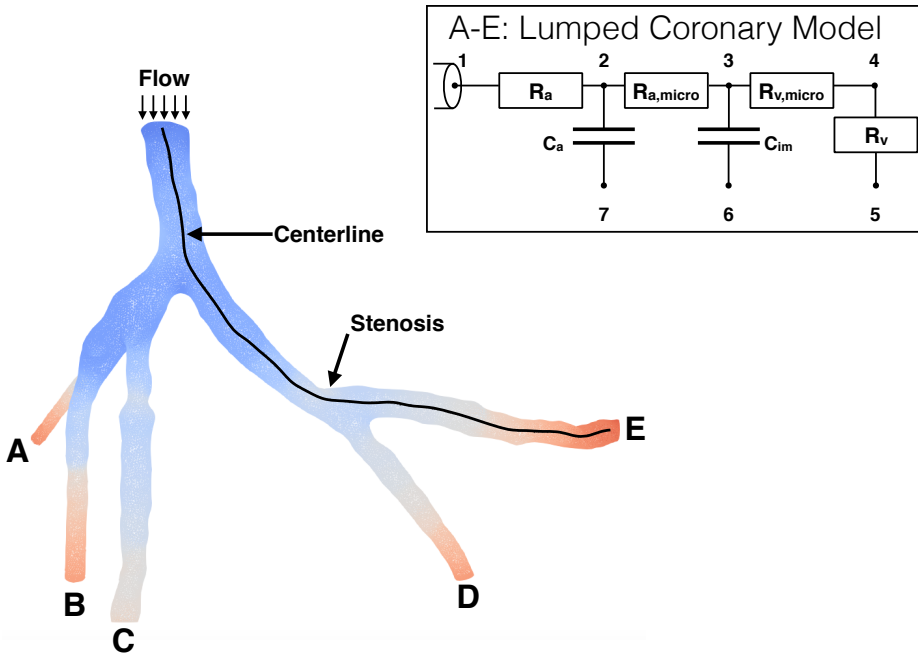


Figure 5.1: The boundary conditions at the inlet and outlets as well as the coronary circulation are shown. Furthermore, the stenosis and centerline for the geometry are depicted.

5.2.6 Numerical implementation

Boundary conditions were calculated for each parameter set. Based on these boundary conditions, simulations were performed. In order to reduce simulation time, simulations were performed in a consecutive order such that when moving to the next parameter set, simulations did not need to be started from a state with no flow. To this end the parameter set was ordered from lowest to highest coronary flow. Simulations were started with the lowest flow and carried out until the solutions for the highest flow were obtained. Simulations for each parameter set lasted until the maximum change in pressure between the current to the previous time step ($\epsilon_p = \frac{p_i^t - p_i^{t-\Delta t}}{\Delta t}$) at the inlet and the outlets was less than 1 mmHg/s. Once a simulation was considered converged, the next simulation was carried out with the next parameter set. This was done until all sets of simulations were performed.

5.2.7 Uncertainty analysis & sensitivity analysis

Changes in parameters that determine the boundary conditions: perfusion, left ventricular mass, flow distribution and mean arterial pressure will influence the FFR. Using uncertainty quantification (UQ) and sensitivity analysis (SA) the influence of those four parameters on the computed FFR was investigated. The SA was based on a global variance-based method which gives the importance of each input parameter on the total uncertainty in

the FFR (Huberts et al., 2014; Donders et al., 2015). Using SA, parameters can be sorted from least to most important such important parameters should either be measured or estimated more accurately. Using the SA analysis, the Sobol indices for all four parameters are computed per patient. These indices are a measure of the relative importance with respect to the uncertainty in FFR. In order to do so, the agPCE method was used which builds a polynomial meta-model of only significant terms (Quicken et al., 2016). The main benefit of the agPCE method is the fact that the computationally expensive CFD model needs to be evaluated significantly less compared to other methods (Quicken et al., 2016). For more detail we refer the reader to the work of Quicken *et al.* (Quicken et al., 2016).

5.2.7.1 Population based

Parameter ranges used for this study are shown in Table 5.1. The range of the perfusion was based on the work of Danad *et al.* and Choy *et al.* (Danad et al., 2014; Choy and Kassab, 2008) and was found to be between 0.73 and 1.23 mL/gram/min, respectively. The range of the left ventricular mass was obtained for men and women seperately. For men the left ventricular mass was shown to range between 75 and 220 gram whereas for women this was between 60 and 190 gram (Kumaran et al., 2002). Next, the range of Murray's exponent for dividing the total coronary resistance among each branch needed to be estimated. In literature various values of b can be found ranging between approximately 2 and 3 (Mittal et al., 2005; Huo and Kassab, 2007; Murray, 1926; Van der Giessen et al., 2011) but also shown to be dependent on the type of vessel (Huo and Kassab, 2007). The mean arterial pressure in this study ranged between 70 mmHg and 120 mmHg (Engelen et al., 2012). In total 50 parameter sets were created for which the CFD model was evaluated for. Per patient, the quality of the meta-models for the SA was checked and if needed new simulations could be performed. For all parameter ranges we assumed a uniform distribution such that the likelihood of occurance was the same.

Table 5.1: Parameters used in this study with their corresponding minimum and maximum value. [1](Choy and Kassab, 2008); [2](Danad et al., 2014); [3](Kumaran et al., 2002); [4](Mittal et al., 2005);[5] (Huo and Kassab, 2007); [6] (Murray, 1926); [7] (Van der Giessen et al., 2011); [8] (Engelen et al., 2012)

Parameter	Symbol	Unit	Min.	Max.	Reference
Perfusion	q_{per}	mL/gram/min	0.73	1.23	[1,2]
Left ventr. mass (M)	m_{lv}	gram	75	220	[3]
Left ventr. mass (F)	m_{lv}	gram	60	190	[3]
Murray's constant	b	-	2	3	[4,5,6,7]
Mean arterial pressure	\bar{p}_a	mmHg	70	120	[8]

5.2.7.2 Measurement based

For the measurement-based approach we investigated the uncertainty in computed FFR in case of an known left ventricular mass (m_{lv}) from CTA and its corresponding uncertainty. The uncertainty in the m_{lv} was assumed to be around $\pm 5\%$. In literature most of the uncertainty in the m_{lv} is given based on minimal distances and not volume. As the exact uncertainty in left ventricular mass was unknown, a 5% uncertainty was assumed. All other parameters were kept the same as shown in Table 5.2. For this purpose simulations were again evaluated, however this time with new values for the left ventricular mass.

Table 5.2: Parameters used in this study with their corresponding minimum and maximum value. [1](Choy and Kassab, 2008); [2](Danad et al., 2014); [3](Mittal et al., 2005);[4] (Huo and Kassab, 2007); [5] (Murray, 1926); [6] (Van der Giessen et al., 2011); [7] (Engelen et al., 2012)

Parameter	Symbol	Unit	Min.	Max.	Reference
Perfusion	q_{per}	mL/gram/min	0.73	1.23	[1,2]
Uncertainty left ventr. mass	dm_{lv}	%	-5	+5	-
Murray's constant	b	-	2	3	[3,4,5,6]
Mean arterial pressure	\bar{p}_a	mmHg	70	120	[7]

5.2.8 Post-processing

For post-processing, the centerline of the vessel containing the stenosis was extracted (see Figure 5.1) using the open-source library Vascular Modeling ToolKit (VMTK) (Antiga et al., 2008). Next, the proximal (p_a) and distal (p_d) pressure were obtained by taking the average pressure over a plane perpendicular to the centerline. The proximal pressure (p_a) was obtained a couple of radii from the inlet which *in vivo* would be close to the ostium. The distal pressure (p_d) was obtained at the stenosis location as indicated by the physician. The FFR was then calculated per case using:

$$FFR = \frac{p_d}{p_a}. \quad (5.12)$$

5.3 Simulations & analysis

In this study a total of 14 patients were included. Mean left ventricular mass for all patients was 144 grams ranging between a minimum of 107 and maximum of 223 grams. The ranges were similar to what was found in literature (Kumaran et al., 2002). The measured FFR was found to be between 0.75 and 0.98 with a mean of 0.86.

5.3.1 Simulations

50 simulations per patient were performed using population-based ranges whereas another 50 simulations per patient were performed for measured left ventricular mass. In total 1400 simulations were performed. The differences between the measured and computed FFR are found to be similar to what can be found in literature (Kim et al., 2014; Nørgaard et al., 2014; Fossan et al., 2018; Koo et al., 2011; Nakazato et al., 2013; Itu et al., 2016) (see Figure 5.2c,5.2d). In general the ranges in computed FFR are found to vary significantly from patient to patient. FFR ranges are between 0.078 and 0.66 (see Figure 5.2a).

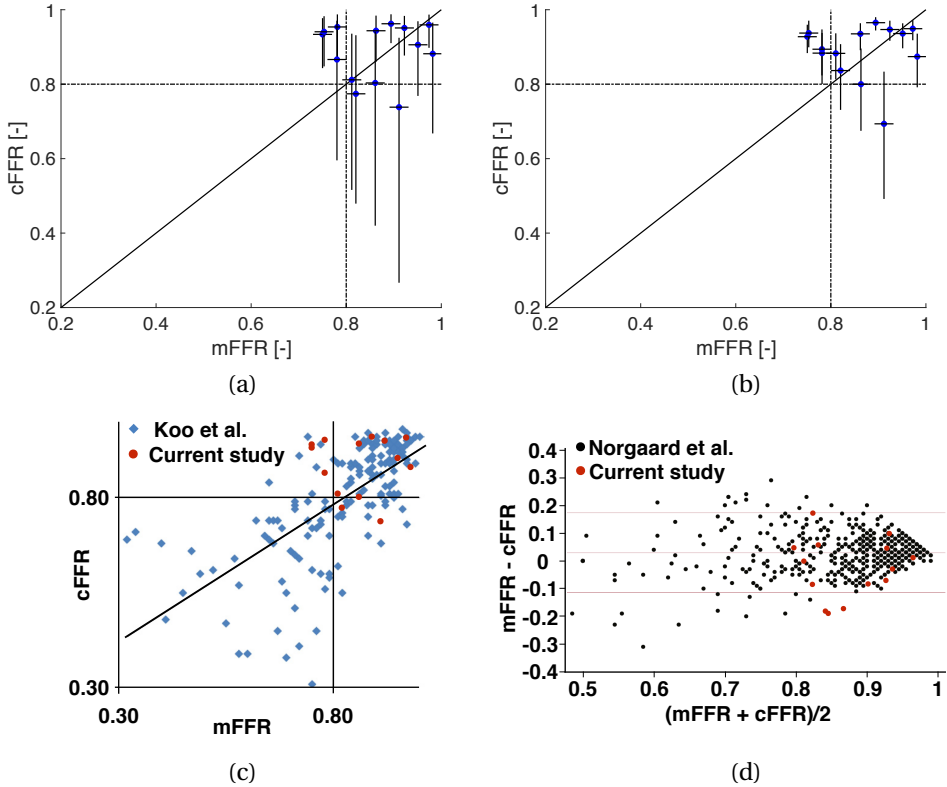


Figure 5.2: Uncertainty for the measured (mFFR) and computed FFR (cFFR) can be seen in (a) and (b). The dashed lines represent the FFR threshold of 0.80 whereas the solid diagonal line represents the identity line. In (a) the FFR uncertainty for the 14 patients is shown when using population-based variance. In (b) the FFR uncertainty when including a patient's left ventricular mass with $\pm 5\%$ uncertainty is depicted. In (c) the FFR predictions of the current study (population ranges) are plotted on top of the results from Koo *et al.* (Koo *et al.*, 2011). Furthermore, in (d) the current results and the results from Norgaard *et al.* are depicted (Norgaard *et al.*, 2014).

When including the patient's left ventricular mass with an uncertainty range of 5%, FFR ranges decrease on average by a factor 2.2 with patient 11 showing a decrease of a factor 3.4. The FFR ranges when considering a smaller uncertainty in left ventricular mass are between 0.036 and 0.34 as can be seen in Figure 5.2b. Based on Figure 5.3a, it can be seen that the FFR uncertainty depends on left ventricular size. Patients with a lower m_{lv} have a larger ΔFFR whereas with increase in m_{lv} the ΔFFR decreases. It furthermore, can be observed that FFR uncertainty and median FFR have a strong correlation (see Figure 5.3b). With increasing median FFR, the uncertainty in FFR decreases linearly.

5.3.2 Sensitivity analysis

For the agPCE method, 50 CFD model evaluations per patient were more than sufficient. Meta-model quality for all models was high ($Q^2 > 0.99$). Quality of the meta-models was high enough with a maximum polynomial order of 3. Interaction between parameters

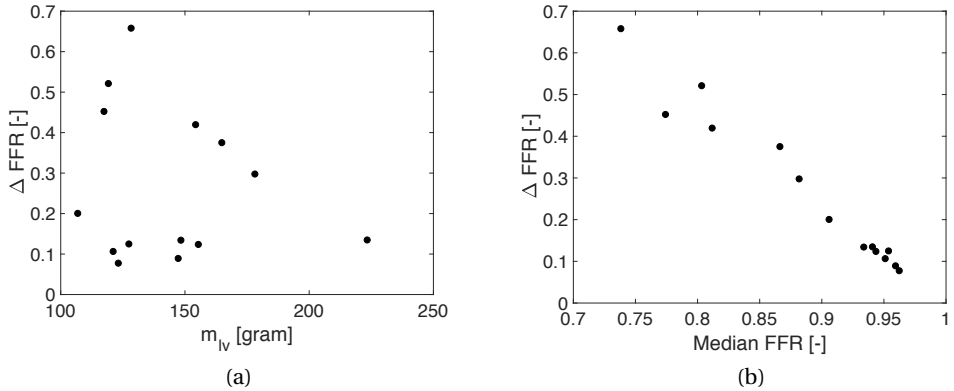


Figure 5.3: In (a) the FFR uncertainty as a function of the left ventricular mass is shown for population-based variance. The FFR uncertainty as a function of the median FFR is shown in (b).

was relatively small (approximately 6%). Most of the interaction was between perfusion and left ventricular mass. The parameter with the largest effect on the computed FFR was the left ventricular mass. On average, approximately 72% of the FFR uncertainty could be attributed to the m_{lV} . The uncertainty in the perfusion amounts for 19% of the FFR uncertainty as can be seen in Figure 5.4a. Murray's exponential constant has the smallest effect on the FFR (< 1%). The relative importance of the four variables in decreasing order of importance based on their impact on the computed FFR were left ventricular mass (72%), myocardial perfusion (19%), mean arterial pressure (8%) and Murray's constant (< 1%). In general the m_{lV} was approximately 3.8 and 9 times more important than myocardial perfusion and mean arterial pressure, respectively. Murray's constant had a total and main Sobol indices of approximately 1%, hence the parameter with the smallest effect on the FFR. The main Sobol indices per patient are shown in Figure 5.5. A thing to note is that the main Sobol indices for the four parameters do not show large variation from patient to patient (see Figure 5.5).

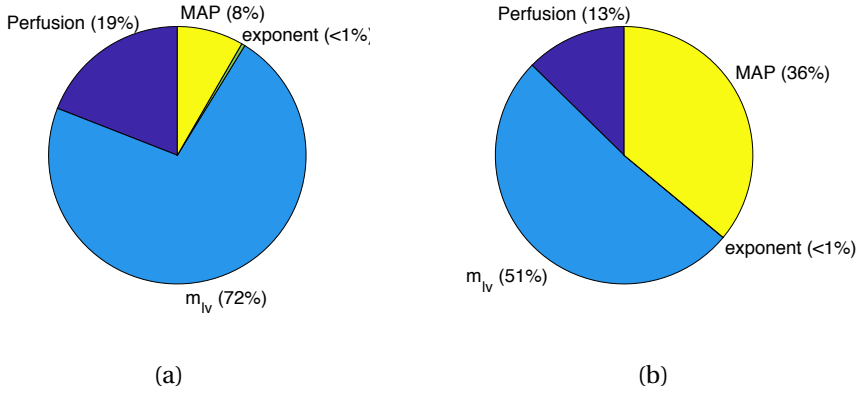


Figure 5.4: The relative influence of each of the four parameters on the uncertainty of the computed FFR is depicted.

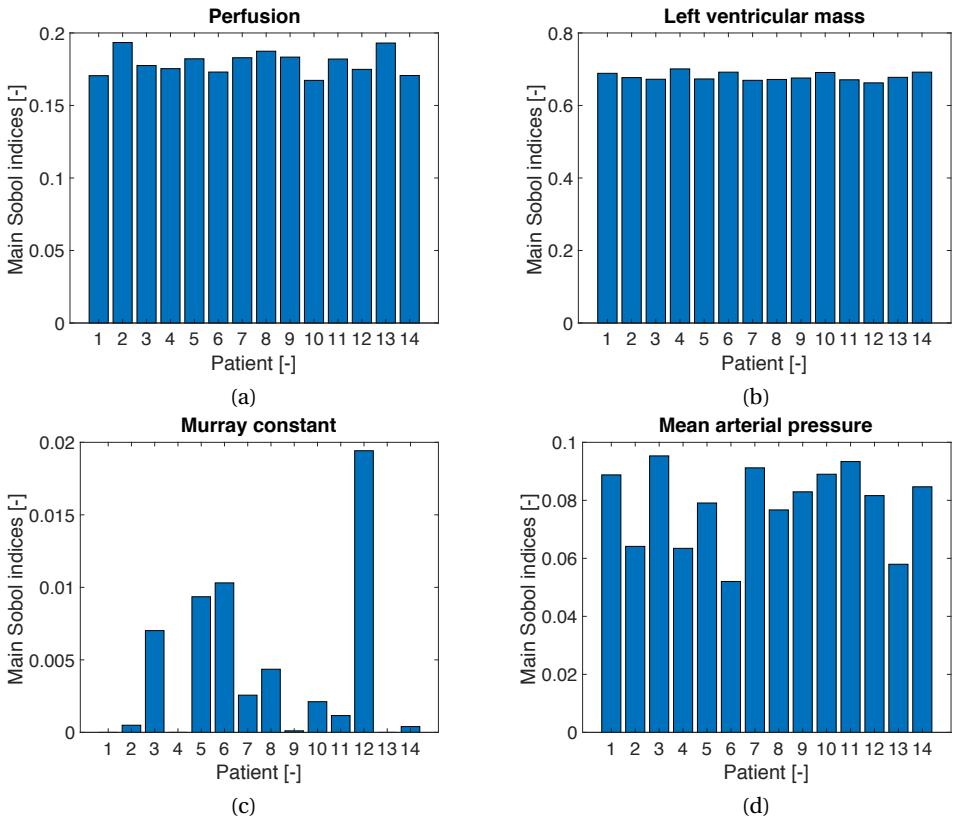


Figure 5.5: The main Sobol indices for 14 patients for the myocardial perfusion (a), left ventricular mass (b), Murray's constant (c) and mean arterial pressure (d)

Including measured left ventricular mass with uncertainty is shown to yield meta-models of the same quality ($Q^2 > 0.99$) and maximum polynomial order of 3. Interaction between parameters is shown to decrease from 6% to 1.5%. The left ventricular mass is shown to remain the parameter with the largest affect on the FFR uncertainty. It accounts for 51% of the total uncertainty (see Figure 5.4b). The effect of perfusion on the FFR uncertainty is shown to have decreased whereas the effect of the \bar{p}_a is shown to have increased from 8% to 36%.

5.4 Discussion

The aim of the study was to investigate the effect of uncertainty in myocardial perfusion, myocardial mass, Murray's constant and mean arterial pressure on the computed FFR. To this end we performed simulations on coronary circulations. The inflow boundary condition was based on myocardial mass and myocardial perfusion. Furthermore, flow division was based on Murray's law whereas mean arterial pressure was based on population based ranges. Using the uncertainty quantification and sensitivity analysis, the impact of each parameter on the FFR is estimated.

5.4.1 Simulations

Differences between the measured and computed FFR are found to be similar to what can be found in literature (Kim et al., 2014; Nørgaard et al., 2014; Fossan et al., 2018; Koo et al., 2011; Nakazato et al., 2013; Itu et al., 2016). For the population based values, we saw significant differences in ranges in computed FFR between patients. For patients with a lower m_{lv} , the FFR uncertainty was higher than for patients with a higher m_{lv} . This can be explained by the fact that smaller hearts in general have smaller coronaries such that blood flow will be lower compared to larger hearts. The form of the coronaries follows the function of the heart making sure sufficient blood flow is delivered. However, when prescribing flows based on larger left ventricles for smaller coronaries, the pressure drop will tend to be higher resulting in a lower FFR. On the other hand patients with a larger ventricle have a smaller range in FFR. This is due to the fact that for larger left ventricles the total range of available flows will be lower relative to the physiological flow such that pressure drops throughout the coronaries will be lower. As flow (q) and pressure drop (Δp) are non-linearly (Seeley and Young, 1976; Garcia et al., 2005; Itu et al., 2013; Huo et al., 2011) related by $\Delta p \propto q^2$. Small flow variation for lower flows will have a smaller effect on the pressure drop compared to the same flow variation at higher flows. When including measured left ventricular mass with a smaller uncertainty and thus reducing the uncertainty in coronary blood flow, the uncertainty in FFR decreases by a factor 2.2 on average.

5.4.2 Sensitivity analysis

We have shown that 50 model evaluations per patient were enough to create an accurate meta-model ($Q^2 > 0.99$). Up to third order polynomials were observed whereas interaction between parameters was rather small. In this study the largest uncertainty in FFR is due to the left ventricular mass (72%) and perfusion (19%) when using population-based ranges. The contribution of the mean arterial pressure (8%) was rather small whereas Murray's constant (< 1%) was found to be negligible. Fossan *et al.* found similar results where

mean arterial pressure and Murray's constant are significantly less important than the flow through the coronaries (Fossan *et al.*, 2018). Coronary flow has a larger effect on the computed FFR than mean arterial pressure due to the fact that flow is non-linearly ($\Delta p \propto q^2$) related to the pressure drop (Seeley and Young, 1976; Garcia *et al.*, 2005; Itu *et al.*, 2013; Huo *et al.*, 2011). The FFR which is a function of pressure drop (Δp) and mean arterial pressure (p_a) as shown here:

$$FFR = \frac{p_d}{p_a} = 1 - \frac{\Delta p}{p_a}, \quad (5.13)$$

will therefore be influenced more by a change in flow than by the same relative change in mean arterial pressure (p_a). Performing sensitivity analysis once including left ventricular mass has shown that left ventricular mass still is the parameter with the largest impact on the FFR. Approximately 51% of the FFR uncertainty can be attributed to m_{lv} . Moreover, the mean arterial pressure became more important (36%) whereas myocardial perfusion became less important (13%). Murray's constant still had a very small effect on the FFR uncertainty ($< 1\%$). The results suggest that when including m_{lv} measurements, accuracy should lie within a smaller uncertainty range than the currently used $\pm 5\%$. \bar{p}_a played a bigger role once measured m_{lv} was included. However, when \bar{p}_a was included with the same standard deviation as Fossan *et al.* in addition to the measured m_{lv} , we found that approximately 10% of the FFR uncertainty was due to \bar{p}_a .

5.4.3 Limitations

One of the main limitations of the study is the fact that FFR computations in his study are less accurate as hoped for. One of the reasons for this is the low number of patients included in this study. Moreover these patients are mostly located within the FFR range where most CFD models computing FFR are the least accurate (Cook *et al.*, 2017). Furthermore, although computed FFR uncertainty is shown to decrease when including patient's left ventricular mass, it does not necessarily improve the predictions with respect to the measured FFR.

A reason could be the fact that myocardial perfusion range in this study does not match the patient's perfusion. In this study the basal myocardial perfusion was based the work of Choy *et al.* and Danad *et al.* (Choy and Kassab, 2008; Danad *et al.*, 2014). However, the lowest myocardial perfusion at baseline as found by Danad *et al.* (Danad *et al.*, 2014) and Stuijzand *et al.* (Stuijzand *et al.*, 2015) was approximately 0.48 mL/gram/min which is 34% lower than used in this study. Furthermore, the highest value for myocardial perfusion was found to be close to 1.8 mL/gram/min which is 46% larger compared to the maximum value used in this study. This could explain the overestimation or underestimation of the FFR as for the model less or more blood was assumed to go to the myocardium.

Another reason for the mismatch between computed FFR and measured FFR could be due to the chosen coronary flow reserve (CFR) which was set to 3.3 for all vessels based on the work of Danad *et al.* (Danad *et al.*, 2014). However, in literature various values can be found for the CFR (Stuijzand *et al.*, 2015; Lee *et al.*, 2016; McGinn *et al.*, 1990). Studies also have found significant differences between CFRs for functionally significant and functionally non-significant stenoses (Danad *et al.*, 2014; Stuijzand *et al.*, 2015). Moreover, Danad *et al.* showed that for some patients the CFR was below 1, meaning that flow decreases during hyperemia (Danad *et al.*, 2014).

In order to determine the accuracy of model predictions, flow measurements could help

to get a better understanding of the underlying hemodynamics (Gould et al., 1988; Tona et al., 2006). Flow measurements could help to determine whether the computed blood flow corresponding to the FFR matches the *in vivo* situation. The computed FFR can match measured FFR while the computed and *in vivo* blood flow do not necessarily have to match. On the other hand, a different FFR can be computed while modelling the same blood flow as in the patient. Having a good indication of the patient's coronary blood flow would both help to get better boundary conditions and also benchmark the CFD models for FFR and flow. Flow indications based on available CT images could be achieved by using intensities of contrast agents to obtain coronary flow (Yao et al., 2013; Bae et al., 2018). Furthermore obtaining perfusion information (Di Carli et al., 2007) would help improve the boundary conditions per patient and thus getting the computed FFR closer to the measured FFR .

5.5 Conclusion

Largest part of the uncertainty in FFR can be attributed to the left myocardial mass (m_{lv}). Mean arterial pressure and Murray's constant were shown to have a very small effect on the FFR and therefore can be fixed to a population-based average. The uncertainty is shown to significantly decrease when including the patient's left ventricular mass (> 2x). Left ventricular mass should be measured more accurately than $\pm 5\%$ as half of the remaining FFR uncertainty was due to m_{lv} . When including m_{lv} , \bar{p}_a became the second most important parameter. However using a variation in \bar{p}_a as found in literature shows that \bar{p}_a only accounts for a small portion of the FFR uncertainty.

Conflict of Interest

None

5.6 Acknowledgment

The authors would like to thank the Dutch institute IMDI- ZonMw for funding [Project number: 104003009].

CHAPTER 6

General Discussion

6.1 General discussion

6.1.1 Introduction

For classifying functional significance of coronary stenoses, the fractional flow reserve (FFR) is considered to be the gold standard. The FFR has been shown to accurately classify stenoses based on their functional significance, although it still remains an invasive assessment as intravascular pressure measurements need to be performed proximal and distal to stenoses. To circumvent this drawback, computational fluid dynamics models for the coronary blood flow and pressure could be used to non-invasively assess the computed FFR whilst maintaining the benefits of FFR. Previously a lot of effort is put into improving CFD models for vFFR predictions (Taylor et al., 2013; Morris et al., 2015; Min et al., 2012). One of the drawbacks of the current models is that FFR uncertainty quantification due to uncertainty in parameter values is difficult to perform due to the computational costs involved in evaluating these complex CFD models. Therefore the goal of this study was twofold. The first goal was reducing computational time of models by investigating the feasibility of reduced order models. The second goal was to investigate the effect of parameter uncertainty on the computed FFR. Investigating the feasibility of reduced order models was done by comparing the computed FFR of reduced order models with the FFR of higher order models. Investigating the impact of parameter uncertainty was achieved by using a global uncertainty quantification (UQ) and sensitivity analysis (SA).

To investigate the effect of choices in blood viscosity models on the computed FFR, various different viscosity models were used for modelling coronary blood flow in **Chapter 2**. For these blood viscosity models both Newtonian and non-Newtonian models were used. In **Chapter 3** the effect of population-based variance of blood viscosity on the computed FFR was investigated by means of uncertainty quantification (UQ) and sensitivity analysis (SA). Using UQ and SA the importance and the contribution of each parameter on the computed FFR can be quantified. Later on, in **Chapter 4** the influence of model-order reduction on the computed FFR was investigated using parameterized coronary geometries. Finally in **Chapter 5** the influence of uncertainty in boundary conditions on the computed FFR due to for example left ventricular mass and myocardial perfusion is investigated. Below the benefits and limitations of the previous chapters will be discussed.

6.1.2 Impact of blood viscosity

Blood is known to be a complex non-Newtonian fluid for which the viscosity depends on the shear rate. For higher shear rates blood viscosity is shown to decrease whereas for lower shear rates blood viscosity is known to increase. This change in viscosity due to shear thinning properties of blood. When performing FFR simulations using computational fluid dynamics models, blood viscosity needs to be included. This can be done in either a Newtonian way where viscosity is fixed to a single value and does not depend on the shear rate or in a non-Newtonian way allowing the viscosity to change as a function of the shear rate. Newtonian approximations are based on single values (Kim et al., 2010; Valen-Sendstad et al., 2013; Vignon-Clementel et al., 2010; Mirramezani et al., 2019; Steele et al., 2007) or patient's input such as hematocrit and plasma viscosity (Sankaran et al., 2016; Fossan et al., 2018). The main benefit of these models is the fact that no shear rates need to be computed. However, implicitly the magnitude of the shear rate is assumed by fixing the viscosity to a certain value. The choice of blood viscosity model and model pa-

parameters will influence blood flow and pressure through the coronaries and thus ultimately impact the computed FFR. Different viscosity models or different viscosity parameters will therefore most likely yield a different prediction and in the worst case scenario will result in ambivalent stenosis classifications. In literature no real consensus can be found regarding the choice of a viscosity model or the values of the viscosity (Sankaran et al., 2016; Fossan et al., 2018; Kim et al., 2010; Johnston et al., 2004; Vignon-Clementel et al., 2010; Mirramezani et al., 2019). In a study by Johnston et al, differences in wall shear stresses depended on the viscosity model (Johnston et al., 2004). Although only one set of model parameters is used per model in the latter study, differences can be expected to increase for different choices in model parameters.

Hence the goal of **Chapter 2** was to investigate how different blood viscosity models would affect the computed FFR within a single patient. For this purpose, blood flow and blood pressure for 146 patients (206 lesions) were computed. For each patient, simulations were performed using blood viscosity based on a high and low fixed constant value (Kim et al., 2010; Valen-Sendstad et al., 2013; Vignon-Clementel et al., 2010; Mirramezani et al., 2019; Steele et al., 2007). Moreover, we also used a Newtonian and non-Newtonian model based on hematocrit and plasma viscosity. As only patient-specific hematocrit was available, these models were evaluated for high and low plasma viscosity to cover the population range (Baskurt and Meiselman, 2003; Haidekker et al., 2002; Késmárky et al., 2008; Rand et al., 1964). This way, three blood viscosity models with corresponding lower and higher viscosities were evaluated resulting in six different viscosity approaches. In this study each patient was evaluated six times resulting in a total of 876 simulations. We found that depending on the choice of the blood viscosity, 78 to 96 lesions were deemed significant (FFR=0.80 as cut-off value). For 7% of the lesions no clear stenosis classification could be made. In other words, depending on the choice of the blood viscosity, a stenosis might be classified differently. Moreover, we found that the computed FFR could vary up to 0.065 and, in 53% of the lesions, are higher than the measured clinical reproducibility found by Berry *et al.* and Gaur *et al.* (Berry et al., 2013; Gaur et al., 2014b). This FFR variance was found to be largest for FFR values between 0.6 and 0.8, similar to what was found in a review study by Cook *et al.* (2017). In the review study, the studies of Koo *et al.*, Nakazato *et al.*, Kim *et al.*, Renker *et al.* and Nørgaard *et al.* which compared computed FFR with actual measured FFR were analyzed (Koo et al., 2011; Nakazato et al., 2013; Kim et al., 2014; Renker et al., 2014; Nørgaard et al., 2014). Although FFR computations in these studies were shown to be accurate (82%) FFR computations were less accurate for FFR values between 0.7 and 0.8. The accuracy in this range for the five studies was found to be approximately 46%. In order to decrease the number of ambivalent stenoses in this region, FFR models need to become more accurate in this region which could be done using patient-specific viscosities. For the lower (<0.6) and higher (>0.9) FFR values, the FFR models were shown to yield accuracies above 86%. Especially for FFR values between 0.7 and 0.8, viscosity models and their corresponding parameters should be chosen more carefully in order to reduce the inaccuracy of the computed FFR.

In **Chapter 2** we used the Quemada model to capture the non-Newtonian behaviour of the blood viscosity. Based on literature, the Quemada model was found to accurately capture the blood behaviour (Marcinkowska-Gapińska et al., 2007). Hence in **Chapter 3**, the goal was to see what the effect of uncertainty in hematocrit (H_{ct}) and plasma viscosity (η_p) is on the computed FFR. For this purpose we used the blood viscosity uncertainty by using the Quemada model. Population-based variances for H_{ct} and η_p were used to compute the FFR for different combinations of both parameters. Using uncertainty quantification,

the uncertainty in FFR was investigated, whereas with sensitivity analysis the relative importance of each parameter was investigated. When looking at individual lesions we found that for 15 lesions, the computed FFR range was intersecting the FFR threshold of 0.80. In other words, depending on the choice of H_{ct} and η_p , the classification of approximately 1 out of 5 lesions depends on the chosen values for the parameters. Including measured H_{ct} in the FFR model was shown to decrease the FFR uncertainty on average by a factor of 2.2 such that only 7.5% of the lesions would receive an ambivalent classification. Without measured H_{ct} and η_p , the FFR uncertainty was found to be as large as 0.08. Similar to **Chapter 2** and the studies of Koo *et al.*, Nakazato *et al.*, Kim *et al.*, Renker *et al.* and Nørgaard *et al.*, the largest uncertainty was for FFR values between 0.7 and 0.8 (Koo *et al.*, 2011; Nakazato *et al.*, 2013; Kim *et al.*, 2014; Renker *et al.*, 2014; Nørgaard *et al.*, 2014). With no measured H_{ct} , up to 88% of the lesions had a FFR uncertainty higher than the measured clinical reproducibility found by Berry *et al.* and Gaur *et al.* (Berry *et al.*, 2013; Gaur *et al.*, 2014b). The FFR uncertainty ranges in this study can be expected to be larger than the ones found by Sankaran *et al.* and Fossan *et al.* (Sankaran *et al.*, 2016; Fossan *et al.*, 2018). The reason for this is that both studies used a fixed value of the plasma viscosity whereas in the current study we varied the plasma viscosity within the population-based range.

6.1.3 Blood viscosity (limitations)

One of the limitations of the studies on viscosity models was the fact that only uncertainty in H_{ct} and η_p was taken into account. This was done while assuming that the uncertainty in other parameters such as boundary conditions and geometry were negligible. Even for the best case scenario where all other parameters are known except for blood viscosity, FFR uncertainty was large with FFR ranges up to 0.08. In future studies, uncertainty quantification and sensitivity analysis should be performed on a larger number of parameters as done by Sankaran *et al.* where the uncertainty of myocardial resistance, stenosis length, minimum lumen diameter and blood viscosity was taken into account (Sankaran *et al.*, 2016). However, with more parameters the number of model evaluations per patient goes up extremely (Quicken *et al.*, 2016). If the analysis needs to be performed for a larger number of patients thus results in an unfeasible study because of the enormous computational effort. Therefore one has to rely on reduced order models when performing sensitivity analysis (Fossan *et al.*, 2018; Morris *et al.*, 2017).

6.1.4 Model order reduction

One of the main drawbacks of computational fluid dynamics (CFD) models for coronary blood flow is the computational time. The CFD models require a lot of computational effort such that uncertainty quantification and sensitivity analysis can become unfeasible. The reason for this is the fact that these models tend to be three dimensional (3D) in order to be as close as possible to the *in vivo* situation. As Morris *et al.* already pointed out, simulation time of a 3D transient approach can range somewhere between hours and days (Morris *et al.*, 2017). Using a steady approach can significantly reduce computational time (Tu *et al.*, 2014). However, the main benefit of these models is the high temporal and spatial resolution which can be achieved within an *in vivo* geometry.

Using a 2D axisymmetric approach, the high temporal and spatial resolution is mostly maintained while slightly simplifying the geometry (Morris *et al.*, 2016). A 3D representation of a coronary artery with curvature and torsion becomes a slice of a straightened tube.

This way only a fraction of the coronary domain needs to be solved and computational time is tremendously reduced. In **Chapter 2**, effects of model order reduction were investigated using a parameterized approach, by replacing the 3D CFD model with its corresponding 2D axisymmetric counterpart while keeping all boundary conditions the same. For this approach, 200 coronary geometries with a single stenosis were generated in 3D based on seven geometrical characteristics. Four of the characteristics were related to the stenosis itself namely stenosis severity, asymmetry, length and angular position. Curvature, torsion and tapering were parameters related to the coronary artery itself. Based on these 3D geometries the corresponding 2D axisymmetric geometries were generated. We furthermore investigated the impact of using a constant flow instead of a transient flow as a way of reducing computational cost. We found that when using transient inflows for both 3D and 2D models, FFR predictions were nearly identical. The 3D model with transient inflow was considered the reference model. For the reference model we found that higher velocities were found at the outer side of the bend with increase in curvature (Chang and Tarbell, 1988; Hayashi and Yamaguchi, 2002; Kelidis and Konstantinidis, 2018). Moreover, recirculation zones right after the stenosis were found to behave similar to what is found in literature (Kelidis and Konstantinidis, 2018; Katritsis et al., 2010). We furthermore found that using constant inflow boundary conditions for 3D and 2D models did not necessarily result in accurate FFR computations compared to the reference model. Only when the constant inflow was based on the root mean square of the transient flow curve did the models yield nearly similar FFR predictions. Furthermore, computational time was reduced from approximately 100 CPU hours for the 3D transient model to approximately 28 minutes for the 2D transient model. The largest reduction in computational time is achieved when replacing the 3D transient model (reference) with the 2D steady model. Using a 2D steady model resulted on average in a computational time of 2 seconds. In addition, not only did the 2D axisymmetric approach result in faster model evaluations but also yielded results very close to the transient case for a constant inflow based on the root mean square (RMS) of its corresponding transient flow curve. Discrepancies between the reference model and the 2D RMS model were mostly caused due to curvature of the vessel, stenosis severity, stenosis length and, tapering of the vessel. Vessel characteristics in 3D which were left out in the 2D case such as torsion, angular position of the stenosis and, the stenosis asymmetry had an insignificant role.

6.1.5 Model order reduction (Limitation)

The model order reduction study conducted in **Chapter 4** was based on a parameterized approach. The benefit of this approach is the fact that an extensive analysis of the impact of model order reduction on the FFR can be done without the need of patient-specific data. The relative contribution of each parameter with respect to reducing the model order can be obtained. However the impact of reducing model complexity using patient-specific geometries is still unknown and needs to be investigated in future studies. Another limitation of this study is the usage of geometries with a single focal stenosis per vessel whereas in vivo stenoses are not always focal. Furthermore, the number of stenoses per vessel is not always limited to one such that the effect of model order reduction for multiple stenoses per vessel should be investigated as well.

6.1.6 Myocardial mass and perfusion

In order to perform patient-specific coronary simulations of blood flow and pressure, accurate boundary conditions are a necessity. The flow in the coronaries is based on the size of the myocardium (Kassab, 2006; Choy and Kassab, 2008) and also on the perfusion (Sharma et al., 2012). Moreover, the mean arterial pressure is needed for an accurate representation of the coronary blood pressure. The mean arterial pressure in combination with coronary blood flow determines the myocardial resistance. This myocardial resistance then needs to be divided among the braches.

In **Chapter 5** we investigated the effect of parameter uncertainty in boundary conditions for the computed FFR. To this end, left ventricular mass, myocardial perfusion, mean arterial pressure and Murray's constant were varied within their corresponding population-based ranges.

We found a similar difference between the computed FFR and the measured FFR as found in literature (Kim et al., 2014; Nørsgaard et al., 2014; Fossan et al., 2018; Koo et al., 2011; Nakazato et al., 2013; Itu et al., 2016). When looking at the uncertainty of the computed FFR for population-based variance in the boundary condition parameters, we found the FFR uncertainty to range up to 0.66. These FFR uncertainty ranges were found to be similar to the ones found by Fossan *et al.* (Fossan et al., 2018). Including the patients' left ventricular mass with a 5% uncertainty was shown to decrease the FFR range on average by a factor 2.2 with the maximum range being 0.34.

From the sensitivity analysis it becomes clear that 72% of the uncertainty in the FFR for population-based values is due to the uncertainty in left ventricular mass. Perfusion (19%) and mean arterial pressure (8%) are found have a smaller effect on the FFR whereas Murray's constant was found to have a negligible effect. When including patients' left ventricular mass with 5% uncertainty, left ventricular mass was still found to have the largest impact on FFR (51%). This strongly suggests that the uncertainty in left ventricular mass needs to be reduced to less than 5%. Also mean arterial pressure was found to play a larger role (36%). However this can be explained by the large range used in this study for the variation in mean arterial pressure (50 mmHg). Once we included mean arterial pressure with the same uncertainty as Fossan *et al.* we found that only 10% of the FFR uncertainty could be attributed to the mean arterial pressure. One of the main conclusions of this study is that patient-specific left ventricular mass should be included with small uncertainty.

6.1.7 Myocardial mass and perfusion (Limitation)

Unfortunately the exact uncertainty in left ventricular mass was unknown. This lead to an approximation of the reduced uncertainty in FFR due to patient-specific left ventricular mass. However, the main conclusion still remains that the left ventricular mass is the parameter with the largest impact on the FFR. Furthermore, for an accurate FFR estimation left ventricular mass should be with a smaller uncertainty than the assumed $\pm 5\%$ uncertainty. A limitation of this study is that we only focussed on measured patient-specific boundary condition parameters and did not look at uncertainty in geometry and blood viscosity. As already shown by Sankaran *et al.* and Fossan *et al.* and in **Chapter 2** and **Chapter 3** it was shown that the choice of blood viscosity also has a relative large effect on the FFR (Fossan et al., 2018; Sankaran et al., 2016). In future studies, uncertainty in both parameter sets and in the geometry should all be included to put the impact of each parameter on the FFR into perspective.

6.1.8 Recommendations for future research

The work presented in this thesis could be extended in a number of ways. Focussing on the blood viscosity, we have shown in **Chapter 2** that computed FFR depends on the choice of blood viscosity model and parameter values. In **Chapter 3** we furthermore showed that if blood viscosity is chosen to be dependent on hematocrit and plasma viscosity, most of the uncertainty is due to hematocrit. In future studies, the diagnostic accuracy of FFR models due to various viscosity models should be investigated. Although we found relatively large differences in FFR between various viscosity models, it should be investigated how this translates into the diagnostic accuracy for each viscosity model. Moreover it should be investigated if diagnostic accuracy improves when including patient's hematocrit. Furthermore, the effect on the computed FFR should be investigated to see whether differences in computations and measurements decrease.

In order to reduce computational time, in **Chapter 4** we investigated the effect of model-order reduction on the computed FFR based on a parameterized approach. We found small differences in FFR between the 2D and 3D model when using appropriate inflow boundary conditions. Although results were promising, comparing 2D and 3D patient-specific models should give further insights on the feasibility of model-order reduction for the patient-specific case. Due to the low computational costs, the 2D model could be used to compute FFRs in a faster and computationally less expensive way making uncertainty quantification (UQ) and sensitivity analysis (SA) more feasible. This 2D model can also be applied for cases only 2D images are acquired such as when performing angiograms.

Based on UQ&SA we investigated the effect of left ventricular mass, myocardial perfusion, mean arterial pressure and, Murray's constant on the computed FFR. We found that left ventricular mass is the most important parameter. Including patient-specific left ventricular mass with smaller uncertainty did decrease the FFR uncertainty but not necessarily improve the computed FFR. In order to improve FFR computations, information of the coronary blood flow should be included. Incorporating additional flow information into the boundary conditions by means of perfusion imaging of the myocardium would help to get a better picture of boundary conditions needed for the myocardium. Moreover, future studies should be aimed at including measured or well-estimated coronary blood flow for the current CFD models aimed at computing FFR. As of now, most CFD models for computing FFR are solely benchmarked against measured FFR. However, as FFR is a relative measure, even if FFR is predicted correctly it does not imply that pressure and flow are correctly computed. Additional flow information would lead to an extra constraint making sure that not just the FFR but also the flow corresponds to the patient's *in vivo* situation. This would help to match the computed blood flow to the patient's *in vivo* blood flow. Furthermore, including parameter uncertainty is essential for computing FFR in order to obtain reliable FFR predictions.

Bibliography

- Alnæs, M., Blechta, J., Hake, J., Johansson, A., Kehlet, B., Logg, A., Richardson, C., Ring, J., Rognes, M. E., and Wells, G. N. (2015). The fenics project version 1.5. *Archive of Numerical Software*, 3(100):9–23.
- Antiga, L., Piccinelli, M., Botti, L., Ene-Iordache, B., Remuzzi, A., and Steinman, D. A. (2008). An image-based modeling framework for patient-specific computational hemodynamics. *Medical & biological engineering & computing*, 46(11):1097.
- Arima, M., Kanoh, T., Suzuki, T., Kuremoto, K., Tanimoto, K., Oigawa, T., and Matsuda, S. (2005). Serial angiographic follow-up beyond 10 years after coronary artery bypass grafting. *Circulation Journal*, 69(8):896–902.
- Bae, Y. G., Hwang, S. T., Han, H., Kim, S. M., Kim, H.-Y., Park, I., Lee, J. M., Moon, Y.-J., and Choi, J.-H. (2018). Non-invasive coronary physiology based on computational analysis of intracoronary transluminal attenuation gradient. *Scientific reports*, 8(1):4692.
- Baskurt, O. K. and Meiselman, H. J. (2003). Blood rheology and hemodynamics. In *Seminars in thrombosis and hemostasis*, volume 29, pages 435–450. Copyright© 2003 by Thieme Medical Publishers, Inc., 333 Seventh Avenue, New York, NY 10001, USA. Tel.:+ 1 (212) 584-4662.
- Bech, G. J. W., De Bruyne, B., Pijls, N. H., de Muinck, E. D., Hoorntje, J. C., Escaned, J., Stella, P. R., Boersma, E., Bartunek, J., Koolen, J. J., et al. (2001). Fractional flow reserve to determine the appropriateness of angioplasty in moderate coronary stenosis: A randomized trial. *Circulation: Journal of the American Heart Association*, 103(24):2928–2934.
- Berry, C., Van'T Veer, M., Witt, N., Kala, P., Bocek, O., Pyxaras, S. A., McClure, J. D., Fearon, W. F., Barbato, E., Tonino, P. A., et al. (2013). Verify (verification of instantaneous wave-free ratio and fractional flow reserve for the assessment of coronary artery stenosis severity in everyday practice): a multicenter study in consecutive patients. *Journal of the American College of Cardiology*, 61(13):1421–1427.
- Bessemers, D. (2007). On the propagation of pressure and flow waves through the patient specific arterial system.
- Blatman, G. and Sudret, B. (2010). An adaptive algorithm to build up sparse polynomial chaos expansions for stochastic finite element analysis. *Probabilistic Engineering Mechanics*, 25(2):183–197.

- Boron, W. F. and Boulpaep, E. L. (2012). *Medical Physiology, 2e Updated Edition E-Book: with STUDENT CONSULT Online Access*. Elsevier Health Sciences.
- Chang, L.-J. and Tarbell, J. (1988). A numerical study of flow in curved tubes simulating coronary arteries. *Journal of Biomechanics*, 21(11):927–937.
- Chen, J., Lu, X.-Y., and Wang, W. (2006). Non-newtonian effects of blood flow on hemodynamics in distal vascular graft anastomoses. *Journal of Biomechanics*, 39(11):1983–1995.
- Chen, P., Quarteroni, A., and Rozza, G. (2013). Simulation-based uncertainty quantification of human arterial network hemodynamics. *International journal for numerical methods in biomedical engineering*, 29(6):698–721.
- Chen, S. J. and Carroll, J. D. (2000). 3-d reconstruction of coronary arterial tree to optimize angiographic visualization. *IEEE transactions on medical imaging*, 19(4):318–336.
- Cho, Y. I. and Kensey, K. R. (1991). Effects of the non-newtonian viscosity of blood on flows in a diseased arterial vessel. part 1: Steady flows. *Biorheology*, 28(3-4):241–262.
- Choy, J. S. and Kassab, G. S. (2008). Scaling of myocardial mass to flow and morphometry of coronary arteries. *Journal of Applied Physiology*, 104(5):1281–1286.
- Çimen, S., Gooya, A., Grass, M., and Frangi, A. F. (2016). Reconstruction of coronary arteries from x-ray angiography: A review. *Medical image analysis*, 32:46–68.
- Cokelet, G. (1987). The rheology and tube flow of blood. *Handbook of bioengineering*, 14.
- Cook, C. M., Petraco, R., Shun-Shin, M. J., Ahmad, Y., Nijjer, S., Al-Lamee, R., Kikuta, Y., Shiono, Y., Mayet, J., Francis, D. P., et al. (2017). Diagnostic accuracy of computed tomography–derived fractional flow reserve: a systematic review. *JAMA cardiology*, 2(7):803–810.
- Curzen, N., Rana, O., Nicholas, Z., Golledge, P., Zaman, A., Oldroyd, K., Hanratty, C., Banning, A., Wheatcroft, S., Hobson, A., et al. (2014). Does routine pressure wire assessment influence management strategy at coronary angiography for diagnosis of chest pain?: the ripcord study. *Circulation: Cardiovascular Interventions*, pages CIRCINTERVENTIONS–113.
- Danad, I., Raijmakers, P. G., Harms, H. J., Heymans, M. W., van Royen, N., Lubberink, M., Boellaard, R., van Rossum, A. C., Lammertsma, A. A., and Knaapen, P. (2014). Impact of anatomical and functional severity of coronary atherosclerotic plaques on the transmural perfusion gradient: a [15o] h2o pet study. *European heart journal*, 35(31):2094–2105.
- De Bruyne, B., Fearon, W. F., Pijls, N. H., Barbato, E., Tonino, P., Piroth, Z., Jagic, N., Mobius-Winckler, S., Rioufol, G., Witt, N., et al. (2014). Fractional flow reserve–guided pci for stable coronary artery disease. *New England Journal of Medicine*, 371(13):1208–1217.
- De Bruyne, B., Pijls, N. H., Kalesan, B., Barbato, E., Tonino, P. A., Piroth, Z., Jagic, N., Möbius-Winkler, S., Rioufol, G., Witt, N., et al. (2012). Fractional flow reserve–guided pci versus medical therapy in stable coronary disease. *New England Journal of Medicine*, 367(11):991–1001.

- Dehmer, G. J., Weaver, D., Roe, M. T., Milford-Beland, S., Fitzgerald, S., Hermann, A., Messenger, J., Moussa, I., Garratt, K., Rumsfeld, J., et al. (2012). A contemporary view of diagnostic cardiac catheterization and percutaneous coronary intervention in the united states: a report from the cathpci registry of the national cardiovascular data registry, 2010 through june 2011. *Journal of the American College of Cardiology*, 60(20):2017–2031.
- Di Carli, M. F., Dorbala, S., Meserve, J., El Fakhri, G., Sitek, A., and Moore, S. C. (2007). Clinical myocardial perfusion pet/ct. *Journal of Nuclear Medicine*, 48(5):783–793.
- Donders, W., Huberts, W., van de Vosse, F., and Delhaas, T. (2015). Personalization of models with many model parameters: an efficient sensitivity analysis approach. *International journal for numerical methods in biomedical engineering*, 31(10).
- Douglas, P. S., De Bruyne, B., Pontone, G., Patel, M. R., Norgaard, B. L., Byrne, R. A., Curzen, N., Purcell, I., Gutberlet, M., Rioufol, G., et al. (2016). 1-year outcomes of ffrct-guided care in patients with suspected coronary disease: the platform study. *Journal of the American College of Cardiology*, 68(5):435–445.
- Douglas, P. S., Pontone, G., Hlatky, M. A., Patel, M. R., Norgaard, B. L., Byrne, R. A., Curzen, N., Purcell, I., Gutberlet, M., Rioufol, G., et al. (2015). Clinical outcomes of fractional flow reserve by computed tomographic angiography-guided diagnostic strategies vs. usual care in patients with suspected coronary artery disease: the prospective longitudinal trial of ffrct: outcome and resource impacts study. *European heart journal*, 36(47):3359–3367.
- Engelen, L., Ferreira, I., Stehouwer, C. D., Boutouyrie, P., Laurent, S., and for Arterial Measurements Collaboration, R. V. (2012). Reference intervals for common carotid intima-media thickness measured with echotracking: relation with risk factors. *European heart journal*, 34(30):2368–2380.
- Fischer, J. J., Samady, H., McPherson, J. A., Sarembock, I. J., Powers, E. R., Gimple, L. W., and Ragosta, M. (2002). Comparison between visual assessment and quantitative angiography versus fractional flow reserve for native coronary narrowings of moderate severity. *The American journal of cardiology*, 90(3):210–215.
- Fossan, F. E., Sturdy, J., Müller, L. O., Strand, A., Bråten, A. T., Jørgensen, A., Wiseth, R., and Hellevik, L. R. (2018). Uncertainty quantification and sensitivity analysis for computational ffr estimation in stable coronary artery disease. *Cardiovascular engineering and technology*, 9(4):597–622.
- Fuchs, A., Mejdahl, M. R., Kühl, J. T., Stisen, Z. R., Nilsson, E. J. P., Køber, L. V., Nordestgaard, B. G., and Kofoed, K. F. (2016). Normal values of left ventricular mass and cardiac chamber volumes assessed by 320-detector computed tomography angiography in the copenhagen general population study. *European Heart Journal-Cardiovascular Imaging*, 17(9):1009–1017.
- Garcia, D., Pibarot, P., and Durand, L.-G. (2005). Analytical modeling of the instantaneous pressure gradient across the aortic valve. *Journal of biomechanics*, 38(6):1303–1311.
- Gashi, K., Bosboom, E., and van de Vosse, F. (2018). The influence of model order reduction on the computed fractional flow reserve using parameterized coronary geometries. *Journal of biomechanics*.

- Gaur, S., Bezerra, H. G., Christiansen, E. H., Tanaka, K., Jensen, J. M., Kaltoft, A. K., Botker, H. E., Lassen, J. F., Terkelsen, C. J., and Norgaard, B. L. (2014a). Reproducibility of invasively measured and non-invasively computed fractional flow reserve. *Journal of the American College of Cardiology*, 63(12 Supplement):A999.
- Gaur, S., Bezerra, H. G., Lassen, J. F., Christiansen, E. H., Tanaka, K., Jensen, J. M., Oldroyd, K. G., Leipsic, J., Achenbach, S., Kaltoft, A. K., et al. (2014b). Fractional flow reserve derived from coronary ct angiography: variation of repeated analyses. *Journal of cardiovascular computed tomography*, 8(4):307–314.
- Gijssen, F. J., van de Vosse, F. N., and Janssen, J. (1999). The influence of the non-newtonian properties of blood on the flow in large arteries: steady flow in a carotid bifurcation model. *Journal of biomechanics*, 32(6):601–608.
- Gould, K. L. (2009). Does coronary flow trump coronary anatomy? *JACC: Cardiovascular Imaging*, 2(8):1009–1023.
- Gould, R. G., Lipton, M. J., Mcnamara, M. T., Sievers, R. E., Koshold, S., and Higgins, C. B. (1988). Measurement of regional myocardial blood flow in dogs by ultrafast ct. *Investigative radiology*, 23(5):348–353.
- Green, N. E., Chen, S.-Y. J., Messenger, J. C., Groves, B. M., and Carroll, J. D. (2004). Three-dimensional vascular angiography. *Current problems in cardiology*, 29(3):104–142.
- Haidekker, M. A., Tsai, A. G., Brady, T., Stevens, H. Y., Frangos, J. A., Theodorakis, E., and Intaglietta, M. (2002). A novel approach to blood plasma viscosity measurement using fluorescent molecular rotors. *American Journal of Physiology-Heart and Circulatory Physiology*, 282(5):H1609–H1614.
- Hall, J. E. (2015). *Guyton and Hall textbook of medical physiology e-Book*. Elsevier Health Sciences.
- Hannawi, B., Lam, W. W., Wang, S., and Younis, G. A. (2014). Current use of fractional flow reserve: a nationwide survey. *Texas Heart Institute Journal*, 41(6):579–584.
- Hayashi, H. and Yamaguchi, T. (2002). A simple computational model of the right coronary artery on the beating heart—effects of the temporal change of curvature and torsion on the blood flow. *Biorheology*, 39(3, 4):395–399.
- Huberts, W., Donders, W., Delhaas, T., and van de Vosse, F. (2014). Applicability of the polynomial chaos expansion method for personalization of a cardiovascular pulse wave propagation model. *International journal for numerical methods in biomedical engineering*, 30(12):1679–1704.
- Hulsen, M. (2007). Tfm: A toolkit for the finite element method.
- Huo, Y. and Kassab, G. S. (2007). A hybrid one-dimensional/womersley model of pulsatile blood flow in the entire coronary arterial tree. *American Journal of Physiology-Heart and Circulatory Physiology*, 292(6):H2623–H2633.
- Huo, Y., Svendsen, M., Choy, J. S., Zhang, Z.-D., and Kassab, G. S. (2011). A validated predictive model of coronary fractional flow reserve. *Journal of The Royal Society Interface*, page rsif20110605.

- Itu, L., Rapaka, S., Passerini, T., Georgescu, B., Schwemmer, C., Schoebinger, M., Flohr, T., Sharma, P., and Comaniciu, D. (2016). A machine learning approach for computation of fractional flow reserve from coronary computed tomography. *American Journal of Physiology-Heart and Circulatory Physiology*.
- Itu, L., Sharma, P., Mihalef, V., Kamen, A., Suci, C., and Lomaniciu, D. (2012). A patient-specific reduced-order model for coronary circulation. In *Biomedical Imaging (ISBI), 2012 9th IEEE International Symposium on*, pages 832–835. IEEE.
- Itu, L., Sharma, P., Ralovich, K., Mihalef, V., Ionasec, R., Everett, A., Ringel, R., Kamen, A., and Comaniciu, D. (2013). Non-invasive hemodynamic assessment of aortic coarctation: validation with in vivo measurements. *Annals of biomedical engineering*, 41(4):669–681.
- Johnson, N. P., Kirkeeide, R. L., and Gould, K. L. (2013). Coronary anatomy to predict physiology: fundamental limits. *Circulation: Cardiovascular Imaging*, 6(5):817–832.
- Johnston, B. M., Johnston, P. R., Corney, S., and Kilpatrick, D. (2004). Non-newtonian blood flow in human right coronary arteries: steady state simulations. *Journal of biomechanics*, 37(5):709–720.
- Johnston, B. M., Johnston, P. R., Corney, S., and Kilpatrick, D. (2006). Non-newtonian blood flow in human right coronary arteries: transient simulations. *Journal of biomechanics*, 39(6):1116–1128.
- Kassab, G. S. (2006). Scaling laws of vascular trees: of form and function. *American Journal of Physiology-Heart and Circulatory Physiology*, 290(2):H894–H903.
- Katritsis, D., Theodorakakos, A., Pantos, I., Andriotis, A., Efstathopoulos, E., Siontis, G., Karcanias, N., Redwood, S., and Gavaises, M. (2010). Vortex formation and recirculation zones in left anterior descending artery stenoses: computational fluid dynamics analysis. *Physics in Medicine & Biology*, 55(5):1395.
- Kelidis, P. and Konstantinidis, E. (2018). Pulsatile flow through a constricted tube: effect of stenosis morphology on hemodynamic parameters. *Computer methods in biomechanics and biomedical engineering*, 21(7):479–487.
- Késmárky, G., Kenyeres, P., Rábai, M., and Tóth, K. (2008). Plasma viscosity: a forgotten variable. *Clinical hemorheology and microcirculation*, 39(1–4):243–246.
- Kim, H., Vignon-Clementel, I., Coogan, J., Figueroa, C., Jansen, K., and Taylor, C. (2010). Patient-specific modeling of blood flow and pressure in human coronary arteries. *Annals of biomedical engineering*, 38(10):3195–3209.
- Kim, K.-H., Doh, J.-H., Koo, B.-K., Min, J. K., Erglis, A., Yang, H.-M., Park, K.-W., Lee, H.-Y., Kang, H.-J., Kim, Y.-J., et al. (2014). A novel noninvasive technology for treatment planning using virtual coronary stenting and computed tomography-derived computed fractional flow reserve. *JACC: Cardiovascular Interventions*, 7(1):72–78.
- Koo, B.-K., Erglis, A., Doh, J.-H., Daniels, D. V., Jegere, S., Kim, H.-S., Dunning, A., De-France, T., Lansky, A., Leipsic, J., et al. (2011). Diagnosis of ischemia-causing coronary stenoses by noninvasive fractional flow reserve computed from coronary computed

- tomographic angiograms: results from the prospective multicenter discover-flow (diagnosis of ischemia-causing stenoses obtained via noninvasive fractional flow reserve) study. *Journal of the American College of Cardiology*, 58(19):1989–1997.
- Kumaran, K., Fall, C. H., Martyn, C. N., Vijayakumar, M., Stein, C. E., and Shier, R. (2002). Left ventricular mass and arterial compliance: relation to coronary heart disease and its risk factors in south indian adults. *International journal of cardiology*, 83(1):1–9.
- Lee, J. M., Jung, J.-H., Hwang, D., Park, J., Fan, Y., Na, S.-H., Doh, J.-H., Nam, C.-W., Shin, E.-S., and Koo, B.-K. (2016). Coronary flow reserve and microcirculatory resistance in patients with intermediate coronary stenosis. *Journal of the American College of Cardiology*, 67(10):1158–1169.
- Legrand, V., Mancini, G. J., Bates, E. R., Hodgson, J. M., Gross, M. D., and Vogel, R. A. (1986). Comparative study of coronary flow reserve, coronary anatomy and results of radionuclide exercise tests in patients with coronary artery disease. *Journal of the American College of Cardiology*, 8(5):1022–1032.
- Long, J. A., Ündar, A., Manning, K. B., and Deutsch, S. (2005). Viscoelasticity of pediatric blood and its implications for the testing of a pulsatile pediatric blood pump. *ASAIO journal*, 51(5):563–566.
- Ludman, P. F. et al. (2012). Bcis audit returns adult interventional procedures. *British Cardiovascular Intervention Society, Glasgow*, 5.
- Mandal, P. K. (2005). An unsteady analysis of non-newtonian blood flow through tapered arteries with a stenosis. *International Journal of Non-Linear Mechanics*, 40(1):151–164.
- Marcinkowska-Gapińska, A., Gapinski, J., Elikowski, W., Jaroszyk, F., and Kubisz, L. (2007). Comparison of three rheological models of shear flow behavior studied on blood samples from post-infarction patients. *Medical & biological engineering & computing*, 45(9):837–844.
- Marcinkowska-Gapińska, A. and Kowal, P. (2009). Comparative analysis of chosen hemorheological methods in a group of stroke patients. *Clinical hemorheology and microcirculation*, 41(1):27–33.
- McGinn, A. L., White, C. W., and Wilson, R. F. (1990). Interstudy variability of coronary flow reserve. influence of heart rate, arterial pressure, and ventricular preload. *Circulation*, 81(4):1319–1330.
- McMillan, D., Utterback, N., Nasrinasrabi, M., and Lee, M. (1986). An instrument to evaluate the time dependent flow properties of blood at moderate shear rates. *Biorheology*, 23(1):63–74.
- Miller, D. D., Donohue, T. J., Younis, L. T., Bach, R. G., Aguirre, F. V., Wittry, M. D., Goodgold, H. M., Chaitman, B. R., and Kern, M. J. (1994). Correlation of pharmacological 99mTc-sestamibi myocardial perfusion imaging with poststenotic coronary flow reserve in patients with angiographically intermediate coronary artery stenoses. *Circulation*, 89(5):2150–2160.

- Min, J. K., Berman, D. S., Budoff, M. J., Jaffer, F. A., Leipsic, J., Leon, M. B., Mancini, G. J., Mauri, L., Schwartz, R. S., and Shaw, L. J. (2011). Rationale and design of the defacto (determination of fractional flow reserve by anatomic computed tomographic angiography) study. *Journal of cardiovascular computed tomography*, 5(5):301–309.
- Min, J. K., Leipsic, J., Pencina, M. J., Berman, D. S., Koo, B.-K., van Mieghem, C., Erglis, A., Lin, F. Y., Dunning, A. M., Apruzzese, P., et al. (2012). Diagnostic accuracy of fractional flow reserve from anatomic ct angiography. *Jama*, 308(12):1237–1245.
- Min, J. K., Taylor, C. A., Achenbach, S., Koo, B. K., Leipsic, J., Nørgaard, B. L., Pijls, N. J., and De Bruyne, B. (2015). Noninvasive fractional flow reserve derived from coronary ct angiography: clinical data and scientific principles. *JACC: Cardiovascular Imaging*, 8(10):1209–1222.
- Mirramezani, M., Diamond, S. L., Litt, H. I., and Shadden, S. C. (2019). Reduced order models for transstenotic pressure drop in the coronary arteries. *Journal of biomechanical engineering*, 141(3):031005.
- Mittal, N., Zhou, Y., Ung, S., Linares, C., Molloy, S., and Kassab, G. (2005). A computer reconstruction of the entire coronary arterial tree based on detailed morphometric data. *Annals of biomedical engineering*, 33(8):1015–1026.
- Morris, P. D., Narracott, A., von Tengg-Kobligk, H., Soto, D. A. S., Hsiao, S., Lungu, A., Evans, P., Bressloff, N. W., Lawford, P. V., Hose, D. R., et al. (2016). Computational fluid dynamics modelling in cardiovascular medicine. *Heart*, 102(1):18–28.
- Morris, P. D., Ryan, D., Morton, A. C., Lycett, R., Lawford, P. V., Hose, D. R., and Gunn, J. P. (2013). Virtual fractional flow reserve from coronary angiography: modeling the significance of coronary lesions: results from the virtu-1 (virtual fractional flow reserve from coronary angiography) study. *JACC: Cardiovascular Interventions*, 6(2):149–157.
- Morris, P. D., Soto, D. A. S., Feher, J. F., Rafiroiu, D., Lungu, A., Varma, S., Lawford, P. V., Hose, D. R., and Gunn, J. P. (2017). Fast virtual fractional flow reserve based upon steady-state computational fluid dynamics analysis: results from the virtu-fast study. *JACC: Basic to Translational Science*, 2(4):434–446.
- Morris, P. D., van de Vosse, F. N., Lawford, P. V., Hose, D. R., and Gunn, J. P. (2015). “virtual”(computed) fractional flow reserve: current challenges and limitations. *JACC: Cardiovascular Interventions*, 8(8):1009–1017.
- Mortensen, M. and Valen-Sendstad, K. (2015). Oasis: A high-level/high-performance open source navier–stokes solver. *Computer physics communications*, 188:177–188.
- Murray, C. D. (1926). The physiological principle of minimum work: I. the vascular system and the cost of blood volume. *Proceedings of the National Academy of Sciences*, 12(3):207–214.
- Nakazato, R., Park, H.-B., Berman, D. S., Gransar, H., Koo, B.-K., Erglis, A., Lin, F. Y., Dunning, A. M., Budoff, M. J., Malpeso, J., et al. (2013). Noninvasive fractional flow reserve derived from computed tomography angiography for coronary lesions of intermediate stenosis severity: results from the defacto study. *Circulation: Cardiovascular Imaging*, 6(6):881–889.

- Neofytou, P. (2004). Comparison of blood rheological models for physiological flow simulation. *Biorheology*, 41(6):693–714.
- Nørgaard, B. L., Leipsic, J., Gaur, S., Seneviratne, S., Ko, B. S., Ito, H., Jensen, J. M., Mauri, L., De Bruyne, B., Bezerra, H., et al. (2014). Diagnostic performance of noninvasive fractional flow reserve derived from coronary computed tomography angiography in suspected coronary artery disease: the next trial (analysis of coronary blood flow using ct angiography: Next steps). *Journal of the American College of Cardiology*, 63(12):1145–1155.
- Oliver, J. D. (1986). *The viscosity of human blood at high hematocrits*. PhD thesis, Massachusetts Institute of Technology.
- Pijls, N. H., de Bruyne, B., Peels, K., van der Voort, P. H., Bonnier, H. J., Bartunek, J., and Koolen, J. J. (1996). Measurement of fractional flow reserve to assess the functional severity of coronary-artery stenoses. *New England Journal of Medicine*, 334(26):1703–1708.
- Pijls, N. H., Fearon, W. F., Tonino, P. A., Siebert, U., Ikeno, F., Bornschein, B., van't Veer, M., Klauss, V., Manoharan, G., Engstrøm, T., et al. (2010). Fractional flow reserve versus angiography for guiding percutaneous coronary intervention in patients with multi-vessel coronary artery disease: 2-year follow-up of the fame (fractional flow reserve versus angiography for multivessel evaluation) study. *Journal of the American College of Cardiology*, 56(3):177–184.
- Pijls, N. H., Van Gelder, B., Van der Voort, P., Peels, K., Bracke, F. A., Bonnier, H. J., and El Gamal, M. I. (1995). Fractional flow reserve: a useful index to evaluate the influence of an epicardial coronary stenosis on myocardial blood flow. *Circulation*, 92(11):3183–3193.
- Pijls, N. H., van Schaardenburgh, P., Manoharan, G., Boersma, E., Bech, J.-W., van't Veer, M., Bär, F., Hoorntje, J., Koolen, J., Wijns, W., et al. (2007). Percutaneous coronary intervention of functionally nonsignificant stenosis: 5-year follow-up of the defer study. *Journal of the American College of Cardiology*, 49(21):2105–2111.
- Pijls, N. H., van Son, J. A., Kirkeeide, R. L., De Bruyne, B., and Gould, K. (1993). Experimental basis of determining maximum coronary, myocardial, and collateral blood flow by pressure measurements for assessing functional stenosis severity before and after percutaneous transluminal coronary angioplasty. *Circulation*, 87(4):1354–1367.
- Quemada, D. (1977). Rheology of concentrated disperse systems and minimum energy dissipation principle. *Rheologica Acta*, 16(1):82–94.
- Quemada, D. (1981). A rheological model for studying the hematocrit dependence of red cell-red cell and red cell-protein interactions in blood. *Biorheology*, 18(3-6):501–516.
- Quemada, D. (1983). Blood rheology and its implication in flow of blood. In *Arteries and arterial blood flow*, pages 1–127. Springer.
- Quicken, S., Donders, W. P., van Disseldorp, E. M., Gashi, K., Mees, B. M., van de Vosse, F. N., Lopata, R. G., Delhaas, T., and Huberts, W. (2016). Application of an adaptive polynomial chaos expansion on computationally expensive three-dimensional cardiovascular models for uncertainty quantification and sensitivity analysis. *Journal of Biomechanical Engineering*, 138(12):121010.

- Rand, P. W., Lacombe, E., Hunt, H. E., and Austin, W. H. (1964). Viscosity of normal human blood under normothermic and hypothermic conditions. *Journal of Applied Physiology*, 19(1):117–122.
- Ree, T. and Eyring, H. (1955). Theory of non-newtonian flow. ii. solution system of high polymers. *Journal of applied physics*, 26(7):800–809.
- Renker, M., Schoepf, U. J., Wang, R., Meinel, F. G., Rier, J. D., Bayer II, R. R., Möllmann, H., Hamm, C. W., Steinberg, D. H., and Baumann, S. (2014). Comparison of diagnostic value of a novel noninvasive coronary computed tomography angiography method versus standard coronary angiography for assessing fractional flow reserve. *The American journal of cardiology*, 114(9):1303–1308.
- Revellin, R., Rousset, F., Baud, D., and Bonjour, J. (2009). Extension of murray's law using a non-newtonian model of blood flow. *Theoretical Biology and Medical Modelling*, 6(1):7.
- Russell, I. (1997). Adenosine-induced coronary vasodilation during transesophageal doppler echocardiography: Rapid and safe measurement of coronary flow reserve ratio can predict significant left anterior descending coronary stenosis. rita f. redberg, youri sobol, tony m. chou, mary malloy, shantha kumar, eli botvinick, and john kane, circulation 1995; 92: 190-196. *CARDIOVASCULAR AND THORACIC ANESTHESIA JOURNAL CLUB JOURNAL*, 2:220–221.
- Sankaran, S., Grady, L., and Taylor, C. A. (2015). Fast computation of hemodynamic sensitivity to lumen segmentation uncertainty. *IEEE transactions on medical imaging*, 34(12):2562–2571.
- Sankaran, S., Grady, L. J., and Taylor, C. A. (2014). Real-time sensitivity analysis of blood flow simulations to lumen segmentation uncertainty. In *International Conference on Medical Image Computing and Computer-Assisted Intervention*, pages 1–8. Springer.
- Sankaran, S., Kim, H. J., Choi, G., and Taylor, C. A. (2016). Uncertainty quantification in coronary blood flow simulations: impact of geometry, boundary conditions and blood viscosity. *Journal of biomechanics*, 49(12):2540–2547.
- Sankaran, S., Moghadam, M. E., Kahn, A. M., Tseng, E. E., Guccione, J. M., and Marsden, A. L. (2012). Patient-specific multiscale modeling of blood flow for coronary artery bypass graft surgery. *Annals of biomedical engineering*, 40(10):2228–2242.
- Schrauwen, J. T., Koeze, D. J., Wentzel, J. J., van de Vosse, F. N., van der Steen, A. F., and Gijzen, F. J. (2015). Fast and accurate pressure-drop prediction in straightened atherosclerotic coronary arteries. *Annals of biomedical engineering*, 43(1):59–67.
- Seeley, B. D. and Young, D. F. (1976). Effect of geometry on pressure losses across models of arterial stenoses. *Journal of biomechanics*, 9(7):447–448.
- Segal, G. (1989). The sepran finite element package. *Ingenieursburo Sepra, Leidschendam, The Netherlands*.
- Sharma, P., Itu, L., Zheng, X., Kamen, A., Bernhardt, D., Suci, C., and Comaniciu, D. (2012). A framework for personalization of coronary flow computations during rest and hyperemia. pages 6665–6668.

- Sharp, M. K., Thurston, G. B., and Moore, J. (1996). The effect of blood viscoelasticity on pulsatile flow in stationary and axially moving tubes. *Biorheology*, 33(3):185–208.
- Sobol', I. M. (1967). On the distribution of points in a cube and the approximate evaluation of integrals. *Zhurnal Vychislitel'noi Matematiki i Matematicheskoi Fiziki*, 7(4):784–802.
- Spencer, A. J. M. (2004). *Continuum mechanics*. Courier Corporation.
- Stary, H. C., Chandler, A. B., Dinsmore, R. E., Fuster, V., Glagov, S., Insull Jr, W., Rosenfeld, M. E., Schwartz, C. J., Wagner, W. D., and Wissler, R. W. (1995). A definition of advanced types of atherosclerotic lesions and a histological classification of atherosclerosis: a report from the committee on vascular lesions of the council on arteriosclerosis, american heart association. *Circulation*, 92(5):1355–1374.
- Steele, B. N., Olufsen, M. S., and Taylor, C. A. (2007). Fractal network model for simulating abdominal and lower extremity blood flow during resting and exercise conditions. *Computer Methods in Biomechanics and Biomedical Engineering*, 10(1):39–51.
- Stuijzfand, W. J., Uusitalo, V., Kero, T., Danad, I., Rijniense, M. T., Saraste, A., Rajmakers, P. G., Lammertsma, A. A., Harms, H. J., Heymans, M. W., et al. (2015). Relative flow reserve derived from quantitative perfusion imaging may not outperform stress myocardial blood flow for identification of hemodynamically significant coronary artery disease. *Circulation: Cardiovascular Imaging*, 8(1):e002400.
- Tang, D., Yang, C., Kobayashi, S., Zheng, J., Woodard, P. K., Teng, Z., Billiar, K., Bach, R., and Ku, D. N. (2009). 3d mri-based anisotropic fsi models with cyclic bending for human coronary atherosclerotic plaque mechanical analysis. *Journal of biomechanical engineering*, 131(6):061010.
- Taylor, C. A., Fonte, T. A., and Min, J. K. (2013). Computational fluid dynamics applied to cardiac computed tomography for noninvasive quantification of fractional flow reserve: scientific basis. *Journal of the American College of Cardiology*, 61(22):2233–2241.
- Tona, F., Caforio, A. L., Montisci, R., Gambino, A., Angelini, A., Ruscazio, M., Toscano, G., Feltrin, G., Ramondo, A., Gerosa, G., et al. (2006). Coronary flow velocity pattern and coronary flow reserve by contrast-enhanced transthoracic echocardiography predict long-term outcome in heart transplantation. *Circulation*, 114(1_supplement):I–49.
- Tonino, P. A., De Bruyne, B., Pijls, N. H., Siebert, U., Ikeno, E., vant Veer, M., Klauss, V., Manoharan, G., Engström, T., Oldroyd, K. G., et al. (2009). Fractional flow reserve versus angiography for guiding percutaneous coronary intervention. *New England Journal of Medicine*, 360(3):213–224.
- Tonino, P. A., Fearon, W. F., De Bruyne, B., Oldroyd, K. G., Leesar, M. A., Ver Lee, P. N., MacCarthy, P. A., Van't Veer, M., and Pijls, N. H. (2010). Angiographic versus functional severity of coronary artery stenoses in the fame study: fractional flow reserve versus angiography in multivessel evaluation. *Journal of the American College of Cardiology*, 55(25):2816–2821.
- Tu, S., Barbato, E., Köszegi, Z., Yang, J., Sun, Z., Holm, N. R., Tar, B., Li, Y., Rusinaru, D., Wijns, W., et al. (2014). Fractional flow reserve calculation from 3-dimensional quantitative coronary angiography and timi frame count: a fast computer model to quantify the

- functional significance of moderately obstructed coronary arteries. *JACC: Cardiovascular Interventions*, 7(7):768–777.
- Valen-Sendstad, K., Mardal, K.-A., and Steinman, D. A. (2013). High-resolution cfd detects high-frequency velocity fluctuations in bifurcation, but not sidewall, aneurysms. *Journal of biomechanics*, 46(2):402–407.
- Valen-Sendstad, K. and Steinman, D. A. (2014). Mind the gap: impact of computational fluid dynamics solution strategy on prediction of intracranial aneurysm hemodynamics and rupture status indicators. *American Journal of Neuroradiology*, 35(3):536–543.
- Van Belle, E., Rioufol, G., Pouillot, C., Cuisset, T., Bougrini, K., Teiger, E., Champagne, S., Belle, L., Barreau, D., Hanssen, M., et al. (2014). Outcome impact of coronary revascularization strategy reclassification with fractional flow reserve at time of diagnostic angiography: insights from a large french multicenter fractional flow reserve registry. *Circulation*, 129(2):173–185.
- Van de Vosse, F. N. and Stergiopoulos, N. (2011). Pulse wave propagation in the arterial tree. *Annual Review of Fluid Mechanics*, 43:467–499.
- Van der Giessen, A. G., Groen, H. C., Doriot, P.-A., De Feyter, P. J., Van der Steen, A. E., Van de Vosse, F. N., Wentzel, J. J., and Gijssen, F. J. (2011). The influence of boundary conditions on wall shear stress distribution in patients specific coronary trees. *Journal of biomechanics*, 44(6):1089–1095.
- van der Horst, A., Boogaard, F. L., van't Veer, M., Rutten, M., Pijls, N. H., and van de Vosse, F. N. (2013). Towards patient-specific modeling of coronary hemodynamics in healthy and diseased state. *Computational and mathematical methods in medicine*, 2013.
- Van Tricht, I., De Wachter, D., Tordoir, J., Vanhercke, D., and Verdonck, P. (2005). Experimental analysis of the hemodynamics in punctured vascular access grafts. *ASAIO journal*, 51(4):352–359.
- Vignon-Clementel, I. E., Figueroa, C., Jansen, K., and Taylor, C. (2010). Outflow boundary conditions for 3d simulations of non-periodic blood flow and pressure fields in deformable arteries. *Computer methods in biomechanics and biomedical engineering*, 13(5):625–640.
- Vignon-Clementel, I. E., Figueroa, C. A., Jansen, K. E., and Taylor, C. A. (2006). Outflow boundary conditions for three-dimensional finite element modeling of blood flow and pressure in arteries. *Computer methods in applied mechanics and engineering*, 195(29-32):3776–3796.
- Waksman, R., Prati, F., Bruining, N., Haude, M., Böse, D., Kitabata, H., Erne, P., Verheye, S., Degen, H., Vermeersch, P., et al. (2013). Serial observation of drug-eluting absorbable metal scaffold: multi-imaging modality assessment. *Circulation: Cardiovascular Interventions*, 6(6):644–653.
- Wei, K., Ragosta, M., Thorpe, J., Coggins, M., Moos, S., and Kaul, S. (2001). Noninvasive quantification of coronary blood flow reserve in humans using myocardial contrast echocardiography. *Circulation*, 103(21):2560–2565.

- Wilson, R. F., Johnson, M. R., Marcus, M. L., Aylward, P., Skorton, D. J., Collins, S., and White, C. W. (1988). The effect of coronary angioplasty on coronary flow reserve. *Circulation*, 77(4):873–885.
- Yao, J., Sakaguchi, T., Yousuf, O., Trost, J., Lima, J. A., and George, R. T. (2013). Image-based fractional flow reserve using coronary angiography. In *2013 IEEE Nuclear Science Symposium and Medical Imaging Conference (2013 NSS/MIC)*, pages 1–4. IEEE.
- Yushkevich, P. A., Piven, J., Cody Hazlett, H., Gimpel Smith, R., Ho, S., Gee, J. C., and Gerig, G. (2006). User-guided 3D active contour segmentation of anatomical structures: Significantly improved efficiency and reliability. *Neuroimage*, 31(3):1116–1128.
- Zreik, M., Lessmann, N., van Hamersvelt, R. W., Wolterink, J. M., Voskuil, M., Viergever, M. A., Leiner, T., and Išgum, I. (2018). Deep learning analysis of the myocardium in coronary ct angiography for identification of patients with functionally significant coronary artery stenosis. *Medical image analysis*, 44:72–85.

Samenvatting

De belangrijkste taak van het hart is zorgen voor voldoende transport van bloed. Om deze taak te kunnen uitvoeren moet het hart zelf ook van voldoende bloed voorzien worden. Het hart krijgt bloed via de linker en rechter kransslagaders (coronaire arteriën). Optimale bloedstroom is belangrijk om de hartfunctie in stand te houden. De bloedstroom in de kransslagaders kan echter afnemen bij patiënten met coronaire hartziekten (CHD). Bij CHD is er sprake van een abnormale ophoping van plaque gedurende een lange periode wat uiteindelijk resulteert in vernauwde segmenten van de kransslagaders (stenose). Naarmate de plaque groeit neemt het lumenoppervlak, de doorsnede waar bloed kan stromen, in de kransslagaders af. Een direct gevolg hiervan is extra bloeddrukverlies over een stenose. Dit resulteert in een lagere bloedstroom in de aangetaste kransslagader. Deze lagere bloedstroom kan ervoor zorgen dat het hartspierweefsel, gevoed door deze aangetaste kransslagader, een verhoogde kans heeft op een tekort aan bloed (ischemie) wat kan leiden tot een infarct. Patiënten met CHD kunnen symptomen vertonen zoals pijn op de borst en een onbehaaglijk gevoel gedurende stress of inspanning en in ernstige gevallen ook gedurende rust. Behandelopties voor patiënt met CHD hangen af van de ernst van de stenose, locatie van de stenose en de medische geschiedenis van de patiënt. Uit eerder onderzoek is gebleken dat patiënten met milde CHD geen baat hebben bij een invasieve behandeling zoals angioplastie en stentplaatsing. Voor deze patiënten is aangetoond dat veranderingen in levensstijl en medicatie voldoende zijn. Patiënten met ernstige vernauwingen daarentegen behoeven een invasieve behandeling. De ernst van een stenose wordt in de kliniek vastgesteld met behulp van de fractional flow reserve (FFR) welke gedefinieerd is als de verhouding tussen de bloeddruk distaal van de stenose en de bloeddruk proximaal van de stenose. Afhankelijk van de gemeten FFR komen patiënten in aanmerking voor een invasieve behandeling (ernstige stenose, $FFR \leq 0.80$) of enkel een behandeling met behulp van medicijnen ($FFR > 0.80$). Voor patiënten die behandeld worden door middel van medicijnen wordt de FFR meting echter gezien als een onnodige invasieve meting. Computermodellen kunnen gebruikt worden om het aantal onnodige invasieve metingen te reduceren door op deze manier patiënt specifiek de bloedstroom in de kransslagaders te simuleren. Het voordeel is dat de ernst van een stenose niet-invasief bepaald kan worden. Dit zorgt voor een vermindering van het ongemak van patiënten, terwijl het bovendien het aantal complicaties verlaagt. Het potentiële voordeel van patiënt specifieke modellen van de kransslagaders is al in eerder onderzoek aangetoond. Echter vanwege hoge rekentijden van de 3D modellen is het niet mogelijk om de onzekerheid op modelparameters in deze modellen mee te nemen in een gevoeligheidsanalyse. Het doel van deze thesis was tweeledig. Het eerste doel is gericht op het reduceren van de rekentijd van de modellen door te onderzoeken in hoe verre lagere orde modellen gebruikt kunnen worden. Het tweede doel is onderzoeken wat de invloed is van parameteronzekerheid op de

berekende FFR in de kransslagadermodellen. Deze thesis omvat de volgende hoofdstukken: In **Hoofdstuk 2** wordt de invloed van verschillende aannames van de bloedviscositeit op de berekende FFR onderzocht. Van bloed is bekend dat het een niet-Newtonse vloeistof is met een hoge viscositeit bij lage afschuifsnellheden en een lage viscositeit bij hoge afschuifsnellheden. Het effect van aannames voor de bloedviscositeit werden onderzocht door simulaties te vergelijken met voor een constante waarde voor de viscositeit (Newtons), een constante waarde die afhangt van de hematocriet en een niet-Newtonse model voor de viscositeit (Quemada model) waarbij de viscositeit eveneens afhangt van de hematocriet. Door gebruik te maken van de verschillende aannames kan de spreiding die resulteert op de berekende FFR onderzocht worden. De resultaten lieten zien dat afhankelijk van het gekozen viscositeitsmodel en de parameterkeuze de FFR kan variëren tot 0.065. De meeste verschillen in FFR werden gevonden bij een FFR tussen de 0.6 en 0.8. In verschillende gevallen (53%) was de verandering in berekende FFR significant genoeg om een stenose anders te classificeren. Dit laat zien dat de keuze van het viscositeitsmodel de nauwkeurigheid van de FFR berekeningen beïnvloedt en dus zou kunnen leiden tot een andere medische behandeling. In **Hoofdstuk 3** is het Quemada model gebruikt dat bekend staat om de nauwkeurige beschrijving van de bloedviscositeit. Dit Quemada model hangt af van twee fysische grootheden hematocriet en plasmaviscositeit die in de kliniek gemeten kunnen worden. Door gebruik te maken van populatiespreidingen voor hematocriet en plasmaviscositeit kon de onzekerheid op de berekende FFR onderzocht worden in het geval dat beide parameters onbekend zijn voor een patiënt. Toevoegen van patiënt specifieke hematocriet waardes reduceerde de FFR onzekerheid gemiddeld met een factor 2.2. Resultaten lieten zien dat ongeveer 60% en 40% van de onzekerheid in de FFR toegeschreven kunnen worden aan respectievelijk hematocriet en plasmaviscositeit. In **Hoofdstuk 4** is het effect van vereenvoudiging van het model in modelorde onderzocht voor geparametriseerde CFD geometrieën. Hiertoe zijn 200 vernauwde coronairvaten gemaakt in 3D met zeven verschillende geometrische kenmerken zoals ernst van de stenose, curvatuur van het vat, torsie van het vat, enz. Voor elk 3D geometrie werd een bijbehorend 2D geometrie gemaakt. Het doel was om te onderzoeken of een hoge nauwkeurigheid gewaarborgd blijft wanneer gebruik wordt gemaakt van een veel minder rekenintensief model (2D). De resultaten laten zien dat een 2D model nauwkeurig genoeg is om het 3D model te vervangen. Bovendien hebben we laten zien dat wanneer een 'correcte' stationaire bloedstroom wordt gekozen de resultaten overeenkomen met de resultaten van instationaire simulaties die veel rekenintensiever zijn. Het effect van verschillende parameters in de randvoorwaarden op de berekende FFR is onderzocht in **Hoofdstuk 5**. Hiervoor werd de bloedstroom afgeschat op basis van de myocardgrootte en de verwachte doorbloeding van het myocard (bloedstroom per hoeveelheid myocard). De bloedstroom door de afzonderlijke aftakkingen van de bloedvaten werd verdeeld met behulp van de wet van Murray. De bloeddruk aan de instroomkant werd gelijkgesteld aan de gemiddelde arteriële druk. Deze vier parameters werden gevarieerd binnen de variatie die verwacht wordt over alle patiënten. De resultaten lieten zien dat de grootte van het myocard het grootste effect had op de FFR. De constante van Murray en de gemiddelde arteriële druk daarentegen hadden een kleine tot verwaarloosbaar effect. Zelfs met een onzekerheid van 5% was de grootte van het myocard nog steeds de belangrijkste parameter. Voor nauwkeurige FFR voorspellingen is het dus belangrijk dat de grootte van het myocard en de doorbloeding nauwkeurig afgeschat kunnen worden. In deze thesis hebben we laten zien dat de rekentijd voor modellen verminderd kan worden en dat er rekening gehouden moet worden met de onzekerheden in modelparameters.

Dankwoord

In dit laatste deel van mijn thesis wil ik iedereen die direct dan wel indirect betrokken was bij mijn promotie bedanken. Het was me een ware eer om vier jaar lang met zo veel mensen te mogen samenwerken.

Allereerst mijn wil ik mijn promotor Frans van de Vosse en co-promotor Marielle Bosboom bedanken. Ik heb de afgelopen vier jaar lang nauw met jullie mogen samenwerken. Beste Frans, gedurende de afgelopen vier jaar hebben we intensief mogen samen werken. Bijna wekelijks hadden we een afspraak om de voortgang van het project te bespreken waarbij we samen met Marielle aan de volgende stap dachten. Aangezien een groot deel van mijn promotie uit modelontwikkeling bestond liep ik zo nu en dan tegen problemen aan waar ik niet altijd zelf uitkwam. Als het probleem niet voor donderdag verholpen was dan wist ik dat ik donderdag een lijst met handige tips kon verwachten die me dichterbij de oplossing zouden brengen. Dit zorgde er voor dat ik met een goed gevoel naar de afspraken ging. Uiteraard wil ik je ook graag bedanken voor het vertrouwen en de vrijheden die ik tijdens mijn promotie heb mogen ervaren.

Beste Marielle, gedurende mijn promotie was jij mijn dagelijkse begeleider waar ik snel terecht kon wanneer het nodig was. Zeker wanneer de afspraak met Frans niet altijd kon doorgaan was het fijn om te weten dat de afspraak met jou meestal wel kon doorgaan. Het was vaak zo dat we samen dan de knoop doorhakten wanneer ik niet altijd kon kiezen tussen meerdere verschillende manieren van aanpak. Waar ik je ook graag voor wil bedanken is het feit dat ik artikelen en abstracts vrij snel terug kreeg verzien van goed commentaar.

Furthermore, I would like to thank Charles Taylor for being my co-promotor and giving me the opportunity to come to HeartFlow and do some wonderful research.

I would like to thank the members of the defense committee, prof. dr. Leif Rune Hellevik, prof. dr. ir. Max Viergever, dr. ir. Martien Hulsen en dr. Pim Tonino for carefully reviewing my dissertation and participating in the defense ceremony.

Ik wil graag ook Wouter Huberts bedanken voor zijn hulp en tijd. Wanneer ik even een net iets andere invalshoek nodig had kon ik vaak bij jou langs. Ik moet zeggen dat het me best vaak geholpen heeft om zo nu en dan vragen te stellen bij een kop koffie.

Marcel van 't Veer, hartelijk dank voor je hulp. Zeker halverwege mijn promotie heb ik heel veel aan jouw input en hulp gehad.

Beste Sjeng, hoewel we beiden na ons afstuderen op een ander project en universiteit terecht zijn gekomen hebben we continu samengewerkt. We hebben vaak via de telefoon gebrainstormd over elkaars problemen en over de beste manier van aanpak wat ertoe geleid

heeft dat we steeds een stap vooruit kwamen. Het is wel jammer dat we niet zoals tijdens ons afstuderen hebben kunnen samenwerken, anders hadden we samen nog veel meer kunnen bereiken.

In een tijd dat ik het best druk had kwam jouw hulp voor het genereren van de meshes toch echt op het juiste moment. Hartelijk dank hiervoor Martijn.

I want to thank the solver team at HeartFlow for making me feel welcome from the first day on. I really enjoyed working in the solver team. Furthermore special thanks to Nan Xiao and Buzzy Spain for helping me performing all the necessary steps during and also after my stay at HeartFlow.

Luc, zonder jou was de trip naar Amerika een stuk saaier geweest en zeker buiten de kantooruren. Ik denk ook niet dat ik zelf de culinaire hoogstandjes zoals Panda Express en In-N-Out Burger had ontdekt.

Gedurende mijn promotie heb ik meerdere bachelor en master studenten mogen begeleiden. Ik wil jullie graag bedanken voor jullie interesse en bijdrage. In het bijzonder wil ik graag Bas, Camile, Janine en Tommy bedanken voor hun direct dan wel indirecte bijdrage aan het onderzoek dat ik heb mogen doen. Tijdens het eerste deel van mijn promotie waar ik vooral nog bezig was met het exacte pad uitstippen was het toch best fijn dat ik met jullie kon sparren en discussiëren over bepaalde problemen.

Beste Roel en Bram, ik ken jullie beide al sinds de middelbare school. Het is toch altijd leuk om zo nu en dan bij te praten en zeker als het varend door de Amsterdamse grachten is. Het wordt eens tijd dat we dit weer een doen.

Maarten, Peter, Raoul, Sjeng en Tamara hoewel we allemaal goed verspreid waren voor onze PhD dan wel QME was het toch wel leuk om zo nu en dan weer eens af te spreken. Dit moeten we ook zeker blijven doen.

Beste Sjeng en Maarten, ik wil jullie graag bedanken voor de leuke avonden in Maastricht waar we lekker konden bijpraten en relativeren. Verder waren de bootfeesten in Maastricht toch altijd weer een succes. Ik moet zeggen dat ik me echt als een PhD IN Maastricht voelde.

Ook de kantoorgenoten uit 4.11 wil ik bedanken voor de leuke tijd op het werk. Beste Eline, Emiel, Esther, Hein, Janine, Jibbe, Joerik, Louis, Louise, Maarten, Marloes, Nicole, Niels, Peilu, Rob, Roel, Stefan en Ümit het was me een waar genoeg om samen met jullie een kantoor te mogen delen. Samen hebben we ervoor gezorgd dat 4.11 toch echt een begrip werd. De vele grappen en opmerkingen die al dan niet soms een beetje te ver gingen deden me af en toe geloven dat ik in een soort Truman Show vast zat waarbij betaalde acteurs zich voordeden als promovendi. Ik had het sterke vermoeden dat het acteersalaris ook nog eens afhing van de hoeveelheid onzin/lawaai dat er geproduceerd werd. Desalniettemin moet ik zeggen dat ik heb genoten van mijn tijd in 4.11. Mijn promotie is er niet makkelijker op geworden maar zeker wel leuker en daarvoor wil ik jullie graag bedanken. Uiteraard wil ik ook nog de mannen van de HIR bedanken voor de nauwe samenwerking. Niels, Emiel en Joerik het heeft me best goed gedaan om zo nu en dan met jullie te kunnen sparren. Na lange tijd onderdeel te zijn geweest van de HIR is het tijd om af te treden en plek te

maken voor iemand anders. Ik ga ervan uit dat Marloes net zo goed haar best gaat doen als onze vorige aanwinst Joerik. Om zeker te zijn dat alles goed gaat binnen de HIR, heb ik toch maar even sensei gevraagd om een oogje in het zeil te houden. Nicole, ik ben echt blij dat jij ook in het kantoor zat. Je hebt de groep strak bij elkaar gehouden met de vele kantooractiviteiten. Zo nu en dan werden bepaalde mensen (onder andere ik) gedwongen om toch mee te gaan wat ook wel goed was. Bovendien als ik bedenk hoeveel kilo lekkere taart en cake jij gedurende een maand mee naar kantoor bracht ben ik verbaasd dat niemand echt is aangekomen. Uiteraard wil ik je graag bedanken voor de leuke en diepgaande gesprekken. Emiel, als directe buurman hebben we denk ik toch echt een mooie tijd achter de rug. Verder ik heb echt enorm veel aan je tips en hulp gehad, zeker aan het einde van mijn promotie. Het ging een stuk sneller, bedankt hiervoor. Niels, voor technische vragen of hulp in de zin van 'hoe zou jij dit aanpakken?' was jij een echt grote hulp bij het oplossen van menig problemen, verder ben je ook een toffe huisgenoot. Joerik, ik stel voor dat we nog meer 'leuke' routes voor het wielrennen uitzoeken en ook nog eens het een en andere persoonlijk record verpletteren.

Ik wil ook nog vrienden en collega's uit de andere kantoren (Ashley, Laura, Marc, Marjan, Mathieu, Nicole, Pim, Stefan, Willeke) bedanken voor de gezellige lunches, de vele spannende tafelvoetbalpotjes en ook de leuke borrels. Mathieu, de blikjestijd was het moment van de dag waar ik heel goed kon ontspannen en zo met frisse moed weer aan het werk kon. Willeke, ik heb uiteindelijk best veel aan je tips en hulp gehad voor de discussie, bedankt hiervoor. Nicole, toch wel leuk om vervroegd naar de borrel te gaan als het weer eens een onproductieve dag bleek te zijn.

Tommy, gedurende mijn promotie hebben we best vaak bijgepraat tijdens de intensieve spinsessies. Aangezien ik geen sportkaart meer heb stel ik voor dat we dit vaker doen maar nu buiten op de fiets.

Richard, hoewel ik geen pulse-aio was, was ik wel welkom bij de belangrijke pulse-meetings (lees borrels, terrasjes en andere festiviteiten) welke toch altijd een groot succes waren. De treintrip van 14 uur naar Graz waar we samen met Emiel uiteindelijk in de continuumbar terecht kwamen was toch wel de trip die me het meeste is bijgebleven.

Uiteraard wil ik nog graag mijn paranimfen bedanken dat ze hebben toegezegd om me bij te staan bij deze belangrijke laatste taak. Beste Roel, ik ken je al sinds de middelbare school. Ik denk dat ik vandaag wel een beetje van jouw 'gewoon doen' mentaliteit en spontaniteit kan gebruiken. Beste Maarten, een tijdje terug waren de rollen omgedraaid waarbij ik jouw paranimf mocht zijn. Vandaag hoop ik toch wel dat je wat 'hemels' advies voor me hebt voor de verdediging begint.

Lieve Lavdrim en Marigona, ik ben ontzettend blij dat jullie mijn broer en zus zijn. Lieve pap en mam, ik wil jullie bedanken voor hun onvoorwaardelijke liefde en steun. Jullie hebben me gemotiveerd om altijd mijn best te doen, dit heeft er nu voor gezorgd dat ik nu hier sta. Daar ben ik ontzettend dankbaar voor.

Kujtim Gashi
Mei 2019

Curriculum vitae

Kujtim Gashi was born on the 19th of October 1990, in Zürich, Switzerland. He grew up in Helmond, the Netherlands, and attended VWO at the Dr.-Knippenbergcollege in Helmond, where he graduated in 2009. In the same year he started studying Biomedical Engineering at the Eindhoven University of Technology, where he obtained his Bachelor's degree in 2012. Afterwards, he started his Master Medical Engineering in the Cardiovascular Biomechanics Group of prof. Frans van de Vosse. During his Master's degree he performed an internship at the University of Bern where he worked on the improvement of image quality and frame rate of existing photoacoustics and ultrasound imaging modality making it suitable of real time image acquisition. For his Master's thesis he implemented a stabilization scheme for an in-house finite element package which made modelling of (biomedical) flows at high flow rates feasible without the need for computational expensive models. He graduated in November 2014. In January 2015, he started as a PhD candidate at the Eindhoven University of Technology, with the focus on developing and applying computer models for diseased coronary arteries. The results of this PhD research are presented in this dissertation.

List of publications

Journal publications

K. Gashi, N. Xiao, E. M. H. Bosboom, M. van 't Veer, C. A. Taylor, and F. N. van de Vosse, Impact of blood viscosity models on computed fractional flow reserve, Submitted: *Annals of Biomedical Engineering*, 2019;

K. Gashi, N. Xiao, E. M. H. Bosboom, S. Quicken, W. Huberts, C. A. Taylor, and F. N. van de Vosse, Influence of population-based variance of blood viscosity on the uncertainty in computed fractional flow reserve, Submitted: *Journal of Biomechanics*, 2019;

K. Gashi, E. M. H. Bosboom, M. J. M. M. Hoeijmakers, M. Zreik, I. Išgum, T. Leiner, and F. N. van de Vosse, Submitted: *Uncertainty quantification for predicted FFR using myocardial perfusion and left ventricular mass*, 2019;

K. Gashi, E.M.H. Bosboom, F.N. van de Vosse, The influence of model order reduction on the computed fractional flow reserve using parameterized coronary geometries, *Journal of Biomechanics*, 2018;

E.E. van Haften, T.B. Wissing, M.C.M. Rutten, **K. Gashi**, A.J. van Kelle, A.I.P.M. Smits, C.V.C. Bouten, N.A. Kurniawan, Decoupling the effect of shear stress and stretch on tissue growth and remodeling in a vascular graft, *Tissue Engineering Part C: Methods*, 2018;

S. Quicken, W.P. Donders, E.M.J. van Disseldorp, **K. Gashi**, B.M. Mees, F.N. van de Vosse, R.G.P. Lopata, T. Delhaas, W. Huberts, Application of an Adaptive Polynomial Chaos Expansion on Computationally Expensive Three-Dimensional Cardiovascular Models for Uncertainty Quantification and Sensitivity Analysis, *Journal of Biomechanical Engineering*, 2016; 138(12): pp. 1-11.

M. Jaeger, **K. Gashi**, H.G. Akerçay, G. Held, S. Peeters, T. Petrosyan, S. Preisser, M. Gruenig, M. Frenz, Real-time clinical clutter reduction in combined epi-optoacoustic and ultrasound imaging, *Photonics and Lasers in Medicine*, 2014;